Chapter 4

Natural Gas / Hydrogen Flames

4.1 Introduction

This chapter presents measurements of turbulent nonpremixed jet flames issuing into a coflow of either 3% or 9% O_2 (by volume) at a temperature of 1100K. The fuel used in the jet is a mixture of natural gas and hydrogen. The hot and diluted oxidant produced by the JHC (Jet in Hot Coflow) burner (§3.2.1) emulates MILD combustion conditions. The OH radical, formaldehyde and temperature are imaged instantaneously and simultaneously with laser diagnostic techniques.

Three different jet Reynolds numbers are used to investigate the influence of the Reynolds number on the flame structure. Hydrogen is added to the fuel to improve flame stabilisation. Hydrogen also reduces the level of soot, which could potentially interfere with the laser measurements. Measurements are taken at two downstream locations. Near the jet exit, the reaction takes place in the coflow with a defined O_2 concentration. At the most downstream location the effects of entrainment of the surrounding air on the flame structure are investigated.

4.2 Flame Conditions

The jet in hot coflow (JHC) burner has been described in detail in §3.2.1. In brief, the JHC burner consists of a central fuel jet within an annular coflow of

Fuel (mol/mol)	Re_{jet}	$\dot{Q}$ [L$_n$/min]	$\bar{v}_{exit}$ [m/s]
	5000	24.0	26.4
Natural gas / H$_2$ (1:1)	10000	48.0	52.9
	15000	72.0	79.3

Table 4.1: Jet operating conditions of natural gas/hydrogen flames. Re_{jet}; Jet Reynolds number, $\dot{Q}$; volumetric flowrate, $\bar{v}_{exit}$; mean exit velocity (for an exit temperature of 300K).

Excess O$_2$ (mol/mol)		3% O$_2$	9% O$_2$
Premixed	O$_2$	3%	9%
combustion	N$_2$	84%	78%
products	H$_2$O	10%	10%
(mol/mol)	CO$_2$	3%	3%
Post-combustion	Temp.	1100K	1100K
products	$\bar{U}$	~2.4 m/s	~2.4 m/s
	Re	~1400	~1400

Table 4.2: Coflow composition and flow conditions for natural gas/hydrogen flames

exhaust products from a secondary burner. Both the jet and coflow conditions are controlled separately. Tables 4.1 and 4.2 list the flowrates and operating conditions of the jet and coflow, respectively, for the flame conditions presented in this chapter. Measurements for each jet Reynolds number listed in Table 4.1 are taken at both of the coflow O$_2$ levels described in Table 4.2.

The coflow composition consists of the exhaust products from the premixed, porous bed, secondary burner. The amount of excess oxygen in the secondary burner governs the O$_2$ level of the coflow. The ratio of the air/nitrogen in the coflow was varied to give the desired O$_2$ levels, while maintaining a constant coflow temperature and exit velocity between the two cases. The composition of the main species (as shown in Table 4.2) is determined assuming equilibrium conditions. The coflow temperature has been measured, and confirmed that the temperature is constant (at 1100K) for both O$_2$ cases. From the composition and temperature, the mean exit velocity and coflow Reynolds number (based on inner annulus diameter) are also calculated.
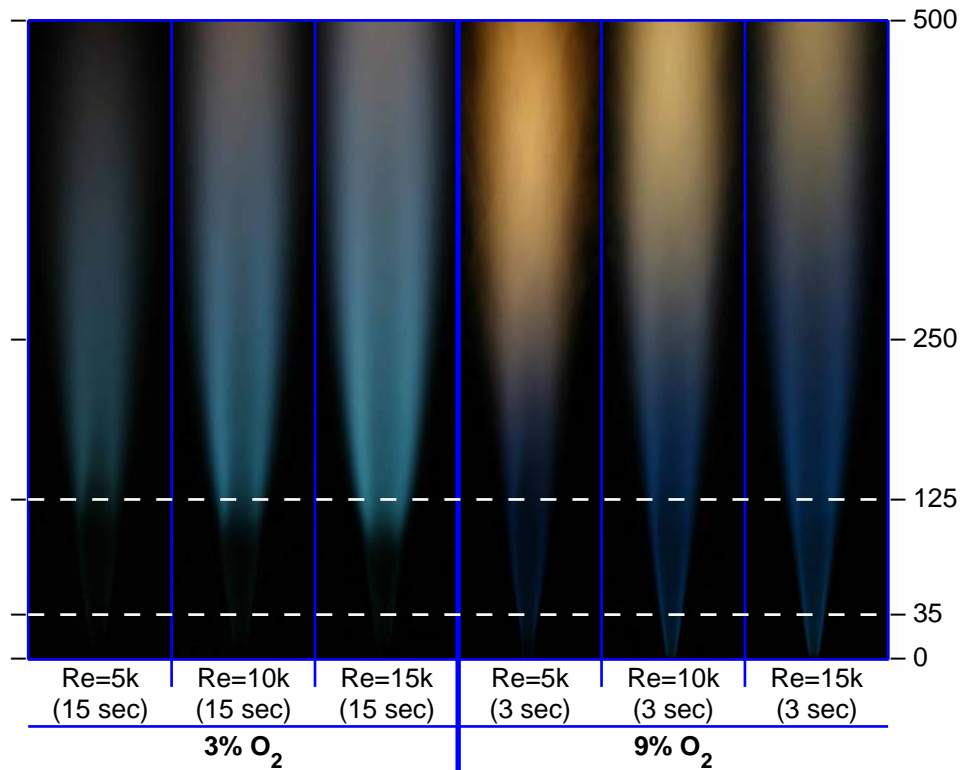
Figure 4.1: Photographs of natural gas/hydrogen (1:1 vol/vol) flames at two coflow O_2 levels. Jet Reynolds number from 5000 to 15,000. Note the different exposure times (all other camera parameters held constant). Horizontal lines indicate measurement locations (35mm & 125mm downstream of jet exit plane). Photograph height: 500mm.

4.3 Visual Observations

Figure 4.1 shows photographs of the flames presented in this chapter. It is clear that the flames have different features at the two measurement locations indicated, namely 35mm and 125mm above the fuel jet exit plane. These locations were chosen to represent two oxidant regimes. At the 35mm location, the oxidant stream is that of the coflow (with a specified O_2 level). At the 125mm location, air from the surrounds is entrained with the coflow stream (Figure 3.2 in §3.2.1) resulting in a different oxidant composition than at the 35mm location.

From the photographs, especially considering the difference in exposure time, it is apparent that the 3% O_2 coflow flames have very low luminosity. The flames appear faint to look at, and it is rather difficult to distinguish the flame brush.

Fuel	Re_{jet}	Coflow O_2	Flame length
NG/H$_2$	5,000	3%	1200mm
NG/H$_2$	10,000	3%	1200mm
NG/H$_2$	15,000	3%	1400mm
NG/H$_2$	5,000	9%	600mm
NG/H$_2$	10,000	9%	800mm
NG/H$_2$	15,000	9%	1000mm

Table 4.3: Visible flame length of natural gas/hydrogen flames

Noteworthy is that the flames with 3% O$_2$ in the coflow are virtually free of visible soot for the full length of the flame. While for the 9% case soot appears at around 250mm downstream of the jet exit. It is known that the effects of the coflow persists around 100–150mm downstream. Soot is absent beyond the known extent of the coflow, suggesting that kinetics in the early regions of the flame play a major role in the soot formation path.

While not necessarily clear from Figure 4.1, for all Reynolds numbers the total visible flame length at 3% O$_2$ is longer than for the higher 9% O$_2$ case. Table 4.3 presents the approximate flame length based on visual observation. It is apparent that the differences in the flame length between the two coflow O$_2$ levels are more noticeable at lower jet Reynolds numbers.

4.4 Instantaneous Images – 35mm downstream

Figures 4.2a & 4.2b show typical instantaneous image triplets of OH, H$_2$CO and temperature at the 35mm location for two coflow stream O$_2$ levels. These images are for a jet Reynolds number of 15,000 and are typical of other Reynolds number flames as well. The corresponding size of each image is 8×35mm.

The spatial location of H$_2$CO on the fuel-rich side, in relation to OH, reinforces that H$_2$CO is a first-step intermediate [14] formed as a product of fuel decomposition [65]. The broad radial profile distributions of H$_2$CO presented here are consistent with previously reported nonpremixed flames [52, 110]. It is emphasised very early that later evidence will prove the broad radial distribution of
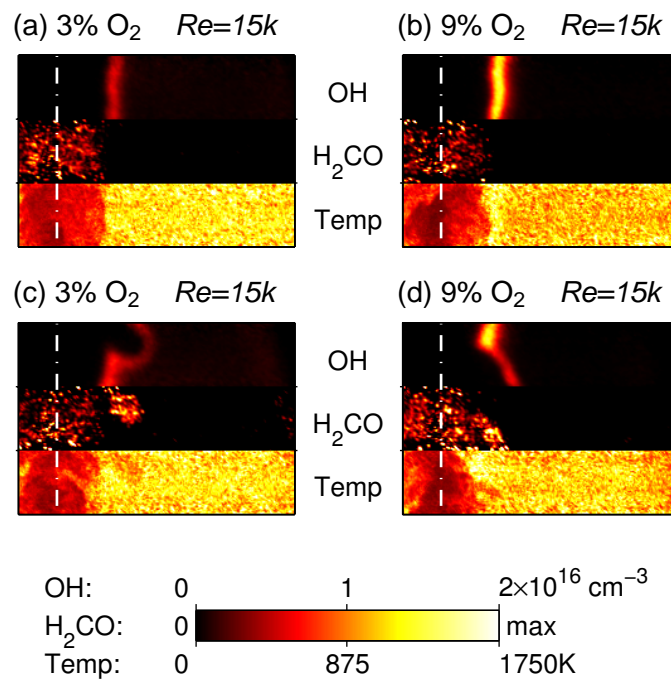
Figure 4.2: Selection of instantaneous OH, H_2CO and temperature image triplets showing typical features (irrespective of Reynolds number) of natural gas/hydrogen flames. Each image 8×35mm. Jet centreline marked with dashed line. Axial location 35mm above jet exit.
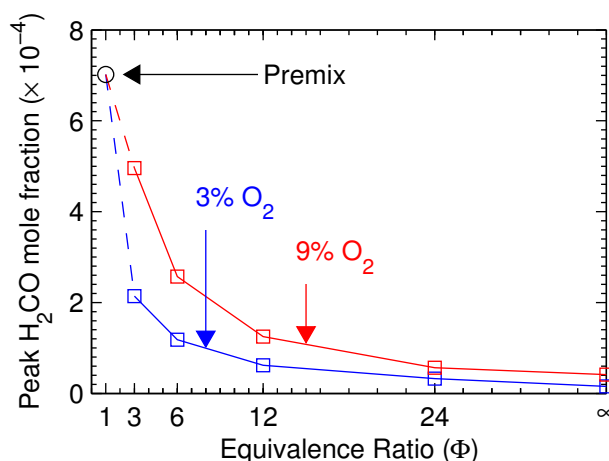
Figure 4.3: Calculated peak H_2CO mole fraction plotted versus equivalence ratio for a methane/hydrogen fuel mixture for two oxidant stream O_2 levels.

H_2CO is not due to PAH or Raman interference. In §6.6 laminar flame calculations are presented which show that H_2CO exists almost throughout the entire mixture fraction space for these hot and diluted conditions.

The temperature images show a uniform temperature distribution in the coflow stream, and for the 9% O_2 coflow a distinct peak close to the reaction zone. For the 3% O_2 case the temperature peak is barely discernable, however a definite OH layer is measured, albeit at lower OH levels than for the 9% case. Similar observations regarding the very low, almost indistinguishable temperature rise across the reaction zone has been seen in a similar high temperature oxidant stream environment [47] and also in a MILD combustion furnace [88]. The lack of apparent temperature rise has been discussed in §3.9.4. The low temperature is believed to be genuine, and not because of interferences or problems with the Rayleigh to temperature conversion process.

At different jet Reynolds numbers the images show similar features. Nonetheless, at higher Reynolds numbers a greater proportion of the instantaneous images show signs of convolution and a weakening (reduction) of the OH distribution, examples of which are shown in Figures 4.2c & 4.2d. In images where the OH is reduced, the H_2CO levels show a noticeable increase. The reduction in reaction rates at low O_2 levels and the weakening of OH and subsequent increases in H_2CO are more noticeable with a 3% O_2 coflow.
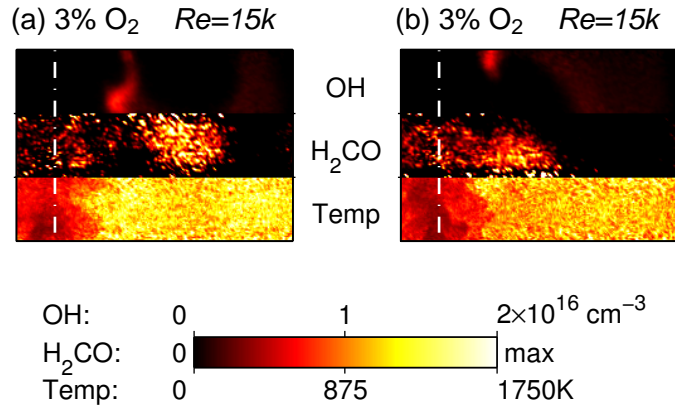
Figure 4.4: Selection of instantaneous OH, H_2CO and temperature image triplets showing wide radial distribution of H_2CO of natural gas/hydrogen flames. Each image 8×35mm. Jet centreline marked with dashed line. Axial location 35mm above jet exit.

Partial premixing has been shown to significantly increase H_2CO levels in hydrocarbon flames [77, 78]. Figure 4.3 presents calculated peak H_2CO mole fractions using the OPPDIF code of the Chemkin package and the GRI-Mech 3.0 mechanism for a single fixed flow velocity at various fuel stream equivalence ratios beyond the fuel-rich limit. For either oxidant stream composition (Table 4.2) it is clearly apparent that increasing the level of partial premixing leads to a significant increase in the peak H_2CO concentration. At stoichiometric conditions ($\Phi=1$) the peak H_2CO level has also been determined, using the PREMIX code of the Chemkin package and again the GRI-Mech 3.0 mechanism. The flame calculations are described in Appendix A.7.

Figures 4.4a & 4.4b show images with very strong H_2CO on the oxidant side of the reaction zone. These images suggest that partially premixed unreacted fuel exists at these wide radial locations. For each Reynolds number, the image set has been visually analysed to record the number of images where H_2CO is seen to exist at wide radial locations. The frequency of images (i.e. the number of images with wide radial H_2CO distribution, normalised by the total number of images ($\sim$400) for each Reynolds number) showing evidence of such mixing is $\sim$1.1%, $\sim$4.4% and $\sim$5.1%, in ascending order of the three Reynolds numbers considered in this chapter.

The observation of H_2CO in the coflow initially appears to indicate that this may

Re_{jet}	3% O_2	9% O_2
5,000	2.02mm	1.68mm
10,000	2.04mm	1.81mm
15,000	2.09mm	1.85mm

Table 4.4: Mean OH width estimates at 35mm downstream location for natural gas/hydrogen flames at two coflow O_2 levels and three Reynolds numbers.

be an issue relating to the secondary burner, however, this is not believed to be the cause. This phenomenon is not noted in any of the other flame conditions in subsequent chapters, and the frequency of these occurrences is clearly dependent on the jet Reynolds number. These two observations point towards H_2CO in the coflow being an effect of the jet rather than the secondary burner.

Estimates of the mean thickness (FWHM) of the OH layer from the instantaneous images are shown in Table 4.4. This table is generated by examining the full-width half-maximum in each row of each image and then averaging. As expected, the reduced oxygen concentration requires a greater volume of oxidant stream to consume the fuel, as such the 3% O_2 coflow flames have a thicker width of the OH region as compared to the 9% O_2 case. The thickness increases slightly with Reynolds number, consistent with previous work [60]. The change in the width of the OH with Reynolds number is less than 1 pixel (160µm), but since the results are averaged over the entire set, a trend is still clearly apparent. The less prevalent increase in thickness with Reynolds number at the lower O_2 level may possibly be due to an increased decay of turbulence levels under these diluted conditions.

4.5 Radial Profiles – 35mm downstream

Figure 4.5 shows the mean and RMS radial profiles of OH, H_2CO, and temperature for both 3% and 9% O_2 at various jet Reynolds numbers, and at an axial location 35mm above the jet exit plane. Each plot is generated only from the central 3mm strip of the images, and not from the entire sheet height, so as to avoid potentially over-corrected values towards the edge of the images where the low laser energy possibly makes sheet corrections less reliable.
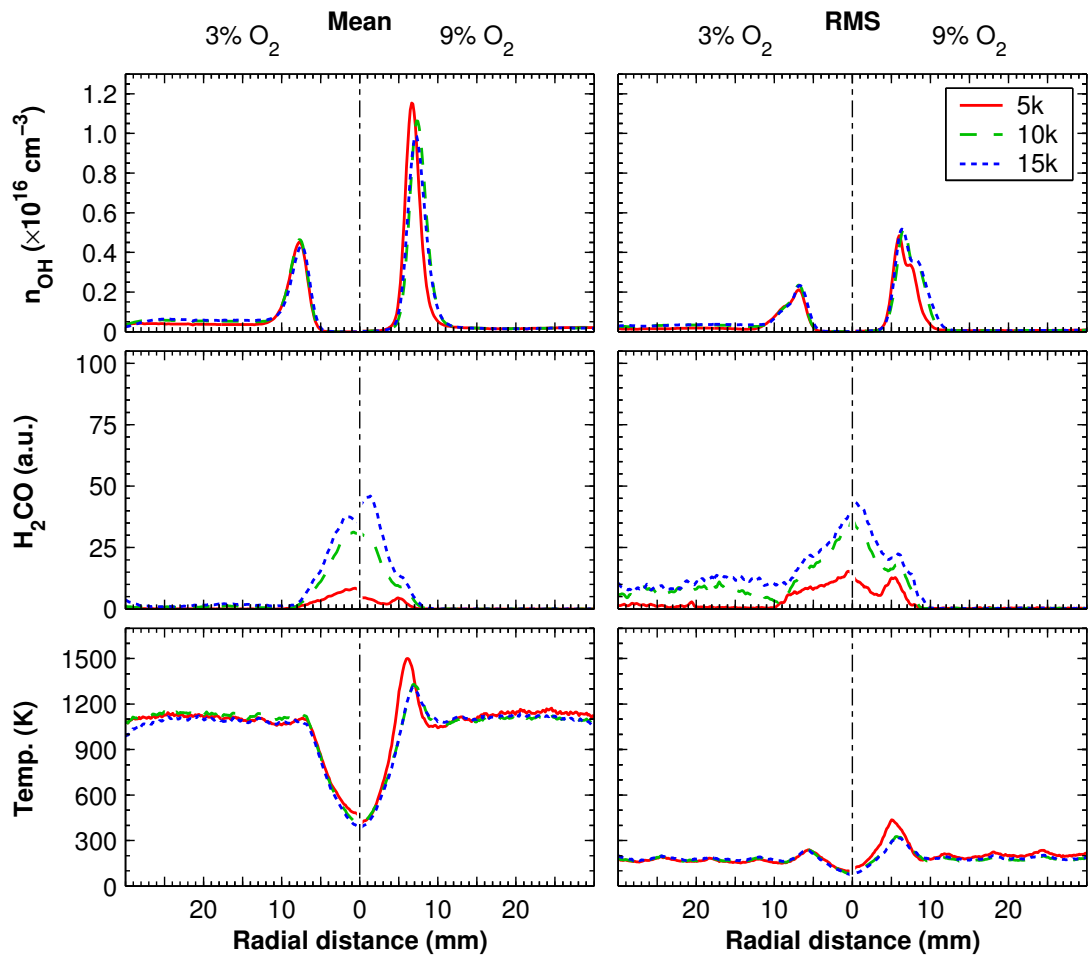
Figure 4.5: Mean and RMS radial profiles for OH, H_2CO and temperature of natural gas/hydrogen flames at two coflow O_2 levels. Jet Reynolds numbers ranging from 5000 to 15000. Central 3mm strip of images used. Axial location 35mm above jet exit.

From Figure 4.5 it is seen that reducing the coflow O_2 level leads to a substantial suppression of OH, as already noted in the instantaneous images of Figure 4.2. This observation is consistent with previous work (e.g. [94]) and is directly related to the reduced temperature of the reaction zone. The 3% O_2 coflow case shows a radial shift of the OH peak towards the oxidant stream of ∼1mm relative to the 9% O_2 case. This radial shift is consistent with a three-fold drop in stoichiometric mixture fraction at the 3% O_2 conditions. Also apparent is that the Reynolds number does not seem to have a significant influence on the mean or RMS profiles of OH at either O_2 level, although minor differences are apparent at the 9% coflow case. Minor equilibrium OH levels in the coflow stream are also observed.

An increase in jet Reynolds number has a marked effect on H_2CO mean profiles. Between $Re_{jet} = 5000$ and 15000, the mean H_2CO increases by a factor of ∼4.4 for the 3% O_2 coflow case and ∼10.4 for the 9% O_2 case. A similar trend has been observed in strained laminar nonpremixed flame calculations (to be presented in §4.7.3), and has also been briefly noted by others [110], though not quite to the extent observed here. The broad radial distribution is consistent with the typical instantaneous images previously presented. The observation of H_2CO along the centreline is related to the very broad distribution of H_2CO in mixture fraction space, and will be discussed in further detail in §6.6.

As already seen from the instantaneous images (Figures 4.4a & 4.4b), transfer of jet fluid into the coflow results in significant increases in H_2CO levels. This is reflected in the H_2CO RMS profiles of Figure 4.5. At 3% O_2 there is a much higher H_2CO RMS at wider radial locations, indicating a greater proportion of unreacted jet fluid penetrating the reaction zone. This is directly related to the less intense reaction zone at the lower O_2 level.

Due to the low O_2 levels, the temperature peak under MILD combustion conditions is expected to be only slightly above the coflow temperature. As expected from the instantaneous images, in the mean there is no clear discernible peak for the 3% O_2 coflow case despite the OH clearly indicating a reaction taking place. For the higher 9% coflow case, the mean temperature rise is only 200–400K. It is worth noting that the peak temperatures are lower than what has been previously reported by Dally et al. [31], and may be primarily attributed to the lower temperature coflow of the present study (1100K compared to 1300K).

The influence of jet Reynolds number on both OH and temperature appears quite minor at this location. Both the mean and RMS levels of OH remain essentially constant over the range $Re_{jet} = 5000 - 15000$, however a slight (1mm) outward radial offset of the OH peak location is observed for the lowest jet Reynolds number at the 9% O_2 coflow. Similarly, the temperature profiles are consistent, again with only slight variations being noted at the lowest jet Reynolds number. The RMS of the temperature is relatively low in the shear layer, even at high Reynolds numbers.

4.6 Results – 125mm downstream

At 125mm downstream it is visibly evident that the flames are perceptibly different in structure, as seen in Figure 4.1. At this location the surrounding air is able to penetrate the coflow, subsequently having an influence on the flame structure. There remains clear differences between the 3% and 9% O_2 coflow cases at this location however, particularly evident in the differing mean radial profiles of the H_2CO seen in Figure 4.6. As highlighted previously for Figure 4.5, Figure 4.6 is generated only from the central 3mm strip of the images, and not from the entire sheet height.

Mean plots of OH and temperature again show minor differences with jet Reynolds number for either coflow case. Differences in the peak temperatures between O_2 levels are $\sim$250K and $\sim$100K along the centreline. The RMS of the OH and H_2CO at this location in percentage terms are approximately double those at 35mm downstream. As expected, at this 125mm downstream location the radial profiles are significantly broader than for the radial plots (at 35mm) in Figure 4.5. The temperature profiles of Figure 4.6 clearly indicate that the influence of the coflow has diminished at the 125mm downstream location as evident by the low temperatures at wider radial locations. For the 9% O_2 at this location the trend of H_2CO increasing with Reynolds number is reversed in relation to what is seen in the other measurements. Occasionally the H_2CO signal in this image set is seen to be much higher than typical levels, having the effect of skewing the mean and is clearly apparent in the very high RMS of the low jet Reynolds number cases.
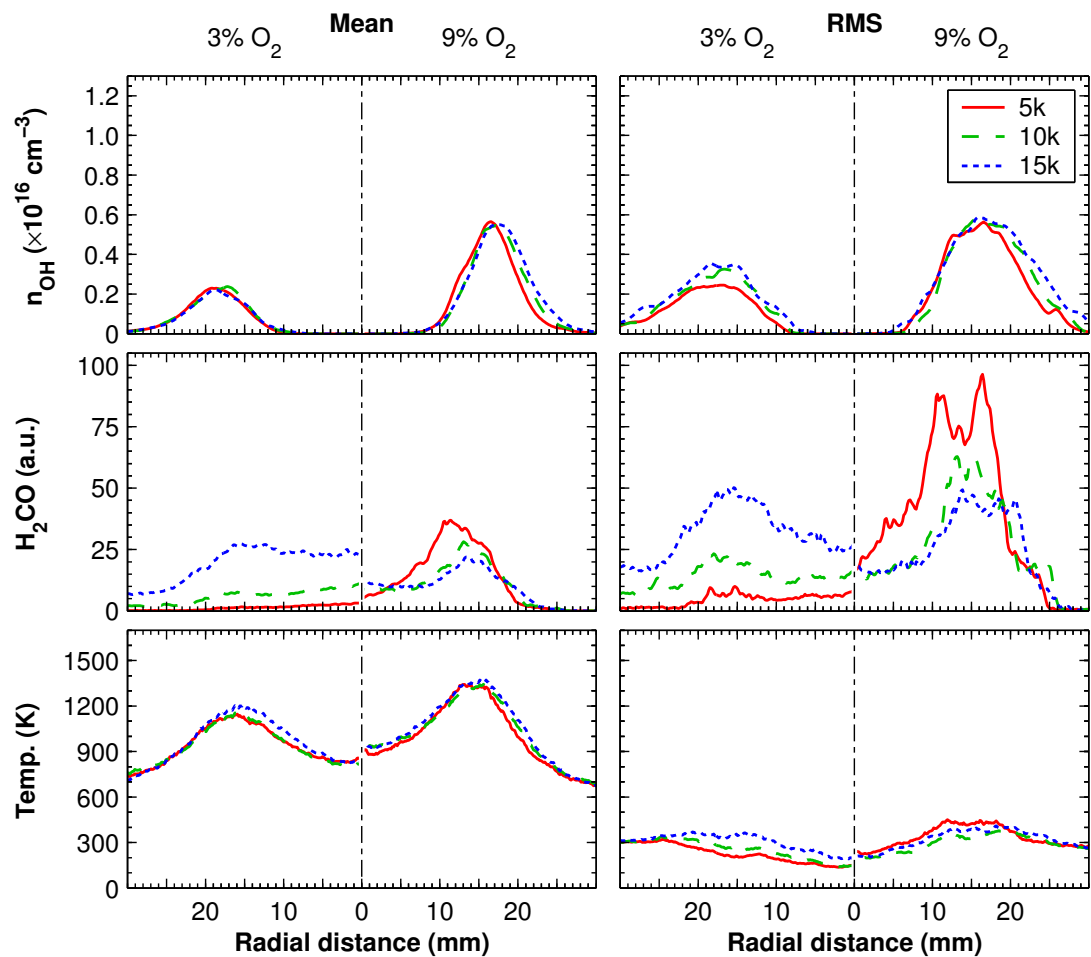
Figure 4.6: Mean and RMS radial profiles for OH, H$_2$CO and temperature of natural gas/hydrogen flames at two coflow O$_2$ levels. Jet Reynolds numbers ranging from 5000 to 15000. Central 3mm strip of images used. Axial location 125mm above jet exit.
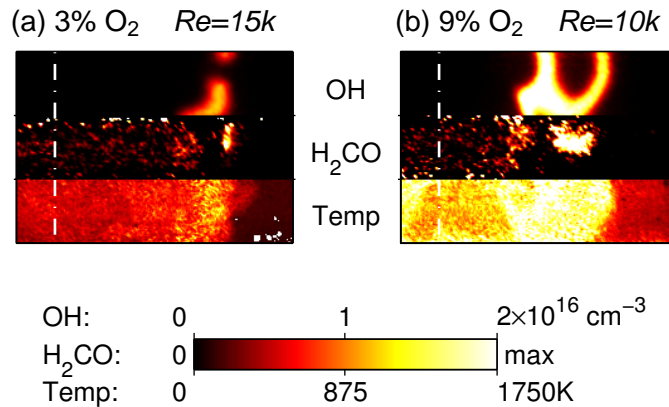
Figure 4.7: Selection of instantaneous OH, H_2CO and temperature image triplets showing effects of surrounding air entrainment on natural gas/hydrogen flames. Each image 8×35mm. Jet centreline marked with dashed line. Axial location 125mm above jet exit.

Figure 4.7 shows instantaneous image triplets at the 125mm location. In both of the temperature images a cold region of entrained air is seen on the oxidant side (righthand side). Localised extinction is evident in Figure 4.7a, as indicated by the rupture of the flame front in the OH image. The subsequent break in the flame front has allowed fuel to mix with the air, and the elevated temperature in this region ($\sim$900K) has initiated a partially premixed flame, evident by the increased H_2CO levels in the area adjacent to the OH break.

Figure 4.7a clearly indicates that the entrainment of cold air at the downstream location (125mm) has a substantial effect on the reaction zone. With the inclusion of surrounding air, the associated drop in temperature can lead to a local extinction of the flame front, based on the OH and temperature images. The nature of such extinction events is attributed to cooling.

Whilst cold air coming into contact with the reaction zone can lead to extinction, the higher O_2 level of the air can also lead to an increase in the reaction intensity (increases in both OH and the local temperature). As evident in the non-extinguished parts of image Figure 4.7a, the OH concentration is higher than seen in the typical images at the 35mm location.

It is proposed that the effects of the surrounding cool air at the furthest down-

stream location takes place in a series of steps. The first step is the extinction due to cooling by the surrounding air. The subsequent rupture or weakening of the flame front allows the fuel and the air to premix. The partially premixed region ignites, evident by the H_2CO levels increasing. Due to the increased oxygen levels, this newly formed reaction zone has a higher reaction intensity and subsequently higher OH and temperature.

The trend of entraining surrounding air tending to increase H_2CO levels and subsequently OH and temperature occurs at the 9% O_2 coflow as well. At this higher O_2 level, the increased reaction rate tends to make the flame front far more resilient to rupture by these entrainment events. The effect of air entrainment increasing the H_2CO due to premixing and the resultant increases in OH and temperature may still be noted at the 9% O_2 coflow in Figure 4.7b. Although the inclusion of higher O_2 air may tend to increase the OH and temperature due to increased reaction rates, until adequate mixing has occurred the O_2 influence does not necessarily increase the OH and temperature, as shown in Figure 4.8a.

Extinction of the flame front due to cooling does not necessarily require room temperature air, rather a lower temperature region. Figure 4.8b is an example of this. Here, a cooler (but not cold, T~550K) region may be seen between and beneath the two small regions of OH, and it is this lower temperature which is believed responsible for this extinction event. Again, associated with this extinction is the interaction of the fuel and oxidant giving rise to a partially premixed region evident by the strong H_2CO. The comparatively low signal of each species indicates that this is a recent extinction event, whereby the partially premixed flame has not yet had a sufficient opportunity to increase the OH and temperature.

Figure 4.8c shows another example of an extinction event. This time however it appears to be towards the end of it, whereby the OH appears to be dominating and the higher temperatures indicate that the reaction has recovered following a re-ignition. Only a small partially premixed pocket remains where the H_2CO persists. Despite an extinction event via cooling (albeit not by entirely cold room air), the flame front has re-established. Figure 4.8d also shows another extinction event where the OH and temperature have recovered. The strong H_2CO present in this image is expected to soon be consumed.
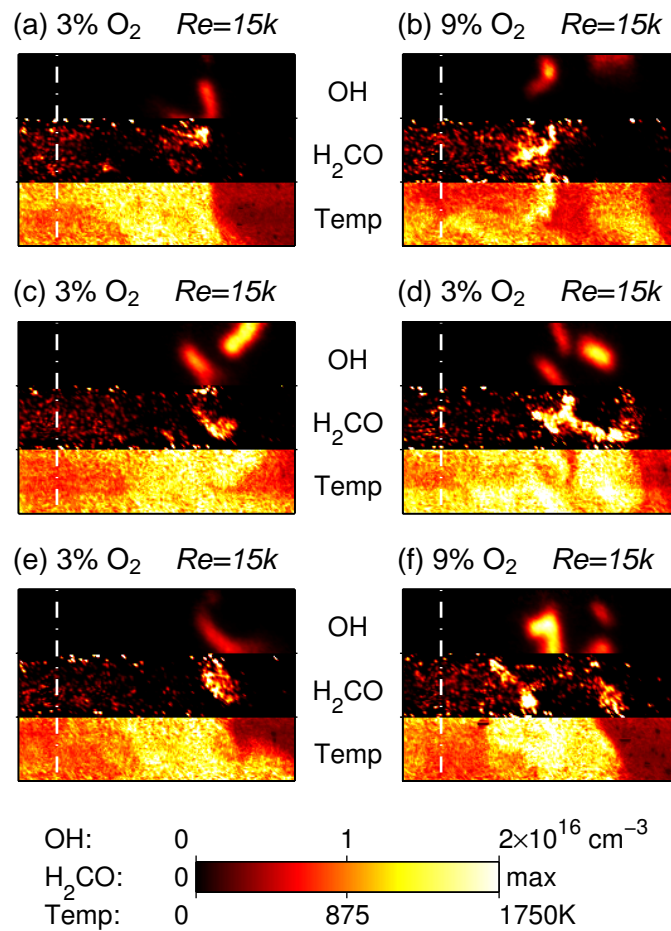
Figure 4.8: Selection of instantaneous OH, H_2CO and temperature image triplets showing localised extinction events of natural gas/hydrogen flames. Each image 8×35mm. Jet centreline marked with dashed line. Axial location 125mm above jet exit.

A large-scale vortex is noted in Figure 4.8e. The H_2CO "island" at a wider radial location than the OH indicates that fuel is present on this outer side. The higher temperatures on the inner side of the OH tends to suggest that this region has in fact been fluid from the coflow which has been forced towards the jet centreline. The high temperature and low O_2 level of the oxidant results in the OH levels being comparable to the controlled 3% O_2 flames at the 35mm downstream location. This image therefore indicates that a disturbed flame front can retain the features of a controlled flame providing the local environment is suitable.

Figure 4.8f shows examples of both situations in the extinction cycle. On the outer side, cold fresh air has lead to a rupture of the OH, enabling a small pocket of premixing, and the production of H_2CO, indicating that fuel has reached the cold air surrounds. Temperatures on this side, even where OH is present, are low. Overall, this appears to be indicative of a recent extinction event. On the jet side of the high temperature region, a much stronger band of OH is seen. Just to the inside of the strong OH and temperature, the presence of strong H_2CO and a corresponding region of cooler temperatures tends to indicate that in this area surrounding air has been entrained which caused a brief extinction, followed by partial premixing and consequently leading to the higher OH and temperature on this side of the image.

Overall, the extinction events identified do not indicate that the entire flame becomes extinct. Rather the flame front becomes locally and instantaneously broken. The localised extinction is accompanied by the formation of H_2CO, indicating that the reaction has recommenced. This re-ignition process is initiated by the heated coflow, which acts as a pilot. Although there is evidence of cold surrounding air penetrating the coflow and leading to temporary extinction at the most downstream location, there are enough hot products to ensure that the temperature is high enough to sustain the overall reaction.

Although no extinction events are seen at the higher (9%) O_2 case, similar trends relating to surrounding air entrainment may be observed in the images. For example, Figure 4.7b shows evidence of entrained cooler air and subsequent premixing which has lead to the island of high H_2CO, surrounded by high OH and temperature – exactly the same as noted for the 3% O_2 cases. The difference at
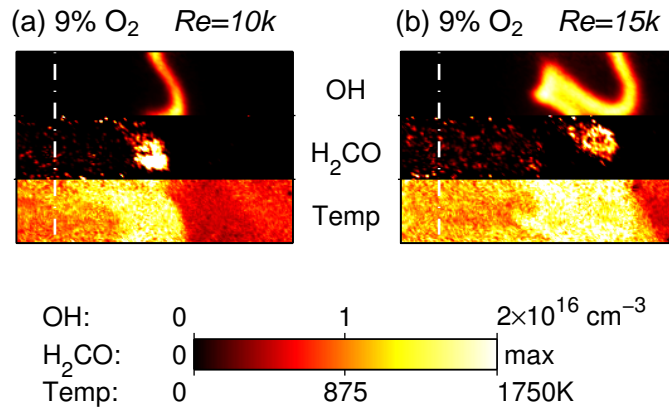
Figure 4.9: Selection of instantaneous OH, H_2CO and temperature image triplets showing effects of oxygen leakage on natural gas/hydrogen flames. Each image 8×35mm. Jet centreline marked with dashed line. Axial location 125mm above jet exit.

the higher oxygen levels is that the initial reaction zone is more intense, consequently, the entrainment of surrounding air serves only to weaken the reaction zone rather than to cause extinction. An example of the weakened reaction zone at the 9% O_2 coflow is seen in Figure 4.9a. As a result of the weakened (but not extinguished) reaction zone, oxygen leakage from the surrounding air has penetrated the flame front. This in turn has lead to an increase in H_2CO in the vicinity of the weakened OH.

Even in situations where there is not necessarily cold air "pockets", but clearly there has been some form of surrounding air entrainment as indicated by the strong H_2CO levels, the OH and temperature levels still increase markedly, as seen in Figures 4.8d and 4.9b.

4.7 Discussion

4.7.1 Extinction at Furthest Downstream Location

At the most downstream location (125mm), the instantaneous images presented in this chapter suggest that the entrainment of surrounding air can lead to lo-

Re_{jet}	3% O_2	9% O_2
5k	1.5%	0%
10k	11.9%	0%
15k	33.7%	0%

Table 4.5: Proportion of images with evidence of extinction at 125mm location for natural gas/hydrogen flames at two coflow O_2 levels.

calised extinction of the reaction zone by means of cooling. It is surmised that the extinction process goes through the following stages;

- Cold (cool) air from the surrounds causes a localised break in the flame front, indicated by a rupture of the OH

- Fuel, coflow and the surrounding air mix, leading a to local partially pre-mixed region

- The elevated temperatures result in ignition of the partially premixed pocket. A partially premixed reaction is evident by high H_2CO levels

- The additional oxygen concentration within the partially premixed pocket subsequently leads to a higher intensity reaction than the nonpremixed reaction zone, resulting in higher OH and temperature

The suggestion that extinction is by cooling is brought about by the associated decreases in temperature in conjunction with the increase of H_2CO in such images. In images with apparent local extinction a region can be identified with evidence of entrainment, typically with lower temperatures. The presence of strong H_2CO at the location of extinction events is suggestive of partial premixing with greater oxygen levels than in the coflow stream, suggesting interaction with the surrounding air. The H_2CO which is seen in the instances of local extinction suggests that these extinction effects are genuine and not falsely identified due to out-of-plane effects, which are minimised due to the streaming nature of this flow.

From analysis of all of the images at the 125mm location, for each flame condition ($\sim$400 images per case), the proportion of images with evidence of extinction is shown in Table 4.5. The increased frequency of extinction events with increased

Reynolds number may initially appear to point towards strain induced extinction. From the evidence seen in these images, as already outlined, it is speculated that cooling leads to these extinction events rather than strain. The frequency of extinction increasing with Reynolds number is attributed to increased mixing, entraining more surrounding air and so leading to a higher frequency of extinction events. This conclusion is reinforced by the observation that the extinction events at all Reynolds numbers have the same structure – it is merely the frequency of extinction that changes with Reynolds number. Further evidence that strain is unlikely to lead to extinction is noted in laminar flame calculations, and has also been noted previously under similar hot and diluted conditions [76]. Heating of the oxidant stream raises the extinction strain rates to higher levels than possible for a 21% O_2 and 300K temperature in the oxidant stream.

The intimation that at the most downstream location (125mm) localised extinction takes place via cooling has previously been suggested in turbulent jet piloted diffusion flames and bluff-body flames [60, 75].

Having identified, from Table 4.5, that Reynolds number has a significant effect on the extinction processes at the 3% O_2 case, it would be expected that the OH RMS plots of Figure 4.6 would reflect this as well. Figure 4.6 reveals a variation in the 3% O_2 OH RMS peak and radial width of the RMS profiles, such that the RMS is higher at increased Reynolds numbers. The differences with Reynolds number in Figure 4.6 may not seem as substantial as expected based on the statistics presented in Table 4.5, however. This difference is due to the different sheet heights used to construct each of these data results. For the statistics of Table 4.5 the entire image height (8mm) was used to determine extinction events, whereas for Figure 4.6 only the central radial strip (3mm high) at the identified axial distance was used. A narrower region was used for the radial plots to avoid over-corrected values towards the edges of the images where the low laser power makes the sheet corrections less reliable, and also to reduce spatial averaging effects. Since the radial profile (Figure 4.6) includes a smaller imaging area there is a reduced likelihood of an extinction event being captured within this narrower region. It is imperative to note however that the different interrogation region has no bearing whatsoever on the significance of the findings, and does not influence the trend with the jet Reynolds number.

OH number density ($\times 10^{16}$ cm^{-3}) [σ]				
Location	Coflow	5k	10k	15k
35mm	3% O_2	0.67 [9%]	0.72 [10%]	0.70 [11%]
	9% O_2	1.55 [7%]	1.59 [9%]	1.60 [10%]
125mm	3% O_2	0.78 [22%]	0.93 [45%]	1.01 [52%]
	9% O_2	1.72 [11%]	1.77 [13%]	1.81 [16%]

Table 4.6: Mean and standard deviation (σ) of peak OH number density for natural gas/hydrogen flames.

4.7.2 Effect of Coflow O_2 Level

Near the jet exit, where the oxidant composition is entirely controlled by the hot coflow, it has been shown that a reduction in O_2 concentration leads to a suppression of OH, directly related to the drop in temperature. Another consequence of reducing the O_2 level is a slight broadening of the width of the OH region.

Reynolds number effects on the structure of these flames appears minimal based on the mean and RMS radial profiles at either axial location. The maximum of these plots does not necessarily represent the mean peak OH number density however, as a result of the inherent spatial averaging. Instead, from each image the peak OH number density has been determined. The mean of the peak from each image gives a better indication of the mean peak OH number density. Shown in Table 4.6 is the mean of the peak OH value in each of the images in the set, also presented is the standard deviation of these peak values throughout the set.

As already noted in the mean OH plots of Figures 4.5 & 4.6, Table 4.6 reinforces the notion that the coflow O_2 level dramatically affects the OH. The OH levels approximately double when the O_2 concentration is increased from 3% to 9% in the coflow. A feature noted in Table 4.6 which was not seen in the mean radial plots however is the increase of mean peak OH number density at the 125mm downstream location. For the 3% O_2 coflow, the peak OH number density in the radial plots dropped from $\sim 0.45 \times 10^{16}$ cm^{-3} at the 35mm location to $\sim 0.25 \times 10^{16}$ cm^{-3} at the 125mm downstream location, and is largely independent of the Reynolds number. Whereas Table 4.6 shows the opposite trend of an increase in the mean peak OH further downstream and this increase is highly dependent on the Reynolds number. The difference between the two downstream

locations is due largely to the effects of the surrounding air entrainment. The additional O_2 levels as a result of the entrainment leads to an increase in the OH, as already noted in the instantaneous images. This effect is masked in the radial plots due to the spatial averaging.

Close to the jet exit (35mm location), as expected, the standard deviation of the OH number density is quite low ($\sim$10%) for either coflow or Reynolds number. Further downstream the interactions with the surrounding air lead to more significant fluctuations, as evident by an increase in the standard deviations, especially for the 3% O_2 case due to localised extinction events. At the 125mm location, additional variations are also noted with increased Reynolds number, as was previously observed in Table 4.5. The significant influence of Reynolds number on the 3% O_2 125mm downstream data is an artefact of the increased turbulent stirring resulting in greater entrainment of surrounding air, subsequently leading to extinction events. Naturally, the increased intermittency of the OH as a result of the extinction–reignition process leads to the increase in the standard deviation in the peak OH levels.

The influence of surrounding air entrainment at the downstream (125mm) location on the OH levels in the instantaneous images has already been noted (§4.6). Particular attention is drawn to the instance of air entrainment in Figure 4.7b, where the OH number density is almost 3×10^{16} cm^{-3}. In comparison, in the typical images at the 35mm downstream location the OH number density does not exceed 2×10^{16} cm^{-3}. The increase in the OH concentration reiterates the intimation that the inclusion of higher O_2 levels leads to increases in OH concentration beyond that expected in the diluted conditions.

4.7.3 Strain Effects

The mean peak OH number density at the 35mm location can be compared to laminar flame calculations. Calculations for both 3% and 9% O_2 oxidant streams (T_{oxi}=1100K) have been performed over a range of strain rates using the OPPDIF code of the Chemkin package and the GRI-Mech version 3.0 mechanism. The flame calculations are described in Appendix A.8. The results presented in Figure 4.10 show that the OH number density steadily increases with strain at
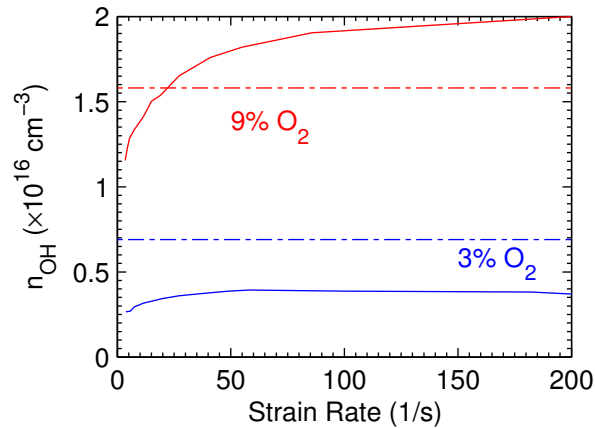
Figure 4.10: Calculated peak OH number density plotted versus strain rate found from laminar flame calculations for methane/hydrogen fuel at two oxidant stream O_2 levels. The overlaid horizontal dashed lines are the peak experimental results.

low strain conditions, before levelling out for strain rates above approximately $100s^{-1}$. The drop in the OH concentration at low strain conditions is believed to be related to radiation effects, and at very low strain rates flame extinction can occur because of this effect [49, 73].

Overlaid on Figure 4.10 are the experimental results from Table 4.6 for the 35mm location. The flame calculations are for laminar conditions rather than turbulent flames, and so the flame calculation are only indicative of the OH number density. It is apparent that there are noticeable variations in the OH number density of the experimental results and the laminar flame calculations. At 3% O_2 the calculations under-estimate the OH number density, whereas at 9% O_2 the experimental results are slightly below the maximum OH number density from the calculations. The overlap between the experimental results and model for 9% O_2 indicates that $20s^{-1}$ typifies the average strain rate in the flames. These are nominally turbulent flows and this strain rate seems rather low, possibly implying an increased decay of turbulence levels under these hot diluted conditions. The mooted concept of reduced turbulence levels under MILD conditions may be speculated to be as a result of the diminished thermal gradients across the reaction zone, further enhanced by the viscosity effects due to the elevated temperature of the oxidant stream. This inference is consistent with the previously noted observation of jet Reynolds number having only minor influence on the
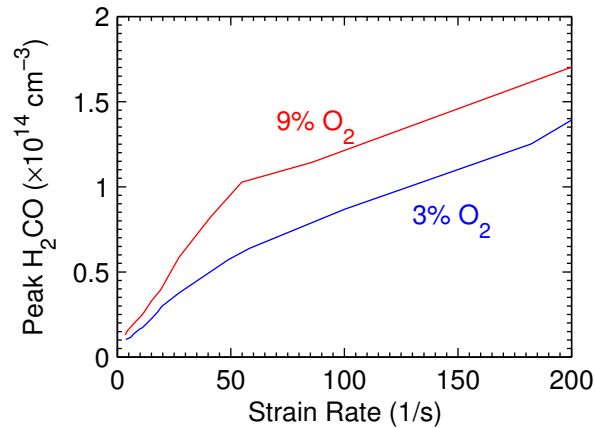
Figure 4.11: Calculated peak H_2CO number density plotted versus strain rate found from laminar flame calculations for methane/hydrogen fuel at two oxidant stream O_2 levels.

mean and RMS radial profiles (Figure 4.5).

To provide an estimate of a characteristic strain rate for the experimental conditions, the OH width from the laminar flame calculations can be compared to the measured width. Table 4.4 indicated that the nominal OH thickness (FWHM) for the 3% O_2 level is around 2mm, and slightly less for the 9% O_2 coflow. From the laminar flame calculations, a strain rate of $\sim 30s^{-1}$ seems provide a OH thickness approximately consistent with the measurements.

The strain rate is related to the jet velocity, hence the jet Reynolds number. As the strain rate in the calculations is increased, the OH width becomes thinner. In contrast, as the Reynolds number is increased Table 4.4 indicates a slight broadening of OH width. The increase in OH thickness with Reynolds number is not attributed to strain, rather, the development of a greater number of small-scale vortices. These unresolved vortices are believed to lead to an apparent broadening of the OH layer. As such, the strain rate of $\sim 30s^{-1}$ may be an under-estimate of the actual strain rate in the flames.

While the strain rate effects on the OH appear quite minor, it has already been seen in Figure 4.5 that with increased Reynolds number (hence strain) the H_2CO levels increase. To examine the role of strain on this increase, Figure 4.11 shows the peak H_2CO number density for CH_4/H_2 flames at various strain rates, found

from strained laminar flame calculations using the OPPDIF code of the Chemkin package and the GRI-Mech version 3.0 mechanism. These are the same conditions as used for Figure 4.10, but here the peak H_2CO number density is plotted instead of OH. Clearly apparent from Figure 4.11 is that unlike OH (Figure 4.10) the peak H_2CO number density does indeed increase with the strain rate. This increase in H_2CO with strain is consistent with the noted effects of Reynolds number.

Accompanying the increase in strain with Reynolds number is also an increase in turbulent mixing due to vortical structures. These vortices both increase the local strain, and also lead to mixing with the oxidant stream. It has already been shown in Figure 4.3 that partial premixing increases the H_2CO concentration. The combination of strain and mixing with an increase in Reynolds number explains the significant increases in H_2CO levels seen in Figure 4.5.

Chapter 5

Diluted Ethylene Flames

5.1 Introduction

The combination of OH, formaldehyde (H_2CO) and temperature, in turbulent nonpremixed diluted ethylene (C_2H_4) flames issuing into a heated and diluted coflow, are reported in this chapter. The hot and diluted oxidant is produced by the JHC (Jet in Hot Coflow) burner (§3.2.1). Comparisons are made between different fuel compositions (ethylene undiluted, or diluted with hydrogen, air, or nitrogen) at a fixed jet Reynolds number (Re_{jet}=10,000) and two coflow oxygen levels. Measurements are taken at two downstream locations. At the furthest downstream location the effects of the entrainment of surrounding air on the flame structure are examined.

Previous experiments have concentrated on methane fuel [2, 30, 31] due to its relatively simple chemistry. In order to bridge the gap to practical fuels, there is a need to investigate more complex hydrocarbons. Ethylene is an important intermediate in the oxidation of higher-order hydrocarbons, therefore making it suitable to examine the effects of such fuels [77]. It is also an important species in the production of precursors leading to soot formation [106]. Mixing ethylene with inert as well as air and hydrogen have been used in the past to reduce soot. As MILD combustion relies on effective mixing with inert and oxygen, understanding the effect of each diluent in isolation aims to advance the understanding of these effects.

Fuel (mol/mol)	Re_{jet}	$\dot{Q}$ [L$_n$/min]	$\bar{v}_{exit}$ [m/s]
C_2H_4	10,000	17.4	19.2
C_2H_4/H_2 (1:1)	10,000	30.5	33.6
$C_2H_4/$Air (1:3)	10,000	27.2	45.0
C_2H_4/N_2 (1:3)	10,000	27.2	45.0

Table 5.1: Jet operating conditions of diluted ethylene flames. Re_{jet}; Jet Reynolds number, $\dot{Q}$; volumetric flowrate, $\bar{v}_{exit}$; mean exit velocity (for an exit temperature of 300K).

5.2 Flame Conditions

The jet in hot coflow (JHC) burner has been described in detail in §3.2.1. In brief, the JHC burner consists of a central fuel jet within an annular coflow of exhaust products from a secondary burner. The fuel used in the jet is ethylene (>99% C_2H_4), either undiluted, or diluted with hydrogen (H_2), air or nitrogen (N_2). Table 5.1 shows the compositions and volumetric ratios of the jet flow. Addition of H_2 at this mixing ratio (1:1) has often been used in hydrocarbon flames to reduce soot interference [50], and is consistent with previous measurements in this burner [31], as well as the other chapters in this thesis. Similarly, air dilution (at 1:3 fuel/air) also cleans flames from soot [77] whilst not significantly altering the flame structure [104]. Nitrogen added at the same ratio as air subsequently allows the effects of inert dilution to be considered independently.

Two coflow compositions (3% or 9% O_2, volumetric basis) are considered. The coflow properties are identical to those already presented in Table 4.2.

5.3 Visual Observations

Figure 5.1 shows photographs of the flames presented in this chapter. The two measurement locations, centred at 35mm and 125mm above the jet exit plane, are indicated. These measurement locations were chosen to represent two oxidant regimes. At the 35mm location, the oxidant stream is that of the coflow (with a specified O_2 level). At the 125mm location, air from the surrounds is entrained with the coflow stream, resulting in a different oxidant composition than at the
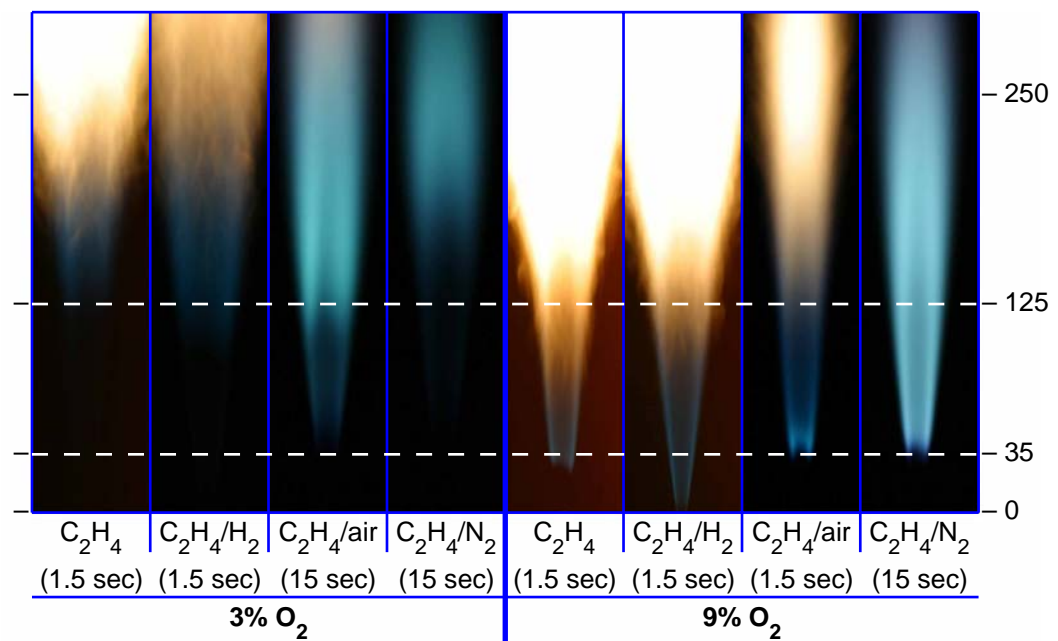
Figure 5.1: Photographs of diluted ethylene flames at two coflow O_2 levels. Jet Reynolds number of 10,000. Note the different exposure times (all other camera parameters held constant). Horizontal lines indicate measurement locations (35mm & 125mm downstream of jet exit plane). Photograph height: 300mm.

Coflow	C_2H_4	C_2H_4/H_2	C_2H_4/air	C_2H_4/N_2
3% O_2	Attached	Attached	Attached	Attached
9% O_2	26mm	Attached	33mm	34mm

Table 5.2: Apparent lift-off height estimates based on visual observations of diluted ethylene flames for Re_{jet}=10,000.

35mm location. It is clearly apparent that for all flames a reduction in O_2 level has led to a decrease in flame luminosity. This change in luminosity is attributed to the reduction in temperature and the different intermediates formed in each of the flames. Furthermore, it should be noted that due to the vast differences in the luminosity of the flames, the exposure times have been varied, while all other camera parameters held constant.

For either coflow O_2 level, where the coflow influences the jet flame ($\lesssim$100mm) soot is not apparent. Generally ethylene fuel has a tendency to produce large amounts of soot, especially with an elevated coflow temperature, but under the current low O_2 coflow conditions soot is not observed. It is only at the most downstream measurement location where the surrounding air begins to penetrate the coflow that soot appears. The presence of soot for some of the 9% O_2 flames (C_2H_4 and C_2H_4/H_2) at 125mm downstream could lead to interferences with the Rayleigh and LIF measurements, and so data collection at 125mm is limited to the 3% O_2 case only.

Except for the C_2H_4/H_2 flame, all of the 9% O_2 coflow flames visually appear lifted by $\sim$30mm. Based on the photographs, what appears to be the (mean) lift-off heights for the 9% O_2 flames are presented in Table 5.2. For all 3% O_2 flames a very faint outline may be seen to extend to the jet exit plane, although this is difficult to see in the photographs. The lack of luminosity under MILD combustion conditions almost gives the 3% O_2 flames the misleading appearance that they are lifted — they are attached however.

The photographs and data presented in Figure 5.1 and Table 5.2 are for a jet Reynolds number of 10,000 (based on jet inner diameter). By altering the jet velocity, the apparent lift-off heights have been determined at other jet Reynolds numbers as well, with the results shown in Figure 5.2. From this figure it is noted that increasing the jet velocity leads to a *reduction* in apparent lift-off height,
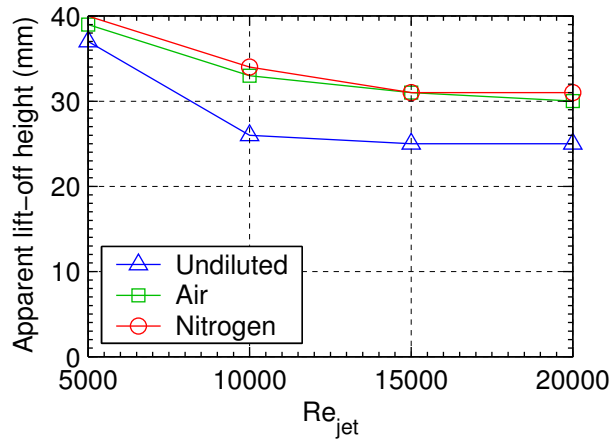
Figure 5.2: Apparent lift-off height of 9% O_2 diluted ethylene flames based on visual observations at various Reynolds numbers.

especially between jet Reynolds numbers of 5000 and 10,000, beyond which the effects are less pronounced. This trend is contradictory to the expected trends for lifted flames under conventional conditions. It is noteworthy that under the heated coflow conditions the Re_{jet}=5000 case borders a transition to turbulence conditions. Increasing the Reynolds number beyond 10,000 shows a much lower decrease in lift-off height.

5.4 Instantaneous Images – 35mm downstream

Figure 5.3 shows typical instantaneous image triplets of OH, H_2CO and temperature at the 35mm downstream location, for each of the fuel compositions at two coflow O_2 levels. The corresponding size of each image is 8×35mm, with the jet centreline indicated by the vertical dashed line. The data presented is for a jet Reynolds number of 10,000 for all cases. Data at different Reynolds numbers shows the same trends seen here.

The temperature images show a uniform temperature distribution in the coflow stream. From the OH images in Figure 5.3 it is clear that there exists vast differences in the relative OH number density for the various flames. The colour scaling for Figure 5.3 has been chosen to overemphasise the low OH levels, resulting in
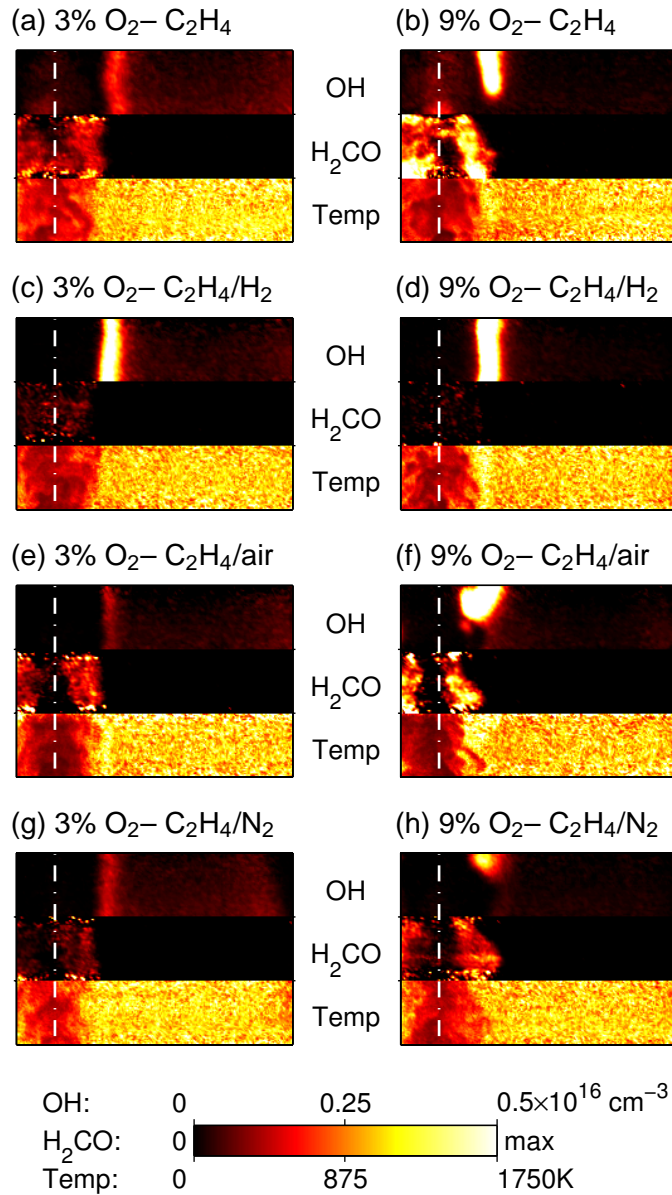
Figure 5.3: Selection of instantaneous OH, H_2CO and temperature image triplets showing typical features of diluted ethylene flames. Re_{jet}=10,000. Each image 8×35mm. Jet centreline marked with dashed line. Axial location 35mm above jet exit.

much of the OH to appear saturated. Very small quantities of OH can be seen in the coflow, and are equivalent to equilibrium levels. As stated in Chapter 4, the spatial location of H_2CO on the fuel-rich side, in relation to OH, reinforces that H_2CO is a first-step intermediate [14] formed as a product of fuel decomposition [65]. The H_2CO levels differ from one fuel composition to another, and are also influenced by the O_2 level in the coflow.

As already highlighted, all of the 3% O_2 coflow flames were visually identified as being attached. This is confirmed in the OH images of Figure 5.3 where a continuous OH layer is seen in each of the 3% O_2 images. The images show a substantial suppression of OH levels in the low O_2 coflow, consistent with the results in Chapter 4 and previous work (e.g. [94]). For most of the 3% O_2 flames the temperature peak across the reaction zone is barely discernable, although a definite OH layer is measured. Similar observations regarding the very low, almost indistinguishable, temperature rise across the reaction zone has been seen in a similar high temperature oxidant stream environment [47] and also in a MILD combustion furnace [88]. It is noted that a temperature increase is seen in the air diluted flame in relation to the other fuel compositions for a 3% O_2 coflow. The temperature increase with air dilution is supported by laminar flame calculations (used to determine the quenching rate) which predict a temperature increase of $\sim$150K relative to the undiluted jet.

At the 9% O_2 coflow, the OH images reveal significant differences to the 3% case, most notably the observation that these flames initially appear lifted. The identified lift-off heights from visual observations are at around the same downstream location as the measurement location ($\sim$35mm). Fluctuations in the apparent lift-off height results in some of the 9% O_2 instantaneous images including strong OH whilst others do not. Figures 5.3b, 5.3f & 5.3h typify the characteristics seen at the base of lifted flames. Closer inspection of the 9% images reveals some interesting observations. Except for the H_2 diluted flame (which is attached), the 9% images presented in Figure 5.3 have been chosen to show what seems to be the bottom of a lifted flame. Beneath the strong OH, in each of the lifted images a weak tail is seen towards the bottom.

Figure 5.4 presents a further selection of images from the flames that appear lifted. The lack of strong OH in these images indicates that these instances are
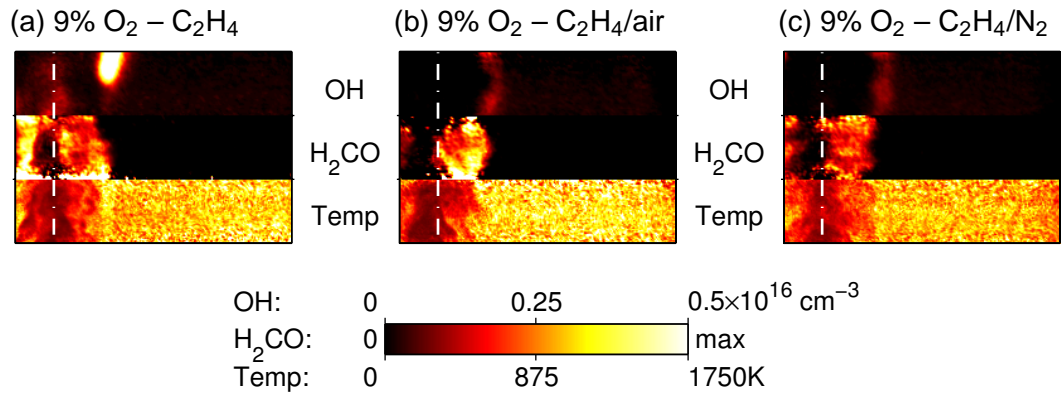
Figure 5.4: Selection of instantaneous OH, H_2CO and temperature image triplets showing examples of lifted diluted ethylene flames. Re_{jet}=10,000. Each image 8×35mm. Jet centreline marked with dashed line. Axial location 35mm above jet exit.

below an instantaneous apparent lift-off height, nevertheless, a discernable OH surface is seen. As the apparent lift-off height of the undiluted flame is less than the other flames, at the measurement location no images were identified where there was no strong OH in the image. The lower parts of image Figure 5.4a show the same features as the other flames in Figure 5.4 however.

The presence of H_2CO in conjunction with the OH in the images tends to suggest that there is in fact a pre-ignition reaction taking place below what appears to be the lift-off height. Formation of H_2CO early in the ignition process has been noted previously in similar conditions [46]. Coupled with the OH observations, formation of H_2CO casts significant doubt over the visual observation of these flames being lifted. The apparent lift-off height corresponds to a transition of weak to strong OH levels. As such, rather than identifying a "lift-off" height it is more appropriate to refer to this as a transition point. The general observations relating to this transition point seem to be analogous to conventional lifted flames.

It is interesting to note that the H_2CO levels are similar at each axial location whether there is strong OH or not. Modelling efforts of Gkagkas & Lindstedt [46] suggest that the H_2CO concentrations reach a maximum just before the flame front – such an increase is not seen in the images presented here. Moreover, the H_2CO distribution shows a relief along the jet centreline and exists on the fuel-

Coflow	C_2H_4	C_2H_4/H_2	$C_2H_4/$Air	C_2H_4/N_2
3% O_2	0.14 [27%]	0.64 [10%]	0.17 [41%]	0.15 [30%]
9% O_2	0.95 [31%]	1.77 [29%]	0.39 [139%]	0.12 [94%]

Table 5.3: Mean and standard deviation (σ, in brackets) of peak OH number density ($\times 10^{16}$ cm^{-3}) for diluted ethylene flames. Re_{jet}=10,000. Axial location 35mm above jet exit.

rich side, whereas Gkagkas & Lindstedt [46] present a continuation of the H_2CO to the centreline. It should be noted that the flames of Gkagkas & Lindstedt [46] are lifted, whereas the flames presented here are not believed to be strictly lifted. For each of the fuel compositions, the H_2CO levels in the 3% O_2 coflow are less than for the 9% O_2 case. The H_2 diluted flame has significantly lower H_2CO levels than the other flames, leading to the very weak H_2CO-LIF signal.

5.5   Radial Profiles – 35mm downstream

Table 5.3 shows the averaged peak OH values in each of the images for a particular flame, also included is the standard deviation (as a percentage). In determining the peak value in each of the images, only the central 3mm strip of the image is included to avoid over-corrected values towards the edges of the images where the low laser power makes sheet corrections less reliable.

As expected, the OH number density at the 3% O_2 coflow is lower than the 9% O_2 case. For the 3% O_2 coflow, the mean peak OH number density seems quite independent of the fuel composition, although a $\sim$3 fold increase is found in the C_2H_4/H_2 flame. The increase of OH in this flame, which is consistent with laminar flame calculations, is not a product of increased temperature but is attributed to the presence of H_2.

At the 9% O_2 level the apparent lifted nature of these flames limits making comparisons between these flames and are only included to highlight this very issue. As already highlighted, and seen in the images of Figures 5.3 & 5.4, at the 35mm measurement location the base of strong OH is intermittently captured in the images. This intermittency leads to the very high standard deviation for

Coflow	C_2H_4	C_2H_4/H_2	C_2H_4/Air	C_2H_4/N_2
3% O_2	33 [23%]	14 [28%]	47 [29%]	21 [24%]
9% O_2	86 [31%]	9 [42%]	56 [35%]	35 [23%]

Table 5.4: Mean and standard deviation (σ, in brackets) of peak H_2CO concentration (arbitrary units), for diluted ethylene flames. Re_{jet}=10,000. Axial location 35mm above jet exit.

the air and nitrogen diluted flames. The undiluted flame also appears lifted, but slightly less than the other two, such that the base of strong OH is always captured, as indicated by the much lower standard deviation and the higher mean OH number density.

The averaged H_2CO peak values (and standard deviation) from the instantaneous images is presented in Table 5.4. As with the OH peak values, only the central portion of the images is included. As expected due to oxygenation of the fuel with air dilution [78] the 3% O_2 flames have the highest H_2CO levels, and is consistent with the instantaneous images of Figure 5.3. At the 9% O_2 coflow the undiluted flame mean H_2CO levels are higher than the air diluted flame. This difference is likely to be due to the apparent lift-off and the pre-ignition chemistry of the different fuels. The intermittency of the lift-off height observed in the OH number density standard deviations is not reflected in the H_2CO standard deviation for the lifted 9% flames. The consistency in the H_2CO levels was also noted in the instantaneous images of Figure 5.3.

Figure 5.5 shows the mean and RMS radial profiles of OH, H_2CO and temperature for both 3% and 9% O_2 for the various fuel compositions, and at an axial location 35mm above the jet exit plane. As most of the 9% O_2 flames appear lifted, direct comparison between the two O_2 levels is less meaningful. For the H_2 diluted flame however, it is clear from Figure 5.5 that reducing the O_2 levels leads to a substantial decrease of OH, as already seen in the instantaneous images. It is also noted that minor equilibrium OH levels in the coflow stream are observed at both coflow conditions.

At 3% O_2, except for the hydrogen diluted flame, the mean OH profiles virtually overlap. The much higher levels of OH for the H_2 diluted flame was also reflected in Table 5.3. The trends seen in the 9% O_2 flames are in agreement with the
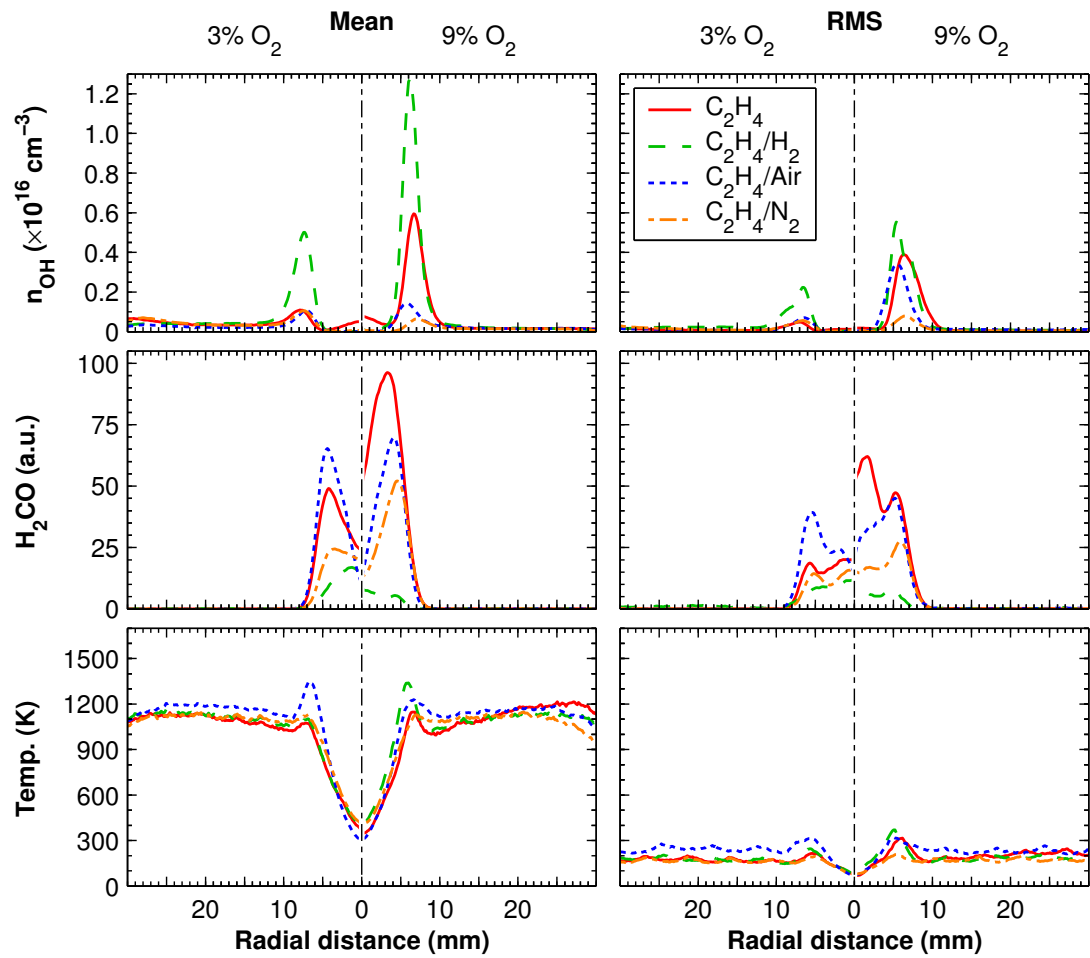
Figure 5.5: Mean and RMS radial profiles of OH, H_2CO and temperature for diluted ethylene flames. Re_{jet}=10,000. Central 3mm strip of images used. Axial location 35mm above jet exit.

values in Table 5.3. In the undiluted ethylene flames a very slight increase in OH-LIF signal is seen towards the jet centreline. As outlined in §3.9.2, this effect is attributed to Raman interferences from the C_2H_4, and does not influence any of the current findings as it is readily disregarded based on the spatial location relative to the reaction zone. From both the mean plots and the instantaneous images in Figure 5.3 the extraneous OH-LIF signal along the centreline is seen to drop to zero before it increases through the reaction zone. This is further evidence of the interference being due to C_2H_4. Due to dilution of C_2H_4 for the other fuel composition this interference is not seen.

As has already been mentioned, the detection of H_2CO along the centreline in the radial plots is related to the very broad distribution of H_2CO in mixture fraction space. This effect will be discussed in further detail in §6.6.

5.6 Results – 125mm downstream

At the 125mm downstream location it is visibly evident that the flames are perceptibly different in structure, as seen in Figure 5.1. At this location the surrounding air is able to mix with the hot coflow. As seen in the photographs, soot becomes apparent at this location for the 9% O_2 coflow flames, limiting laser diagnostic measurements of these scalars to the 3% case only. The presence of soot particulate could potentially interfere with the measurements.

Figure 5.6 shows the mean and RMS radial profiles of OH, H_2CO and temperature for a 3% O_2 coflow for the various fuel compositions, and at an axial location 125mm above the jet exit plane. In comparison to the equivalent plot at 35mm downstream (Figure 5.5) it is apparent that the radial distribution becomes broader and peaks at a wider radial location, due to the spreading of the jet.

Figure 5.7 shows typical images for the various 3% O_2 flames at the 125mm axial location. At the furthest downstream location, the entrainment of additional oxygen from the surrounds into the coflow results in increased reaction rates. This in turn leads to increases in the OH and temperature at the 125mm downstream location compared to the 35mm position. Of particular note in these images
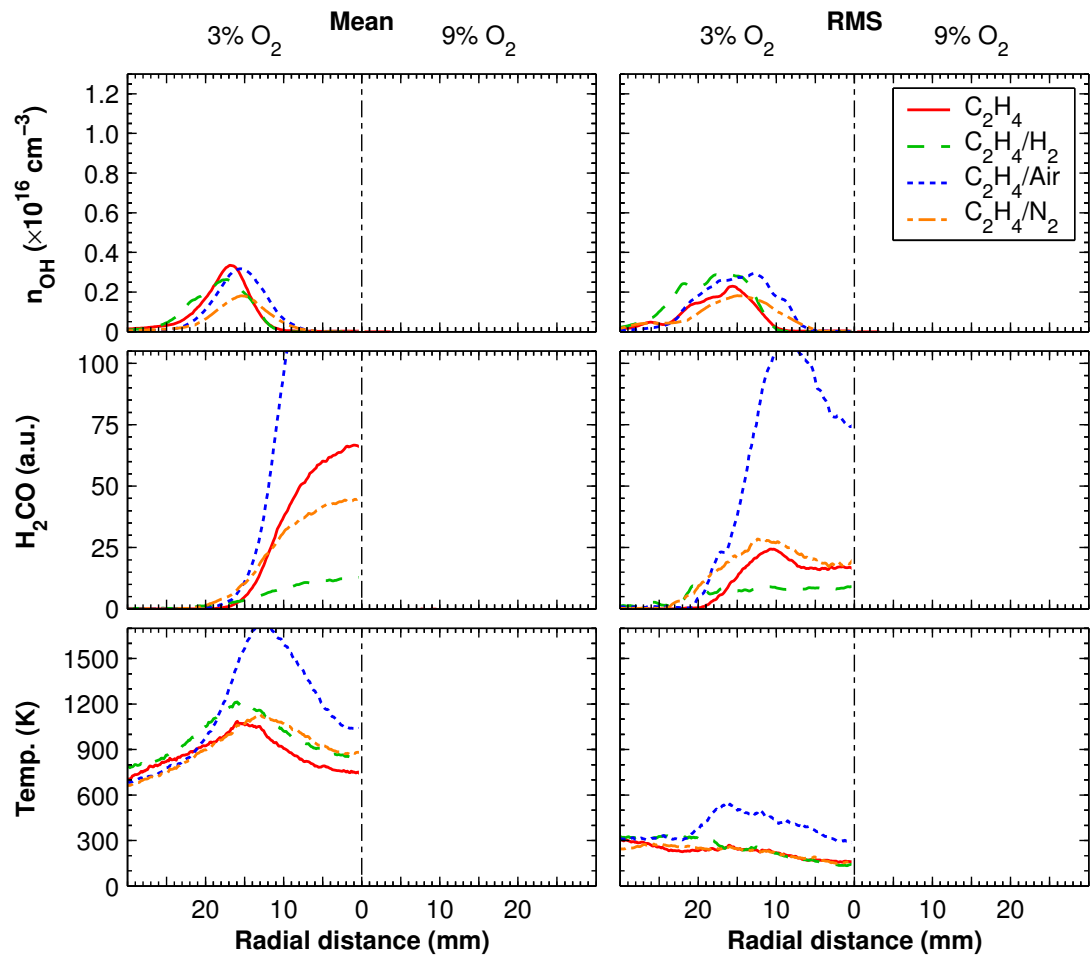
Figure 5.6: Mean and RMS radial profiles of OH, H_2CO and temperature for diluted ethylene flames. Re_{jet}=10,000. Central 3mm strip of images used. Axial location 125mm above jet exit.
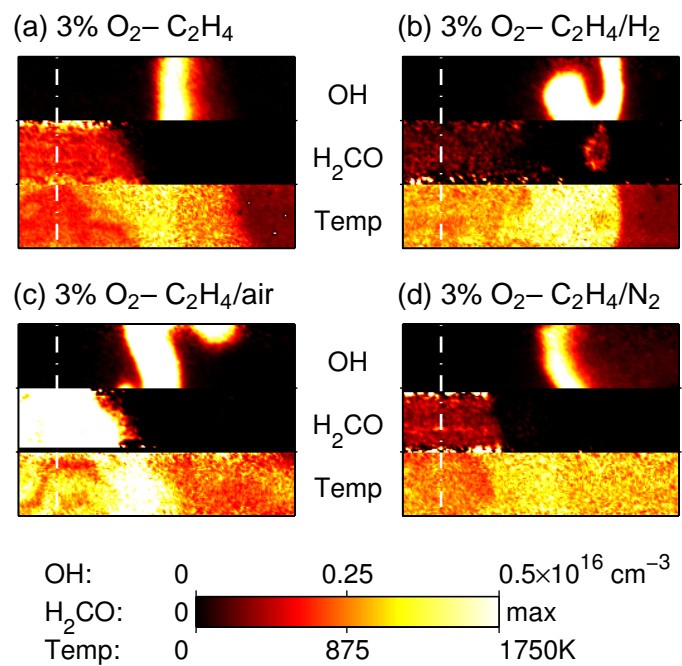
Figure 5.7: Selection of instantaneous OH, H_2CO and temperature image triplets showing typical features of diluted ethylene flames. Re_{jet}=10,000. Each image 8×35mm. Jet centreline marked with dashed line. Axial location 125mm above jet exit.

Coflow	C_2H_4	C_2H_4/H_2	C_2H_4/Air	C_2H_4/N_2
3% O_2	0.53 [16%]	0.65 [29%]	0.62 [26%]	0.36 [49%]

Table 5.5: Mean and standard deviation (σ, in brackets) of peak OH number density ($\times 10^{16}$ cm^{-3}) for diluted ethylene flames. Re_{jet}=10,000. Axial location 125mm above jet exit.

Coflow	C_2H_4	C_2H_4/H_2	C_2H_4/Air	C_2H_4/N_2
3% O_2	39 [25%]	12 [44%]	162 [25%]	39 [34%]

Table 5.6: Mean and standard deviation (σ, in brackets) of peak H_2CO concentration (arbitrary units), for diluted ethylene flames. Re_{jet}=10,000. Axial location 125mm above jet exit.

is the mismatch between the OH and H_2CO surfaces. Although the OH and H_2CO demarcate the fuel lean and rich sides of the reaction zone, respectively, the spatial separation between the two is extraordinarily large. For example, in the nitrogen diluted image presented in Figure 5.7d the separation is ∼5mm. This separation is not due to experimental error in the matching of the images, since correlation of a target image before and after the runs does not exhibit any spatial mismatch. Furthermore, a temperature increase is noted to follow the respective borders of the void between the OH and the H_2CO. The separation is likely to be due to the consumption of the H_2CO well in advance of the reaction zone due to the high temperature in this region, as has been noted previously [46].

Tables 5.5 & 5.6 respectively present the averaged peak and standard deviation (as a percentage) of the OH and H_2CO values for each flame. As was also seen in Table 5.3, at the 125mm downstream location the OH number density is relatively constant for the different fuel compositions. A slight reduction in peak OH is noted for the N_2 diluted flame – which also has the highest standard deviation in the peak OH value. For the H_2CO, from Table 5.5 the air diluted flame is seen to have a peak value four times higher than the other fuel compositions, as expected, and consistent with the 35mm data.

5.7 Discussion

5.7.1 General Observations

A triple flame consists of lean and rich premixed flames surrounding a diffusion flame. Joedicke et al. [57] have presented images of lifted methane and methane/nitrogen flames suggesting evidence of a triple flame structure. Their flames consisted of a simple fuel jet issuing into a nominal coflow. The heated coflow used in the current work seems to provide a fundamentally different environment to that of Joedicke et al. [57]. Comparison of images already presented to that of Joedicke et al. [57] reveals significant differences in the distribution of OH and H_2CO. The differences are particularly evident in the H_2CO images. Without a heated coflow, the H_2CO only appears around the base of the lifted flame [57], whereas with a heated coflow the H_2CO is seen to exist well below the lift-off height (Figure 5.4).

Imaging of OH alone is insufficient to identify a triple flame structure [95], but coupled with H_2CO it may be possible to infer a triple flame. In a triple flame the H_2CO should "wrap around" the OH, thereby creating two H_2CO peaks, each demarcating the fuel lean and rich branches. In general, the images presented do not show evidence of a triple flame structure existing in the flames. A few images show some signs of two H_2CO branches (Figure 5.8), but no H_2CO is present at what would be deemed the triple point. The cause of the H_2CO distribution seems far more likely to be due to vortical structures rather than a triple flame.

While there is no evidence of triple flames, and a significantly different H_2CO distribution, this alone cannot categorically confirm or deny the existence of a triple flame. The turbulent nature of the flames may lead to a compression of the triple flame such that its presence would be masked [72]. As reported by Joedicke et al. [57], and noted by Im & Chen [54], as turbulence levels increase the interaction of vortices with a triple flame cause the branches of a triple flame to collapse into an edge flame.
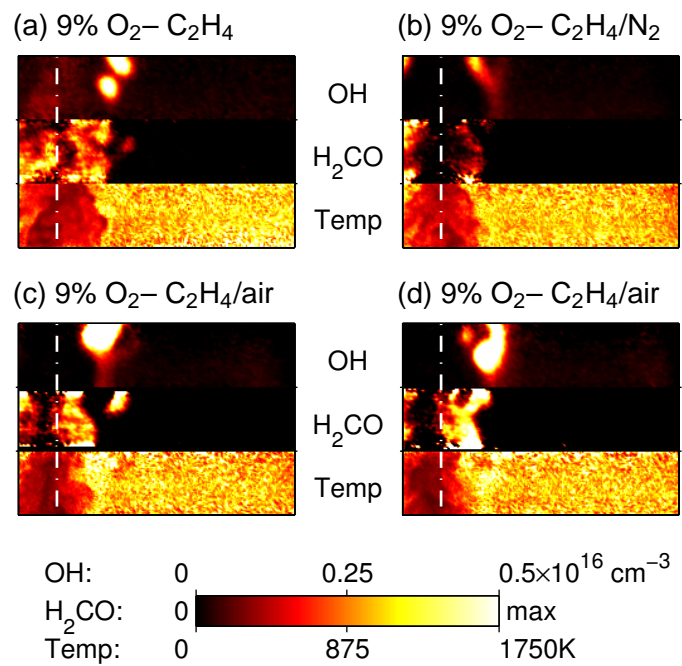
(a) 9% O_2– C_2H_4

(b) 9% O_2– C_2H_4/N_2

OH

H_2CO

Temp

(c) 9% O_2– C_2H_4/air

(d) 9% O_2– C_2H_4/air

OH

H_2CO

Temp

OH: 0   0.25 0.5×10^{16} cm^{-3}

H_2CO: 0   max

Temp: 0   875   1750K

Figure 5.8: Axial location 35mm above jet exit – further selection of instantaneous OH, H_2CO and temperature image triplets for diluted ethylene flames. Re_{jet}=10,000. Each image 8×35mm. Jet centreline marked with dashed line.

5.7.2 Effect of Coflow O_2 Level

The most noticeable difference between the two coflow oxygen levels is noted in the apparent lift-off phenomenon observed. At the higher (9%) O_2 level, the flames visually appear lifted, but the OH tends to indicate a continuous reaction extending to the jet exit. Furthermore, lift-off height is generally considered to be directly proportional to the jet exit velocity [72], whereas increasing the jet velocity (jet Reynolds number) for these flames is seen to decrease the lift-off height (Figure 5.2). In this study the lift-off height is based on visual observation and long-exposure photography rather than an arbitrary choice of chemilumines-cence, as has been used in other previous work (e.g. [48]) or a defined OH mass fraction (e.g. [21, 22]). The different approach is not expected to lead to the variations noted however. Moreover, during the experiments as the jet flowrate was increased the apparent lift-off height was visually seen to decrease. It is worth mentioning that hysteresis effects which occur in flames without a hot coflow [72] are not expected to lead to the differences in the apparent lift-off heights seen here because of the hot coflow. The coflow temperature is above auto-ignition and so this is believed to counteract any hysteresis effects.

The presence of OH and H_2CO below the identified lift-off (transition from weak to strong OH) height coupled with the different trend of apparent lift-off height with jet velocity all points towards these flames not being lifted at all. As the flames are not strictly considered to be lifted, then there is no reason to suggest that they should follow the general trends of lifted flames.

The different trend in transition height with jet velocity is likely due to an increase in mixing near the jet exit. A similar observation has been previously noted in a MILD combustion furnace. Dally et al. [32] reported that an increase in jet velocity helped to stabilise their flames closer to the jet exit. This trend highlights the differences in the stabilisation mechanisms of these flames as compared with conventional lifted flames.

The role of mixing on the stabilisation is highlighted when it is considered that transition height is very similar for the different diluted flames. The undiluted case has a jet velocity less than half of the other two transitional flames. However, the Reynolds number is constant. The similar turbulence levels, which control

Fuel Composition	Volumetric ratio	f_{stoich} 3% O_2	f_{stoich} 9% O_2
C_2H_4	—	0.010	0.029
C_2H_4/H_2	1:1	0.009	0.027
C_2H_4/Air	1:3	0.050	0.135
C_2H_4/N_2	1:3	0.039	0.108

Table 5.7: Fuel jet dilution ratios of ethylene (C_2H_4) and stoichiometric mixture fraction (for both coflow compositions).

the mixing, are believed to play a role in the similarity of the transition height.

The observation of the transition from weak to strong OH in the higher O_2 flames is analogous to a lifted flame. Such a transition is not seen in the lower O_2 flames however. The transition which occurs at the 9% O_2 level and not at 3% O_2 could be due to a shift in the stoichiometric mixture fraction (Table 5.7) towards the fuel rich side, where the interactions with the jet shear layer are higher. Another alternative may be that the *flame induced* strain rates are reduced because of the lower reaction rate and subsequent heat release rate.

The presence of H_2CO in conjunction with the identified OH surface in the images of apparent lifted flames tends to suggest that there is in fact a reaction taking place below the transition height. Furthermore it is noted that the OH number density below the transition point in the 9% O_2 flames is at similar levels to the attached 3% O_2 flames. For the 3% flames, the luminosity of the entire flame is very low, enabling visual identification of the very faint outline of the reaction zone down to the jet exit plane. The more luminous flame brush of the 9% flames may mask such a reaction zone outline in the 9% flames. If it were possible to isolate the light from luminous brush perhaps a reaction zone outline may be able to be identified in the lower parts of the 9% flames as well.

In contrast to the present work, under similar vitiated conditions Gordon et al. [48] observed a linear dependence of lift-off height with jet velocity. Four significant differences are noted between the current work and that of Gordon et al. [48]; (1) different O_2 level in coflow, (2) different fuel and coflow composition, (3) different jet velocities and (4) different coflow velocity. It is important to recognise the extreme sensitivity of the lift-off height with coflow temperature

[22] and also the coflow velocity [95]. The clear trend of lift-off height with jet velocity for the various fuel diluents suggests that the sensitivity of the lift-off height is not likely to be responsible for the trends seen in the current data. It is relevant to note that Gordon et al. [48] used the same burner design as Cabra et al. [20, 21]. In the work of Cabra et al. the OH mass fraction results show a lifted flame, but the PDF reaction progress shows a reaction taking place well upstream of the main OH contours. Furthermore, a *very* faint OH outline is seen in Figure 3 of Cabra et al. [21]. The barely discernable OH tail seems to be consistent with the current results. The relative intensity of the weak OH in the tail and the much stronger OH downstream of the "lift-off" height is far more pronounced in Cabra et al.'s work as compared with the current data. This is expected to be due largely to the differences in the O_2 levels and potentially the coflow temperature as well. It is also noted that the fuel in the Cabra et al. [21] study is H_2/N_2. Subsequent work by Cabra et al. [20] has shown that the stabilisation of CH_4/air flames is different to the H_2/N_2 case.

The reason for the presence of the weak OH upstream of the transition point seen in the images does not seem to be due to the reverse flow observations made by Upatnieks et al. [112] or the existence of products further upstream by Tacke et al. [108]. The high temperatures of the coflow stream suggest that the characteristic S-shaped curve for ignition and extinction collapses into a monotonic function [94]. Consequently separate ignition and extinction events do not occur [88]. This seems to be a relevant observation regarding the detection of OH in what appears a non-reacting region. It is particularly important that despite the proposition of a monotonic function for extinction/ignition, a bimodality under MILD combustion conditions has been observed [32]. It is mooted that under MILD conditions perhaps the extinction/ignition phenomenon manifests itself as a weak/strong reaction. This transition leads to a bimodal behaviour, without explicit extinction/ignition occurring.

The intimation that there may be a reaction taking place upstream of the lift-off height *does not* categorically conflict with the potential of a lifted flame. The reaction which is in discussion is not considered to be a fully fledged flame, rather some kind of pre-ignition reaction. Being a much less intense reaction, entrained mixing with the oxidant stream is capable of permeating through the "reaction"

zone, leading to premixing at the lift-off height, thus resulting in the stronger OH levels after a certain downstream distance.

The role of the pre-ignition reaction taking place upstream of the transition height does not seem to significantly alter the remainder of the flame. Cabra et al. [21] showed that under similar heated and diluted coflow conditions, conventional scaling arguments seemed to predict the lift-off height, suggesting that the overall characteristics of the flame were not significantly varied from a standard flame. As Cabra et al. [21] noted, the different temperature of the coflow may alter the mechanisms relating to lift-off despite the similar global observations between the vitiated and conventional conditions. This is in relative agreement with the present findings. It is acknowledged that a reaction upstream of the transition height does not significantly effect the downstream reactions, but does tend to suggest a different kinetic role in the stabilisation mechanism.

5.7.3 Effects of Fuel Composition

It is clear from the flame photographs of Figure 5.1 that changing the fuel composition alters the visual appearance of the flames. Differences between the flames are not as obvious in the OH concentrations seen in Table 5.3 and Figure 5.5, however, more significant differences are seen in the H_2CO concentration profiles of Figure 5.5.

When comparing the effect of fuel dilution, focus is placed on the 3% O_2 flames because these are all attached. The highest H_2CO levels are expected in the air diluted (partially premixed) flame over the nonpremixed flames [78]. Partial premixing leads to at least five times H_2CO levels as in nonpremixed methane flames [78]. The effect of premixing is even more pronounced for ethylene, where small amounts of premixing (Φ=24) are reported to lead to a eight-fold increase in formaldehyde over the nonpremixed flame [77]. The equivalence ratio of the air diluted flame in the current study is $\Phi \approx 4.8$, which is expected to have maximum H_2CO levels $\sim$15 times larger than the undiluted flame [77], much greater than the increases seen in Figure 5.5. It is imperative to highlight that the peak H_2CO concentrations of McEnally & Pfefferle [77] are based on centreline data, at a much further downstream location and at laminar conditions. It has pre-

viously been shown in Chapter 4 that Reynolds number has a significant effect on H_2CO concentrations. Nevertheless, the trends of H_2CO increase are consistent. Furthermore, even in an un-questionably attached flame under conventional conditions some O_2 penetrates to the jet centreline, resulting in some form of pre-mixing even in attached flames [78]. The effect of oxygen permeating through the flame front zone is expected to be more pronounced as a result of the weakened reaction zone at the low O_2 coflow conditions in these flames, enhanced by the thermal diffusion due to the hot coflow.

The potential for oxygen leakage through the reaction zone in the low O_2 flames may lead to higher H_2CO levels in the undiluted flames as compared to an ideal nonpremixed flame, and so the effects of partial premixing may be reduced.

The dilution rate for the partially premixed (air diluted) and inert (nitrogen) diluted flames is the same. Any differences between the two are directly attributed to the effects of the additional oxygen, with only a slight change in stoichiometric mixture fraction. The OH concentrations and the general features of the images remain essentially constant for either diluent. Increases in the peak H_2CO and temperature are noted with air dilution, while retaining the same features. Partial premixing of the flame therefore seems to increase reaction rates, but not significantly alter the inherent structure of the reaction zone. It is generally accepted that at this level of premixing the flame retains all the nonpremixed flame features, which seems to hold true in heated and diluted conditions as well.

Hydrogen dilution leads to the most noticeable variations in the measured species. Concentrations of OH increase markedly, while H_2CO levels drop dramatically. Addition of H_2 also gives rise to the 9% O_2 flames attaching, unlike any of the other cases. The addition of H_2 to the fuel is expected to lead to an attached flame as it is known that H_2 acts as an ignition promoter [46].

Small degrees of partial premixing increases soot volume fractions in ethylene flames, but for equivalence ratios below about ~15 soot volume fractions subsequently decrease [77]. The equivalence ratio of the partially premixed flame is $\Phi \approx 4.8$, and so the premixing is expected to reduce levels of soot, as seen in Figure 5.1.

Increasing the stoichiometric mixture fraction (by means of fuel dilution) causes

the location of the reaction zone to shift towards the shear layer, having an influence on the flame structure [59]. Moreover, shifting the stoichiometric mixture fraction closer to the fuel side can be linked to a decrease in soot formation [40]. The stoichiometric mixture fraction of the 9% flames is greater than the 3% flames, suggesting that if the stoichiometry shift was the only difference between the two O_2 cases the 9% flames would exhibit less soot – which does not appear to be the case. This suggests that the soot suppression by means of reducing the O_2 level is related to the chemical effects of the hot coflow and not the shift in stoichiometry.

The effects of the hot and diluted coflow on the levels of soot seem to extend beyond the region where the oxidant composition is controlled by the coflow. As a generalisation, soot does not appear until $\sim$200mm downstream of the jet exit. The coflow is known to persist only approximately 100mm downstream, and so, it seems that the initial conditions have a significant role on the intermediates that are formed, which in turn alter the downstream behaviour of the flames.

Chapter 6

Influence of Fuel Type

6.1   Introduction

In this chapter the influence of combustion chemistry on the flame behaviour and reaction zone structure is examined by systematically increasing the fuel complexity under MILD combustion conditions. Three different fuels are considered, namely; natural gas, ethylene, and LPG (each diluted with hydrogen). The difference in the chemical path for these fuel mixtures provides a way of assessing the sensitivity of the MILD combustion regime to fuel type (for gaseous hydrocarbon fuels). By maintaining all other conditions constant except for the fuel type, any differences between the flame structure can be attributed to the chemical kinetics of the fuel.

To emulate MILD combustion, the jet in hot coflow (JHC) burner (§3.2.1) is used. Two coflow compositions are considered, either with 3% or 9% O_2 (volumetric). For each fuel type in the jet, differences in the fluid properties necessitates a change in the velocity to hold the Reynolds number constant (at Re_{jet}=10,000) in order to maintain similar turbulence levels. The primary fuel is diluted with hydrogen (H_2) in an equal volumetric ratio to reduce the levels of soot and to improve flame stability. Addition of H_2 also has implications for the potential use of hydrogen as a supplemental fuel additive.

In the following sections, flame appearance and characteristics are discussed. Si-

Fuel (mol/mol)	Re_{jet}	$\dot{Q}$ [L_n/min]	$\bar{v}_{exit}$ [m/s]
NG/H_2 (1:1)	10,000	48.0	52.9
C_2H_4/H_2 (1:1)	10,000	30.5	33.6
LPG/H_2 (1:1)	10,000	17.5	19.3

Table 6.1: Jet operating conditions of natural gas (NG), ethylene (C_2H_4) and LPG flames, each diluted with hydrogen in equal volumetric parts. Re_{jet}; Jet Reynolds number, $\dot{Q}$; volumetric flowrate, $\bar{v}_{exit}$; mean exit velocity (for an exit temperature of 300K).

multaneous measurements of the hydroxyl radical (OH), formaldehyde (H_2CO) and temperature are presented for two downstream locations. The chapter concludes with a general discussion of the findings.

6.2 Flame Conditions

The jet in hot coflow (JHC) burner has been described in detail in §3.2.1. In brief, the JHC burner consists of a central fuel jet within an annular coflow of exhaust products from a secondary burner. Both the jet and coflow conditions are controlled separately. The coflow properties are identical to those already presented in §4.2. Tables 6.1 and 4.2 list the flowrates and operating conditions of the jet and coflow, respectively, for the flame conditions presented in this chapter. Measurements for each of the fuel types listed in Table 6.1 are taken at both of the coflow O_2 levels described in Table 4.2.

6.3 Visual Observations

Figure 6.1 shows photographs of the flames presented in this chapter. Apparent from Figure 6.1 is that the natural gas flames show significantly less soot than the ethylene and LPG flames. While soot is seen at both coflow O_2 levels for the ethylene and LPG flames, at the 3% O_2 level soot does not appear until around ~200mm downstream, whereas for the 9% O_2 case soot appears much closer to the jet exit (~100mm). For either fuel type, at the higher (9%) O_2 level, close to the jet exit the flame luminosity is significantly greater as compared to the lower
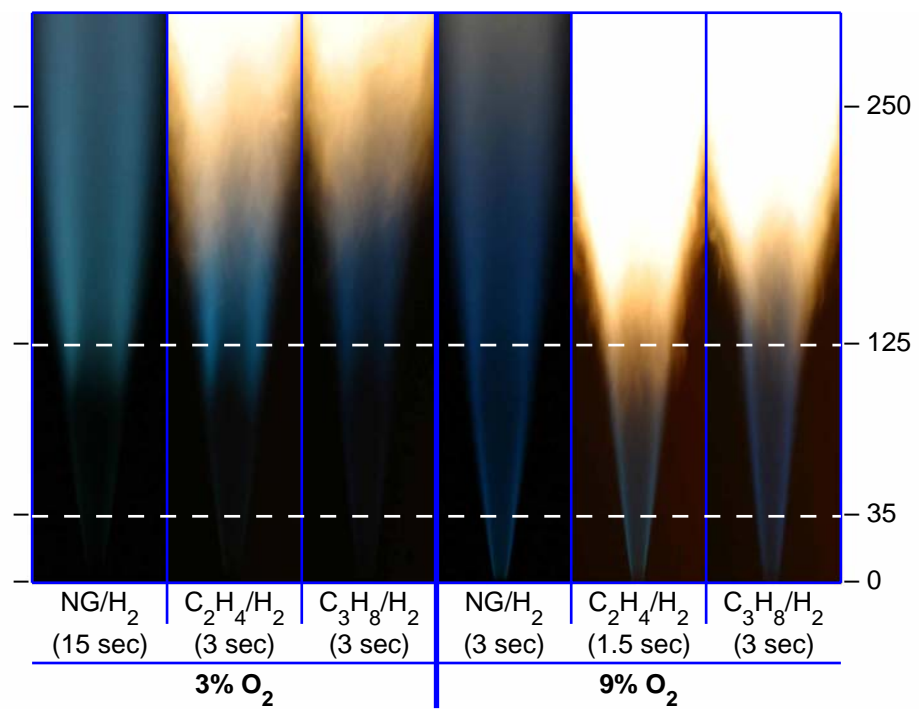
Figure 6.1: Photographs of natural gas (NG), ethylene (C_2H_4) & LPG flames, each diluted with hydrogen (1:1 vol/vol) at two coflow O_2 levels. Jet Reynolds number of 10,000. Note the different exposure times (all other camera parameters held constant). Horizontal lines indicate measurement locations (35mm & 125mm downstream of jet exit plane). Photograph height: 300mm.

(3%) O_2 case. The low luminosity of the 3% O_2 flames almost makes them appear invisible for the first $\sim$100mm. While not clearly apparent from the photographs, a faint reaction is indeed apparent in this region. Further downstream, once the effects of the coflow are diminished by the entrainment of surrounding air, soot does begin to appear for either coflow O_2 level. The presence of soot around the 125mm downstream location in the 9% O_2 flames could potentially interfere with laser diagnostic measurements, and so data is collected at this location for the 3% O_2 flames only.

6.4 Results – 35mm downstream

6.4.1 Typical Features

Figure 6.2 presents typical image triplets of OH, H_2CO and temperature for each flame condition (three fuel types, each at two coflow O_2 levels) at the 35mm downstream location. Consistent with the representative images already presented in Chapters 4 & 5 (i.e. Figures 4.2 & 5.3) the majority of the LPG/H_2 images also show no sign of large-scale turbulent structure.

It is seen in Figure 6.2 that in all cases the OH appears as an unconvoluted layer which is quite uniform in intensity along the length of the sheet. For each fuel type, the OH concentration is considerably less at 3% O_2 as compared to the 9% O_2 case. At either O_2 level the OH concentration does not significantly vary with the type of fuel.

The temperature in the coflow is again seen to be uniform. For all of the 3% O_2 cases there is no obvious sign of a temperature increase across the reaction zone, although a reaction is clearly taking place as identified by the presence of OH. The very low temperature rise at the low O_2 level has been discussed previously in §4.4. With the 9% O_2 coflow the temperature is seen to increase in the region corresponding to OH, as is expected.

The H_2CO concentration varies with both the O_2 level and even more dramatically with the type of fuel. Most notably, the 3% O_2 C_2H_4/H_2 flame has significantly higher H_2CO than any other flame. In all cases the H_2CO appears quite
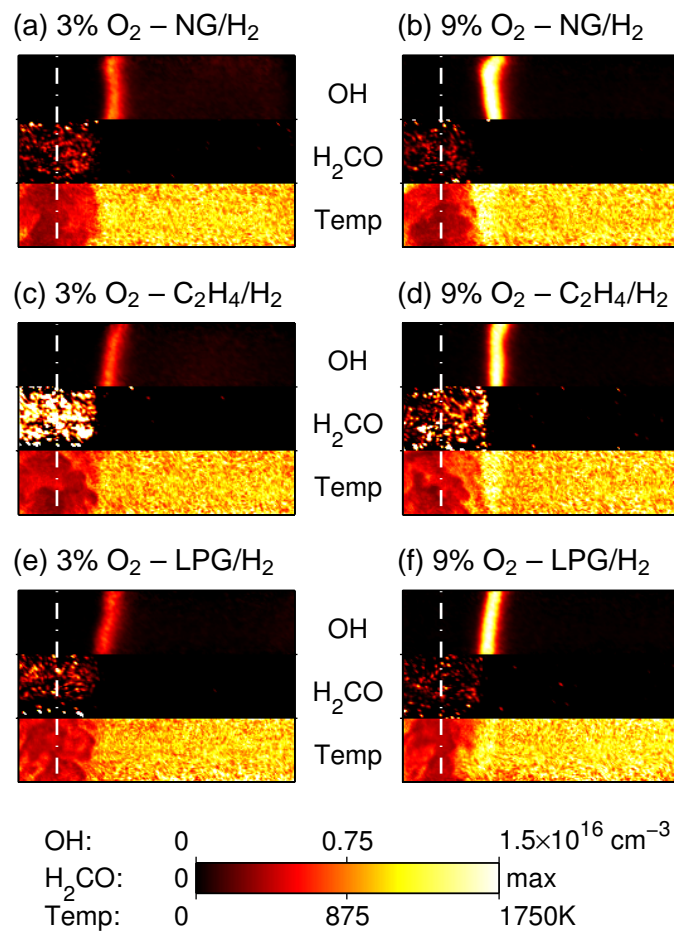
Figure 6.2: Selection of instantaneous OH, H_2CO and temperature image triplets of natural gas/H_2, C_2H_4/H_2 and LPG/H_2 flames showing typical features. Re_{jet}=10,000. Each image 8×35mm. Jet centreline marked with dashed line. Axial location 35mm above jet exit.
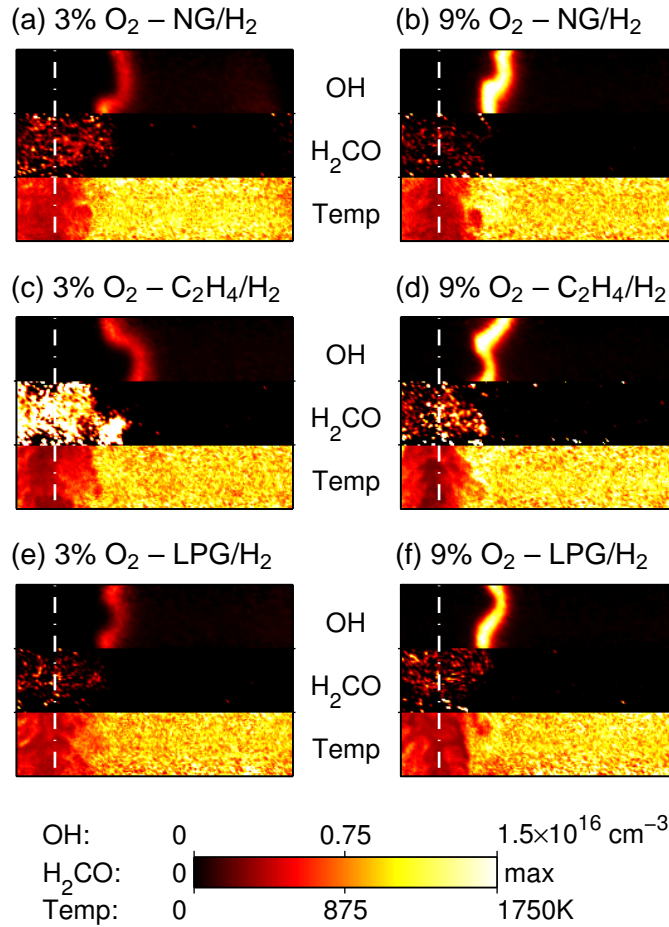
Figure 6.3: Selection of instantaneous OH, H_2CO and temperature image triplets of natural gas/H_2, C_2H_4/H_2 and LPG/H_2 flames showing vortex interaction with the reaction zone (reaction zone convolution). Re_{jet}=10,000. Each image 8×35mm. Jet centreline marked with dashed line. Axial location 35mm above jet exit.

uniformly distributed and always exists on the fuel-rich side of the OH layer.

6.4.2 Turbulent Fluidic Structure

The images presented in Figure 6.2, and indeed all measurements in this chapter, are for a jet Reynolds number of 10,000. The features noted are essentially the same as those seen at other Reynolds numbers. With a change in Reynolds number, the only major difference is the change in proportion of images which show signs of large-scale vortices. At lower jet Reynolds numbers the majority

of images display features similar to those in Figure 6.2. As the Reynolds number increases, a greater proportion of images become convoluted (i.e. influenced by large-scale vortices, as determined by curvature of the OH layer), with features such as those shown in Figure 6.3. The size of these vortical structures is approximately the integral length scale ($\sim$5mm).

The effects of large-scale vortices on the reaction zone have already been discussed in Chapters 4 & 5. From Figure 6.3 it is seen that the LPG/H_2 flames respond to turbulent fluidic structure in a similar way. The representative images in Figure 6.3 all show signs of convolution, but essentially have the same features as seen in the typical images in Figure 6.2. For the selected images in Figure 6.3 there are only minor changes in the local OH concentration near the locations of convolution. This indicates only a change in the shape of the reaction, and not changes to the reaction itself.

6.4.3   Reaction Zone Weakening

In the preceding subsection (§6.4.2) it was identified that vortex interaction with the reaction zone can lead to a convolution of the OH layer, but change only the shape of the flame front and not the species concentrations. Nevertheless, as the flame front becomes convoluted and stretched by vortices, the OH images can show a localised decrease in concentration and a spatial thinning of the OH layer. The decrease in OH levels is defined as a weakening of the reaction zone. It is important to recognise that despite a weakening (i.e. a reduction in OH) an actual rupture of the OH layer is never observed.

The distribution of the measured scalars in Figure 6.4 suggests large-scale vortices are present in each of these images. In the strained region surrounding the vortices a weakening of the reaction zone is seen, evident by a local reduction in OH concentration and/or a thinning of the OH layer. Accompanying the weakening of the flame front can be an increase in H_2CO levels. An increase of H_2CO with strain has previously been noted in Chapter 4.

Irrespective of the fuel type, examples of weakening of the reaction zone (and subsequent increases in the H_2CO levels) are noted in both the 3% & 9% O_2 levels. In such cases it is apparent that the flow structure has an effect on the
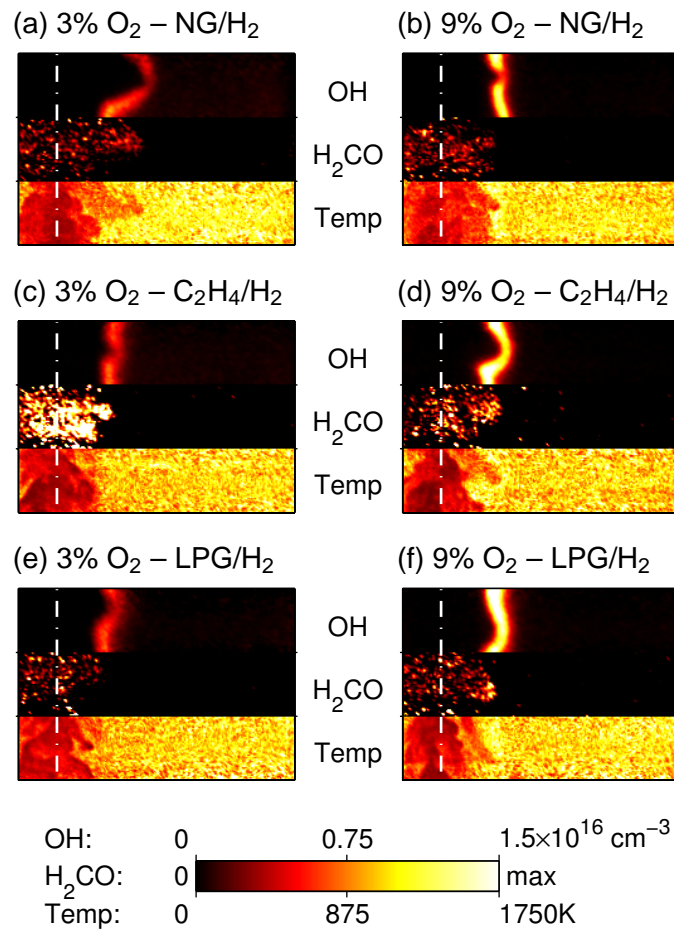
Figure 6.4: Selection of instantaneous OH, H_2CO and temperature image triplets of natural gas/H_2, C_2H_4/H_2 and LPG/H_2 flames showing vortex interaction with the reaction zone (reaction zone weakening). Re_{jet}=10,000. Each image 8×35mm. Jet centreline marked with dashed line. Axial location 35mm above jet exit.

reaction zone, and that all of the fuels are susceptible to this phenomenon. For the C_3H_8/H_2 flames, the effects are not quite as apparent. Nevertheless the same processes occur, albeit on a more subtle level.

As an extension to the weakening of the reaction zone, further convolution can lead to more dramatic flame features. In each of the images presented in Figure 6.5, what appears to be isolated "islands" of H_2CO are seen. In Figure 4.3 it was seen that partial premixing leads to significant increases in H_2CO concentrations. The low temperature of such islands suggest that these are unreacted pockets of fuel, and the higher H_2CO levels suggest some premixing has occurred. The formation of such H_2CO islands is not dissimilar to those seen previously in the natural gas / hydrogen flames in Figure 4.4. Unlike those in Figure 4.4, the isolated pockets of H_2CO in Figure 6.5 remain within the fuel-rich side of the reaction zone. The turbulent flow structure is responsible for these incidents. The features remain essentially constant for each fuel type, suggesting that the chemistry of the fuel does not have significant influence on these flames.

6.4.4   Radial Profiles – 35mm downstream

The instantaneous images presented suggest that each of the various fuel types have a very similar structure. This is also seen in the radial plots of Figure 6.6. At the 3% O_2 coflow the mean OH profiles seem quite coincident, with each fuel having a similar peak mean value and similar spatial shape. In both the mean and RMS, there is a slight shift of the OH profiles inward towards the centreline as the fuel complexity is increased. This radial shift corresponds to a drop in jet velocity required to maintain the jet Reynolds number. At the 9% O_2 coflow the radial shift of the OH peak with the fuel type is more noticeable. Also more noticeable for the 9% case is a variation in the mean OH peak, although the changes are still relatively small. Worth noting is that despite an almost three-fold difference in the jet exit velocity for the various fuels, because the Reynolds number is constant in all cases, the OH RMS is comparable for either O_2 level.

At both coflow O_2 levels, in the H_2CO profiles of Figure 6.6 a very significant increase is noted for the C_2H_4/H_2 flame. The mean H_2CO is distributed widely across the radial profiles, but does show evidence of a dip along the jet centreline,
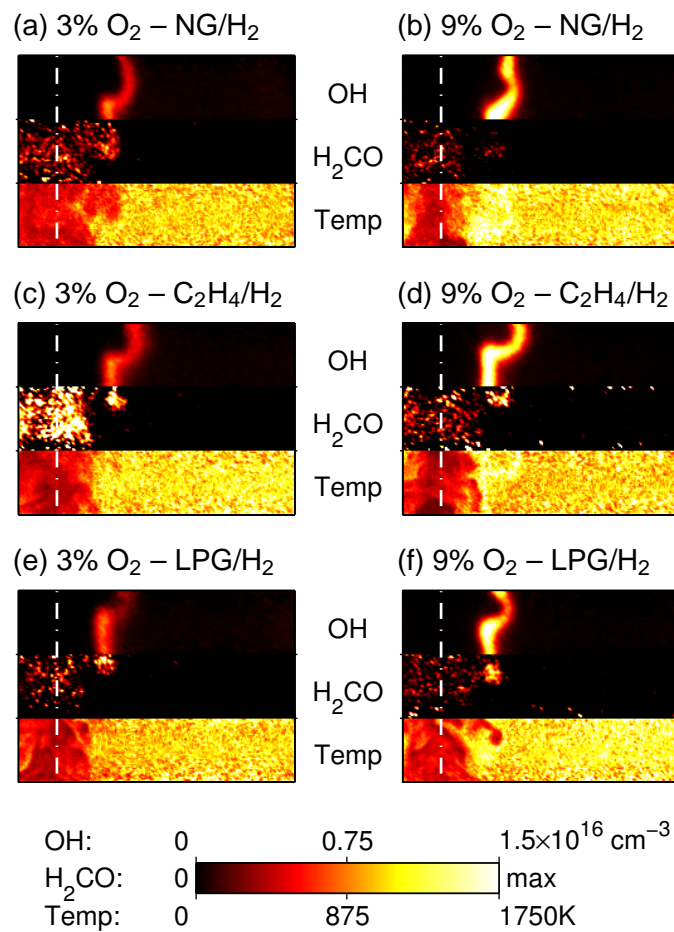
Figure 6.5: Selection of instantaneous OH, H_2CO and temperature image triplets of natural gas/H_2, C_2H_4/H_2 and LPG/H_2 flames showing isolated pockets of high H_2CO. Re_{jet}=10,000. Each image 8×35mm. Jet centreline marked with dashed line. Axial location 35mm above jet exit.
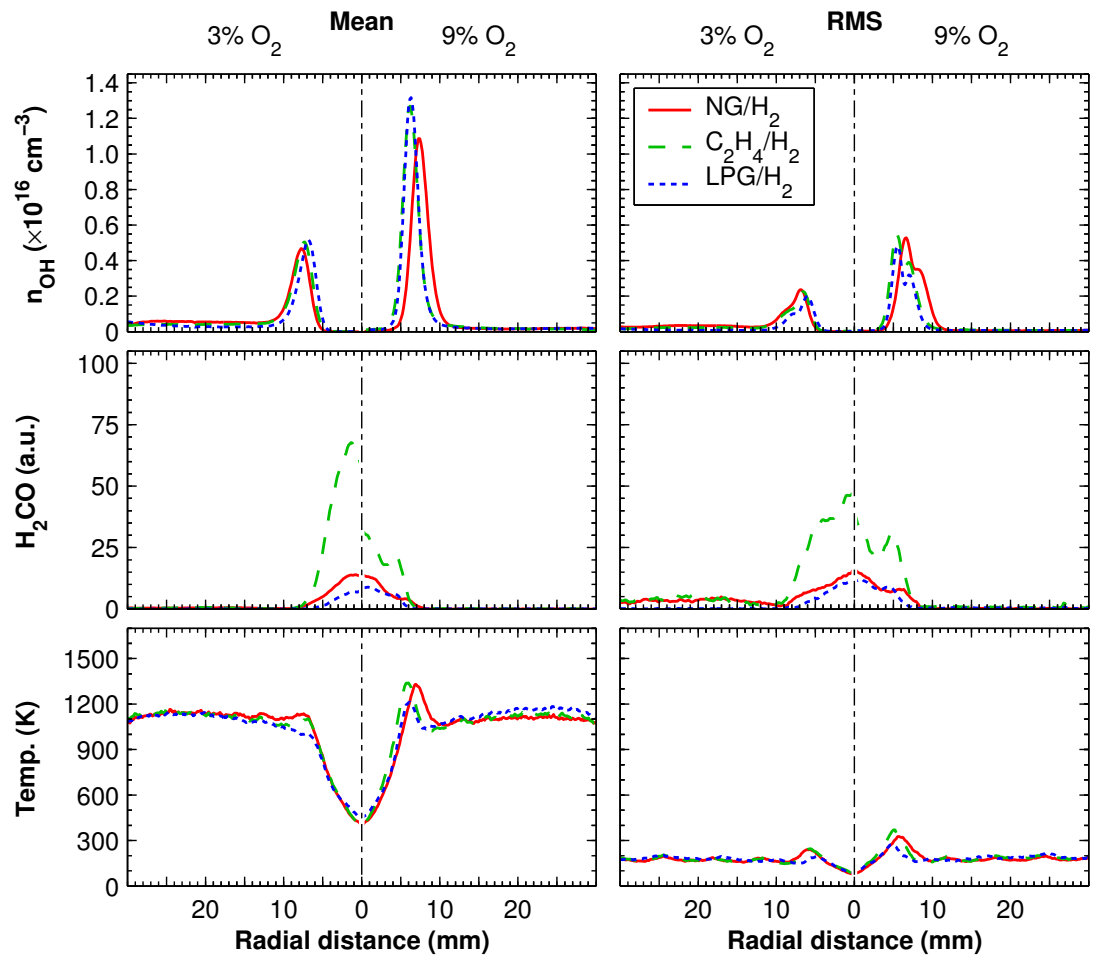
Figure 6.6: Mean and RMS radial profiles of OH, H_2CO and temperature for natural gas/H_2, C_2H_4/H_2 and LPG/H_2 flames. Re_{jet}=10,000. Central 3mm strip of images used. Axial location 35mm above jet exit.

suggesting that this effect is not due to potential fuel Raman interference. The broad radial distribution of H_2CO has already been discussed in Chapter 4. The H_2CO levels in the C_2H_4/H_2 flame are significantly higher with the 3% O_2 coflow as compared to 9% O_2, but for the other fuels (natural gas/H_2 & LPG/H_2) the H_2CO is similar at either O_2 level. These trends will be investigated further in §6.6.

As was noted in the instantaneous images, the temperature rise across the reaction zone in the 3% O_2 coflow is barely discernable. For the 3% O_2 LPG/H_2 flame the temperature rise is not resolved in the mean profile. The lack of temperature increase has been outlined in §3.9.4. At the 9% O_2 coflow, again the LPG/H_2 flame shows the lowest reaction zone temperature. The trends relating to the location of the peak temperature follows the same trend as seen in the OH profiles, viz. the peak shifts towards the centreline as the fuel complexity increases.

6.5 Results – 125mm downstream

As noted in the flame photographs (§6.3) the presence of soot at the 125mm location in the 9% O_2 flames restricts laser measurements to the 3% O_2 case only.

The radial profiles at the 35mm location (Figure 6.6) showed that each fuel type has very similar OH profiles. Despite the effects of surrounding air entrainment at the 125mm downstream location, in Figure 6.7 the OH profiles are again seen to be very similar. The C_2H_4/H_2 flame again leads to much stronger H_2CO levels than for the other fuels. At the 125mm downstream location, unlike at the 35mm location, the LPG/H_2 flame has a similar temperature profile to the other fuel types.

Figure 6.8 presents a selection of typical images for each of the fuel types at the 125mm location. These images show more-or-less similar features to those at the upstream location; the OH layer appears intact and relatively unconvoluted, and the H_2CO is quite broad and uniformly distributed. The temperature in the reaction zone is higher than was seen for the 3% O_2 flames at the 35mm location.
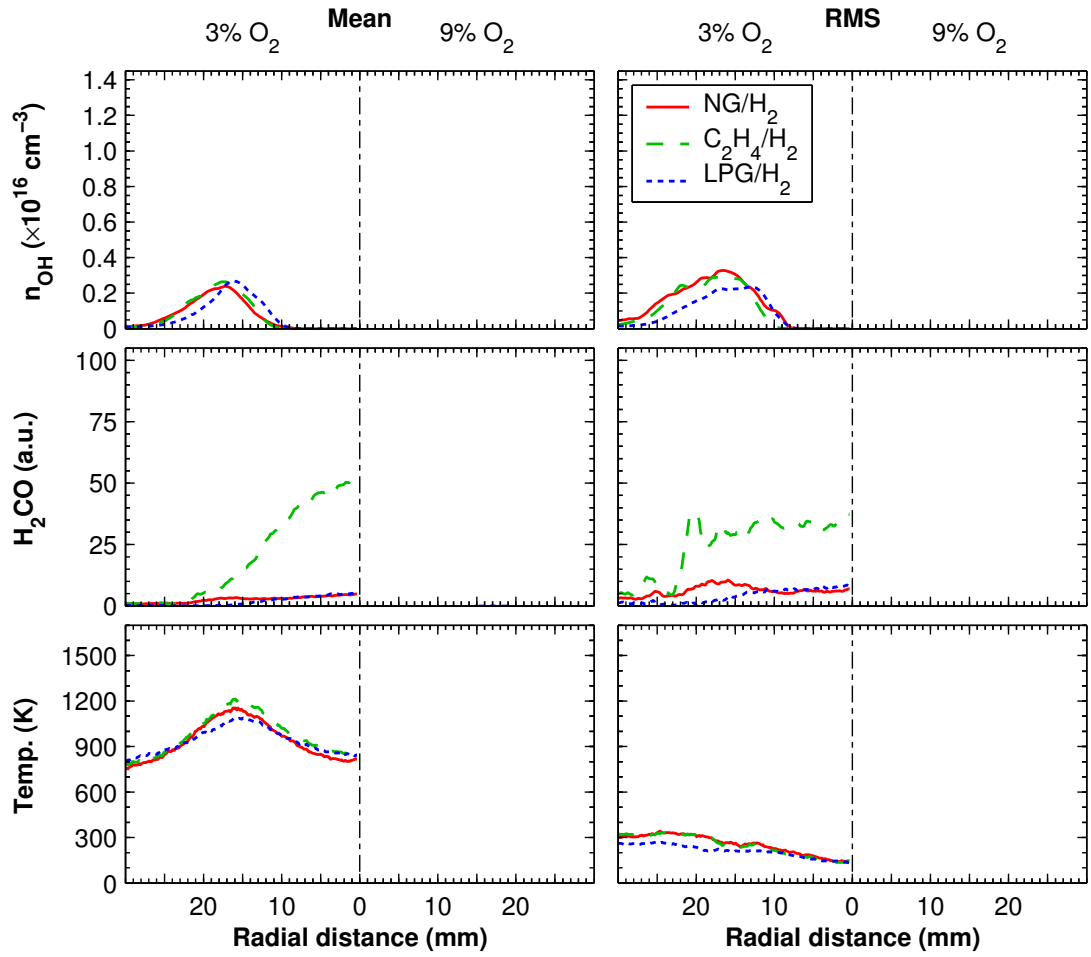
Figure 6.7: Mean and RMS radial profiles of OH, H_2CO and temperature for natural gas/H_2, C_2H_4/H_2 and LPG/H_2 flames. Re_{jet}=10,000. Central 3mm strip of images used. Axial location 125mm above jet exit.
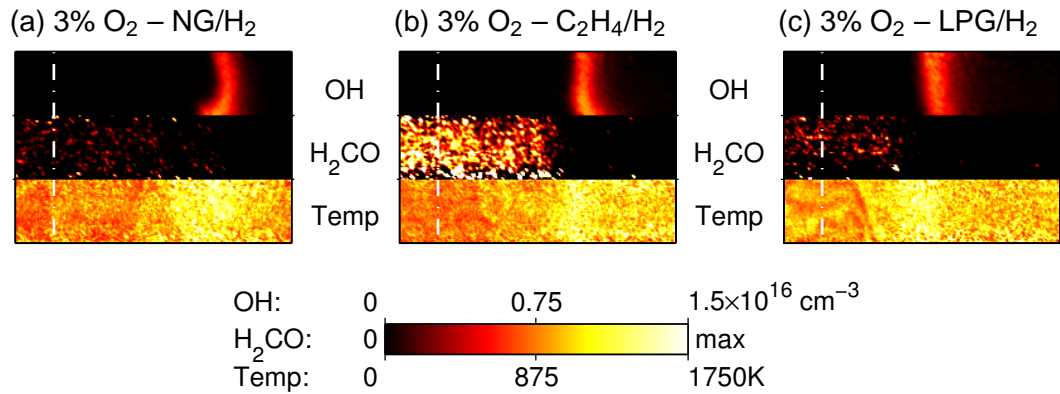
Figure 6.8: Selection of instantaneous OH, H_2CO and temperature image triplets of natural gas/H_2, C_2H_4/H_2 and LPG/H_2 flames showing typical features. Re_{jet}=10,000. Each image 8×35mm. Jet centreline marked with dashed line. Axial location 125mm above jet exit.

The measurements at the 125mm location, both in the radial plots of Figure 6.7 and the typical instantaneous images of Figure 6.8, support the observations from the 35mm location (§6.4) that the fuel type does not appear to have a significant influence on the reaction zone structure. Subsequent analysis of the data and strained laminar flame calculations presented later in §6.6 will provide support to the notion of relatively constant peak OH concentration between fuel types.

6.5.1 Examples of Downstream Fluidic Structure Effects

For the typical cases presented, the fuel type, and thus chemistry path, does not appear to play a major role in the structure of the reaction zone. The result of turbulent fluidic interaction can have a significant effect however. In Chapters 4 & 5 the effects of turbulent fluidic structure and surrounding air entrainment at the most downstream location have been considered. In this chapter, the effects of such fluidic structure are compared between the different fuel types.

By way of introduction, Figure 6.9 gives some examples of the effects of fluidic structure on the reaction zone. The appearance of the reaction zone in each of the cases in Figure 6.9 exhibit different features. The differences are attributed to fluidic structure differences rather than chemistry effects of the various fuels.
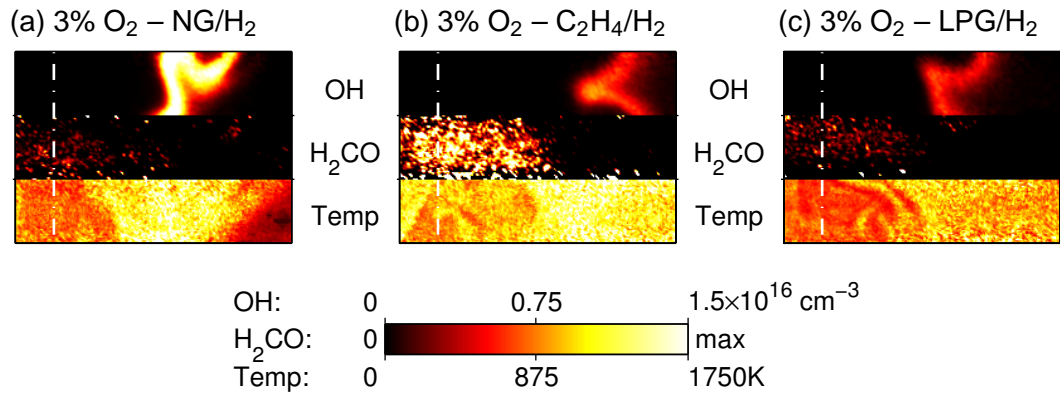
Figure 6.9: Selection of instantaneous OH, H_2CO and temperature image triplets of natural gas/H_2, C_2H_4/H_2 and LPG/H_2 flames showing various effects of convolution on the structure of the reaction zone. Re_{jet}=10,000. Each image 8×35mm. Jet centreline marked with dashed line. Axial location 125mm above jet exit.

Figure 6.9a shows an image where the OH has significant curvature. The peak OH in this image is substantially higher than seen in the typical image in Figure 6.8a. The oxidant stream temperature is also lower. Figure 6.9b shows some turbulent fluidic structure, this time without increases in the OH peak concentration, but with a significantly different shape of the OH. The OH is spatially separated from the H_2CO by a sizeable distance. The region between the OH and the H_2CO is where the highest temperatures occur. Figure 6.9c again has fluidic structure and a single continuous OH layer. The structure in this case appears to almost create a fork (or "Y" shape), with H_2CO (albeit small) in the created saddle point.

The features identified in Figure 6.9 are investigated further in the proceeding sections.

6.5.2 Multiple Reaction Zones

Similar features identified in the LPG/H_2 flame of Figure 6.9c have also been seen for other fuel types in previous chapters, for example Figures 4.2c, 4.7b & 5.7b. Such "forking" of the reaction zone is therefore apparent as being a fluidic property, and is common to all of the fuels. A more extreme example of reaction zone forking is seen in Figure 6.10a.
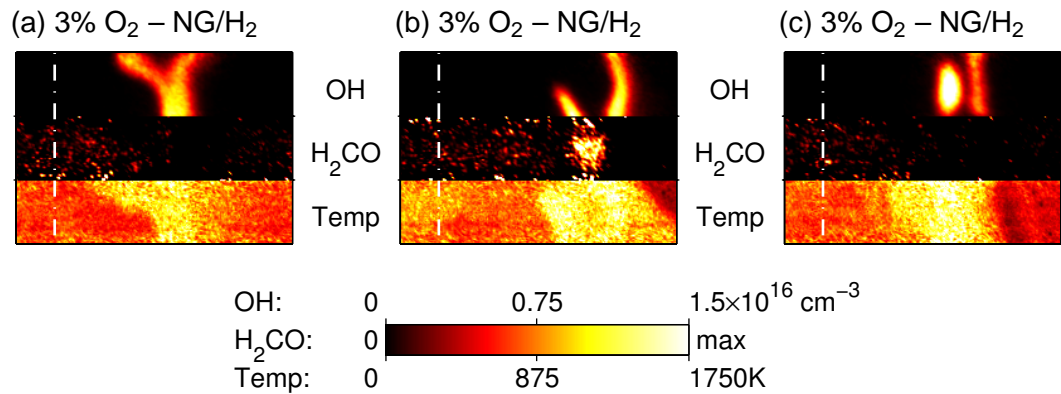
Figure 6.10: Selection of instantaneous OH, H_2CO and temperature image triplets of natural gas/H_2, C_2H_4/H_2 and LPG/H_2 flames showing multiple reaction zones. Re_{jet}=10,000. Each image 8×30mm. Jet centreline marked with dashed line. Axial location 125mm above jet exit.

As is seen in Figure 6.10b, the formation of forks in the reaction zone leads to the effect of a double, or multiple, reaction zone. It appears as though this image is the top portion of a fork, with strong H_2CO obvious between the two reaction zones that are formed. A slight drop in temperature is seen in the area corresponding to the high H_2CO. The cold air (evident by the lower temperature) which appears to the right of the image does not appear to have any influence on the reaction zone at the instance of this particular image. Figure 6.10c shows further evidence of the formation of multiple reaction zones. The OH on the left side is much stronger than on the right (oxidant) side of the reaction zone, where cooler temperatures are noted. The reaction zone adjacent to the lower temperatures, likely due to entrainment of surrounding air, appears to be less intense. A weakening, and subsequent strengthening, of the reaction zone with cold/cool oxidant has been noted in previous chapters.

It is recognised that the temperature images presented in Figure 6.10 may not be as reliable as in other situations. Identification of the fuel rich/lean boundary which is necessary for determining the Rayleigh cross-section is less straightforward when multiple OH layers are present. Nevertheless, even in these instances, the temperature images still reveal useful information.
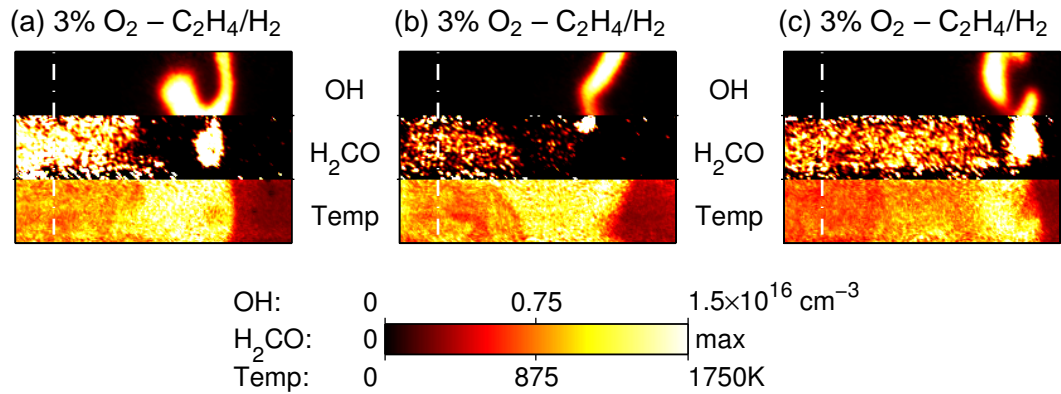
Figure 6.11: Selection of instantaneous OH, H_2CO and temperature image triplets of natural gas/H_2, C_2H_4/H_2 and LPG/H_2 flames showing effect of surrounding air entrainment. Re_{jet}=10,000. Each image 8×35mm. Jet centreline marked with dashed line. Axial location 125mm above jet exit.

6.5.3 Surrounding Air Entrainment

The similarity of the reaction zone for the different fuels is also noted in the effects of the combination of convolution and surrounding air entrainment. For the natural gas / hydrogen flames presented in Chapter 4 it was introduced that the surrounding air, which has a lower temperature and higher oxygen concentration, can lead to a higher reaction zone intensity. Similarly, this same process is seen for other fuels.

Figure 6.11a shows the presence of a vortex, and that the oxidant stream has a temperature much lower than the coflow. The features seen in this image suggest that the vortex has entrained fluid towards the centreline. Where the flame front (identified by the OH) is in contact with the cold air, the OH has a lower concentration than that which has been entrained. An isolated core of H_2CO is present at the centre of the vortex, and is accompanied by a localised region of slightly lower temperature. The presence of H_2CO within the vortex is evidence of it consisting of unreacted fuel, and given that the H_2CO signal is higher than the rest of the image suggests (partial) premixing has occurred. The lack of H_2CO between the central portion of the jet and the vortex suggests that this region is reacted, and consequently the higher temperature. Indeed, the temperature is higher than in the "typical" images. Similarly, the OH in the

vortex is higher due to the additional oxygen of the entrained fluid.

Figure 6.11b also shows the effects of surrounding air entrainment, but unlike Figure 6.11a, a vortex is not apparent. The OH suggests a single reaction zone, with cold oxidant still seen along the height of the image. The presence of a strong region of H_2CO indicates that some premixing has occurred. In the area adjacent to the strong H_2CO, the OH is also much higher than toward the bottom. It is proposed that the cold air has weakened the reaction zone (as has occurred toward the bottom of the image) and the higher oxygen concentration from the surrounding air has lead to partial premixing and subsequently an increased reaction rate (higher temperature and OH concentration).

Figure 6.11c has some similar features to Figure 6.11a. Again, the oxidant stream consists of cold air. A region of higher H_2CO is seen, suggesting some form of premixing. The additional oxygen in the air that is entrained leads to higher reaction rates (stronger OH and higher temperature) in the inner portions of the pocket. Conversely, as evident by the break in the OH surface, Figure 6.11c appears locally extinguished. Extinction of the flame front in contact with the surrounding air is noted, and is attributed to cooling. The process of weaking/extinction of the flame front and the subsequent re-ignition with a stronger reaction rate was described in Chapter 4, and will be continued in the next section.

6.5.4 Localised Extinction Events

The example of localised extinction seen in Figure 6.11c was for a C_2H_4/H_2 flame. Evidence of such extinction events are seen for all of the fuel types (natural gas/H_2, C_2H_4/H_2 & LPG/H_2). From visual observation, the frequency of extinction events (for $Re_{jet} = 10,000$) are approximately; $\sim 12\%$ for natural gas/H_2, $\sim 1.5\%$ for C_2H_4/H_2 and $\sim 1\%$ for LPG/H_2 flames.

Extinction of natural gas / H_2 flames was covered in detail in Chapter 4, and was attributed to cooling effects. Local extinction is common to all fuel types, and Figure 6.12 shows a further selection of locally extinct natural gas/H_2 flames to briefly review the extinction process. The cold surrounding air entrainment appears to be the cause of the extinction in Figure 6.12a. In this image, both the OH concentration and reaction zone temperature are very low, and a small region
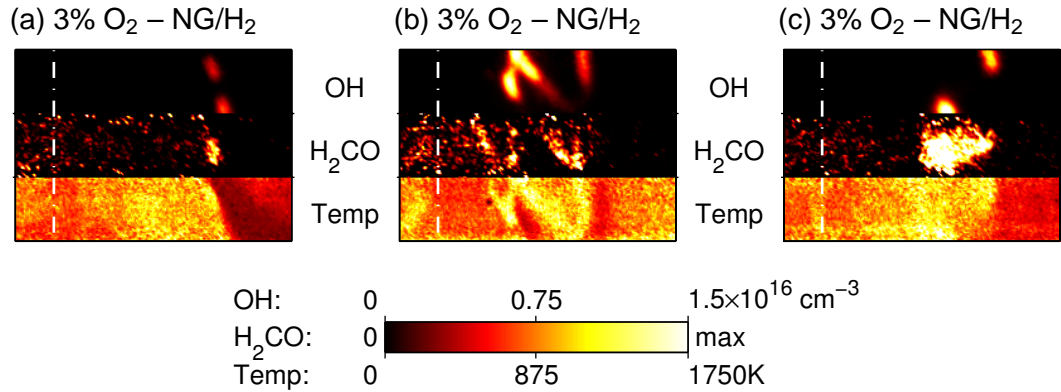
Figure 6.12: Selection of instantaneous OH, H$_2$CO and temperature image triplets of natural gas/H$_2$, C$_2$H$_4$/H$_2$ and LPG/H$_2$ flames showing localised extinction. Re_{jet}=10,000. Each image 8×35mm. Jet centreline marked with dashed line. Axial location 125mm above jet exit.

of high H$_2$CO signal is noted corresponding to a break in the OH surface. Figure 6.12b shows a far more convoluted reaction zone, with signs of very localised extinction indicated by breaks in the OH layer. Accompanying the weakening of the OH is a strengthening of the H$_2$CO, as has been noted previously. Along the length of the reaction zone, whether indicated by either the OH or H$_2$CO, the temperature remains high and quite constant. Adjacent to the region of high temperature a slightly cooler region can be identified. Another example of extinction, but without an obvious sign of cold air, is seen in Figure 6.12c. In this example, very strong H$_2$CO is seen corresponding to a break in the OH which is indicative of an extinction event, but the temperature of the oxidant stream is not as low as seen in the other examples with extinction.

6.5.5   Spatial Mismatch of OH & H$_2$CO

An interesting feature noted in many of the presented images without extinction is the spatial mismatch between the H$_2$CO in the central jet fluid and the OH layer. This is noted for each of the fuel types, as shown in Figure 6.13. The mismatch between the OH and H$_2$CO has been previously noted (§5.6). In the images in Figure 6.13 the region of high temperature is bordered to the left by the H$_2$CO and by OH on the right. It is generally expected for conventional
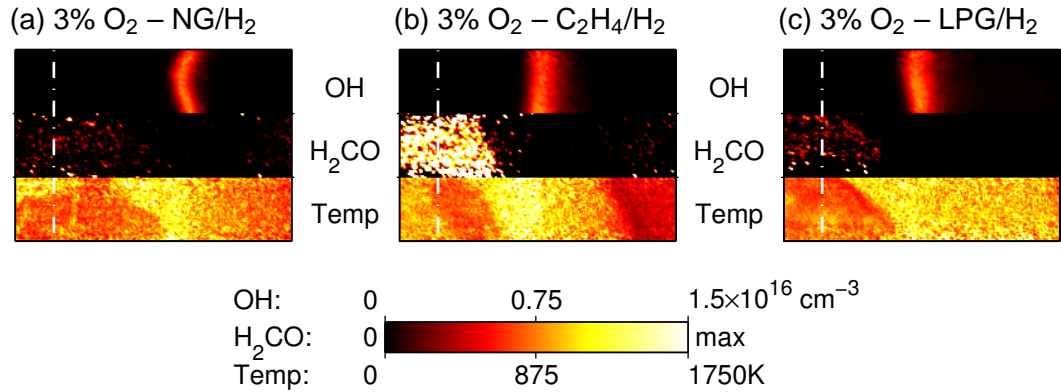
Figure 6.13: Selection of instantaneous OH, H_2CO and temperature image triplets of natural gas/H_2, C_2H_4/H_2 and LPG/H_2 flames showing spatial mismatch between OH and H_2CO. Re_{jet}=10,000. Each image 8×35mm. Jet centreline marked with dashed line. Axial location 125mm above jet exit.

flames that the highest heat release occurs in the region of overlap of OH and H_2CO. In these images there is not a physical overlap of the two species, but the high temperatures between them suggests that the heat release does occur in this region. The relationship between OH and H_2CO will be dealt with further in §7.5.

6.6 General Discussion

There does not seem to be any significant effect of the fuel type on the structure of the reaction zone from the instantaneous images and the radial profiles that have been presented. The trends obtained from methane and propane fuels have previously been noted as being similar in a heated and diluted oxidant stream in a spectral emission study with a different burner configuration [56].

Of the measured scalars, the H_2CO number density changes the most between the different fuel types considered. Nonetheless, the basic behaviour of the H_2CO is essentially constant between the different fuel cases. Changes in the flow structure are also apparent for the different fuel types. These differences arise because of the different jet velocity for each fuel type (required to maintain constant Reynolds number). Despite these minor differences, the fuel type does not lead to any

OH number density ($\times 10^{16}$ cm^{-3}) [σ]				
Location	Coflow	NG/H$_2$	C$_2$H$_4$/H$_2$	C$_3$H$_8$/H$_2$
35mm	3% O$_2$	0.56 [11%]	0.56 [10%]	0.54 [9%]
	9% O$_2$	1.28 [11%]	1.53 [30%]	1.33 [8%]
125mm	3% O$_2$	0.69 [46%]	0.65 [29%]	0.56 [12%]

Table 6.2: Mean and standard deviation (σ, in brackets) of peak OH number density measurements.

major changes in the overall flame characteristics at the measurement locations.

The photographs of the flames (Figure 6.1) provide supplemental evidence supporting the similarity of the different fuel types when in the confines of the hot and diluted coflow. Further downstream, after the effects of the coflow have diminished, each of the flames visually appear significantly different. This is suggestive of the importance of the coflow in establishment of the unique conditions which lead to the similarity between the different fuels.

Table 6.2 shows the averaged peak OH values in each of the images for a particular flame. Also included is the standard deviation (as a percentage) of the values. In determining the peak value in each of the images, only the central 3mm portion of the image is included to avoid over-corrected values towards the edges of the images where the low laser power makes sheet corrections less reliable.

From the radial profiles (Figures 6.6 & 6.7) for all cases the peak of the mean OH at the 125mm location was around half that at 35mm. In comparison, Table 6.2 shows an increase in the mean of the peak OH concentrations at the 125mm downstream location. Increases in the mean peak OH at the 125mm downstream location has been observed in the previous Chapters 4 & 5 and is due to the entrainment of surrounding air containing much more oxygen than is present in the coflow at the 35mm location. The OH radial profiles show a drop in the peak mean OH because at the 125mm downstream location the turbulent spreading of the jet causes the reaction zone to effectively become spatially averaged over a wider radial area.

Table 6.2 reiterates the similarity of the OH levels for the different fuel compositions. At the 35mm location, where the oxidant composition is well defined

Fuel composition (jet)	Peak temp. (K)		Peak n_{OH} ($\times 10^{16}$ cm^{-3})		Peak n_{H_2CO} ($\times 10^{14}$ cm^{-3})	
	3%	9%	3%	9%	3%	9%
CH_4/H_2	1400	1876	0.40	2.04	1.15	1.93
C_2H_4/H_2	1403	1856	0.46	2.11	2.59	0.87
C_3H_8/H_2	1384	1807	0.43	1.97	1.60	1.45

Table 6.3: Peak temperature and OH & H_2CO number density from strained laminar flame calculations ($a \approx 200$s^{-1}).

and not yet affected by surrounding air entrainment, comparisons of the trends can be made to strained laminar flame calculations. Table 6.3 presents the peak temperature, and the maximum number density of OH and H_2CO for each fuel type and at both O_2 levels obtained from OPPDIF calculations of the Chemkin package using GRI-Mech 3.0 mechanism.

Comparing Tables 6.2 & 6.3 it is seen that calculations support the measurements, in that the OH concentration does not change significantly with the fuel composition. The experimental peak OH value for the 3% O_2 flames is higher than from the calculations, whereas at 9% O_2 the calculated value is higher than that found from the experiment. The typical differences between the measured value and calculations is approximately 25% for 3% O_2 and $\sim$40% for 9% O_2. Nevertheless, there is good similarity of the trends, and also a similar order of magnitude between the experiments and calculations.

Table 6.3 shows that the H_2CO in the C_2H_4/H_2 flame behaves the opposite to the other two fuels. For C_2H_4/H_2 the H_2CO significantly increases at the lower O_2 case. In contrast, the effect of O_2 on H_2CO is comparatively minor for the other fuels. For C_3H_8/H_2 there is little difference between the two O_2 levels. In the CH_4/H_2 flame the trend is reversed and H_2CO slightly increases with O_2 level. The different behaviour of the H_2CO in the C_2H_4/H_2 flames to the other fuels was also apparent in the experimental data presented. Of particular note in the C_2H_4/H_2 flames was that the H_2CO levels in the 3% O_2 flames was much higher than the other cases, which is consistent with the laminar flame calculations (Table 6.3). At 9% O_2, Table 6.3 indicates that the C_2H_4/H_2 flame should have lower H_2CO than the other flames, which is not seen in the experimental data. Nevertheless, in general, the trends of H_2CO largely follow those predicted by

the flame calculations shown in Table 6.3.

To extend the comparison of the fuel type beyond the peak number density, Figures 6.14, 6.15 & 6.16 show selected species concentrations in mixture fraction space. The temperature and OH, H_2CO & HCO mole fractions were obtained from OPPDIF calculations of the Chemkin package using GRI-Mech 3.0 mechanism. A normalised mixture fraction (ξ^*) is used instead of the standard definition obtained from the calculations because of the non-standard oxidant stream composition. The normalised mixture fraction is defined by equation A.4 in Appendix A.3, and ensures that ξ^* ranges from zero in the oxidant stream to one in the fuel stream. To observe the features in Figures 6.14, 6.15 & 6.16 more clearly, the mixture fraction is only shown to 0.25, beyond which there are no features of interest.

Figures 6.14 and 6.15 indicate that the temperature rise across the reaction zone is ~350K for the 3% O_2 coflow flames, and ~800K for the 9% O_2 coflow case. These temperature increases are higher than the measured temperature results that have been presented for the 35mm location in this chapter, and also in Chapters 4 & 5. The low temperature rise across the reaction zone in the measurements has been discussed in §3.9.4, and it is believed that the low reaction zone temperatures are in fact genuine. It is worth highlighting that the measured coflow and jet potential core temperatures agree almost perfectly with the expected values (1100K in the coflow and ~400K along the jet centreline). As such, any interference that could potentially lead to erroneous temperatures must be localised around the reaction zone. The flames are free of any visible signs of soot at the 35mm location. It seems unlikely that other sources of interference could explain the large discrepancy of the calculated peak temperature with the measurements.

Consistent with the measurements, the OH profiles in Figure 6.14 virtually overlap, both in location and peak value. There are some minor differences in the width of the OH profiles in Figure 6.14, but when normalised, the FWHM (full-width half-maximum) width varies by only around ~5%. Similarly, the temperature profiles in Figure 6.14 across the reaction zone are also very similar, and virtually overlap for the different fuel types. At higher mixture fractions, the temperature for the CH_4/H_2 flame does roll-off a little faster than the others, but the differences are relatively minor. The general observations regarding OH and
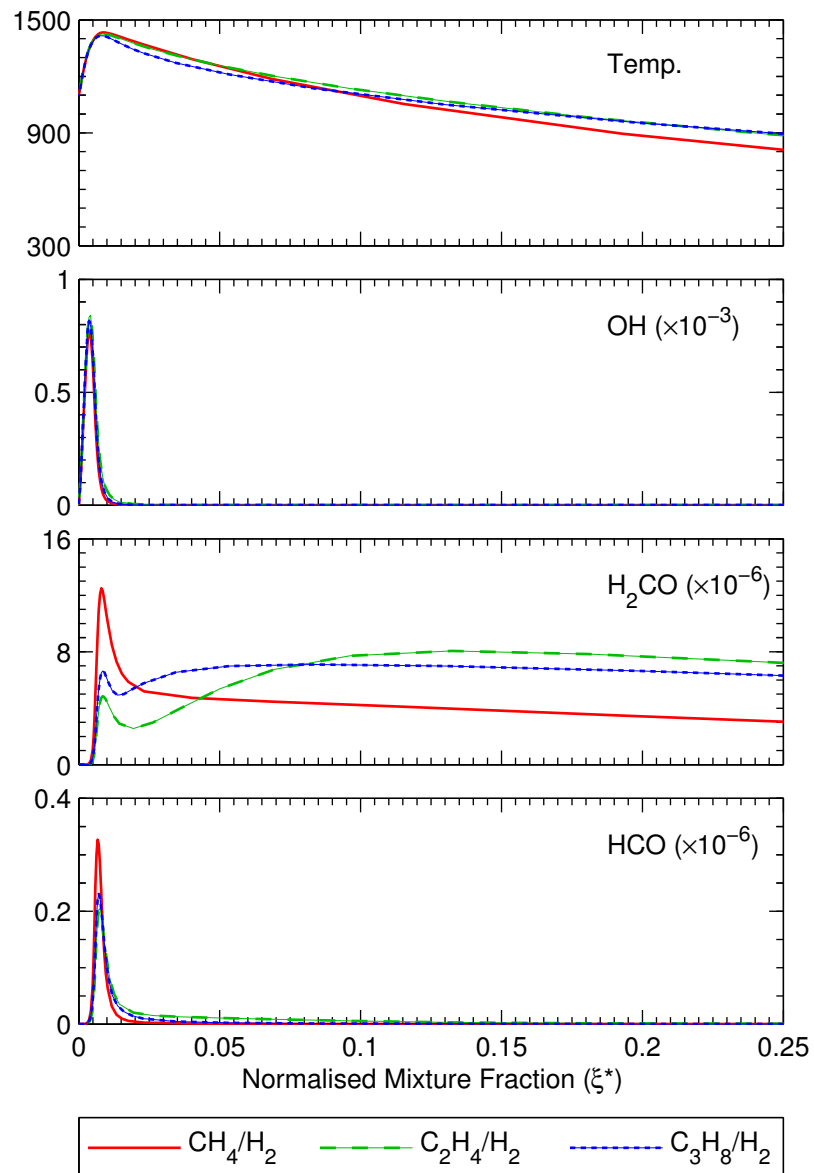
Figure 6.14: Temperature and species mole fractions from strained laminar flame calculations in (normalised) mixture fraction space for 3% O_2 coflow composition ($a \approx 100s^{-1}$).

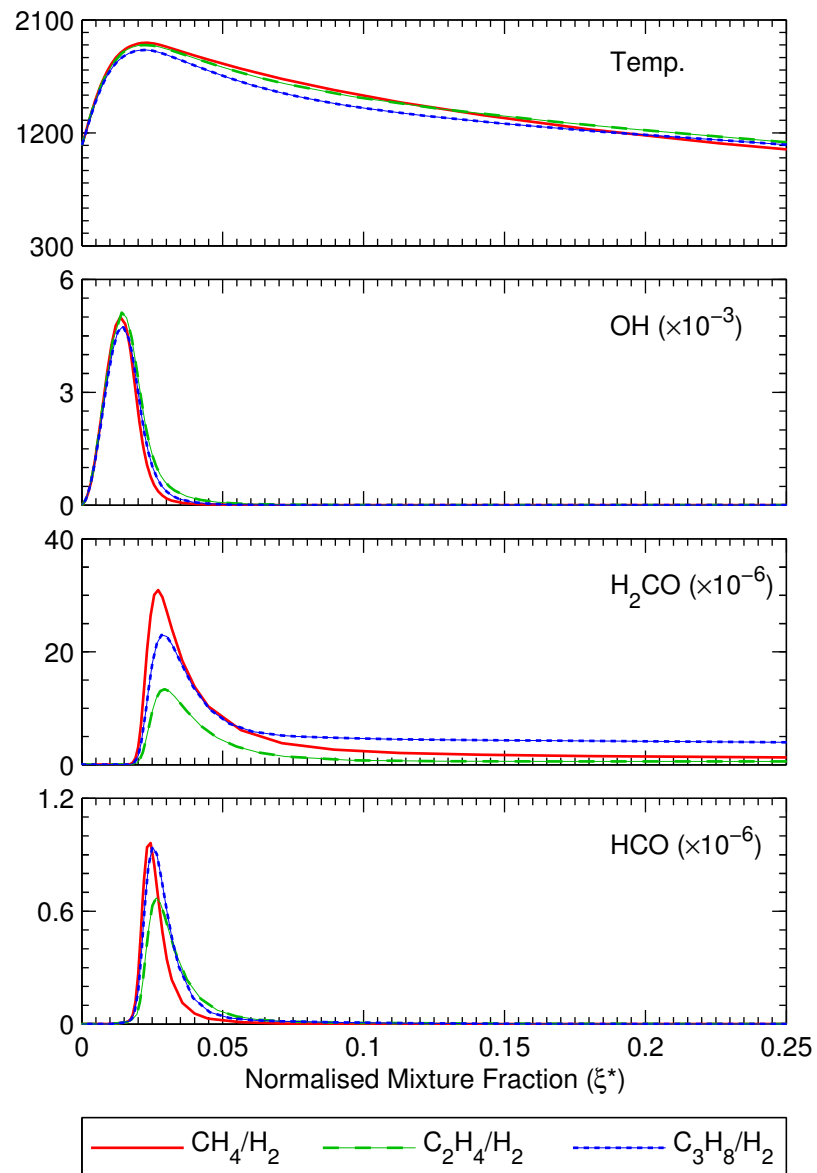**Figure 6.15:** Temperature and species mole fractions from strained laminar flame calculations in (normalised) mixture fraction space for 9% O_2 coflow composition ($a \approx 100s^{-1}$).
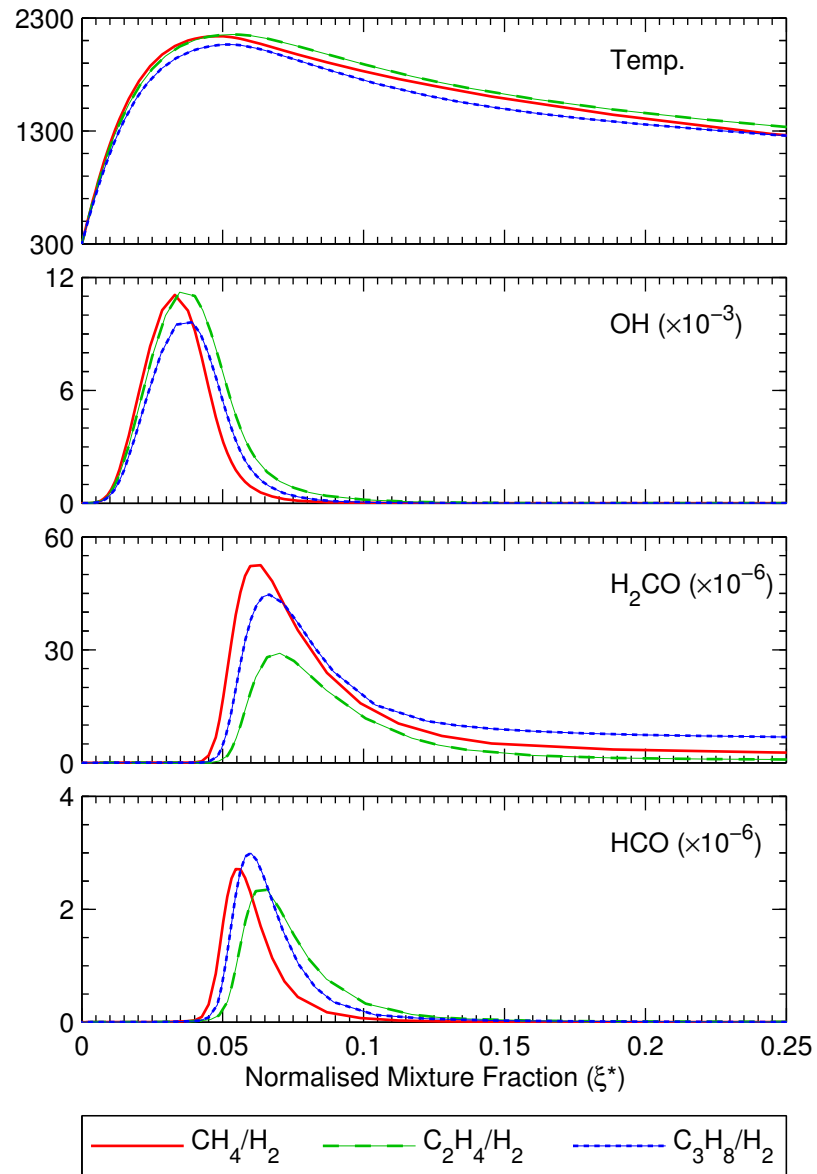
Figure 6.16: Temperature and species mole fractions from strained laminar flame calculations in (normalised) mixture fraction space for (21% O_2, 300K) air ($a \approx 100s^{-1}$).

temperature confirm the experimental result that the fuel type has only minor effects on the reaction zone structure.

While the OH and temperature do not seem to vary significantly with the type of fuel, from Figure 6.14 H_2CO does show very different behaviour depending on the fuel type. In all cases, H_2CO is found almost over the entire range of mixture fraction, extending well beyond the presented range. This explains the very wide radial distribution of H_2CO in the images and reinforces that PAH or Raman interference is not responsible for the distribution seen in the measurements. It is only for the CH_4 flame that the H_2CO peak is located near the stoichiometric mixture fraction. Both the C_2H_4 and C_3H_8 flames reach a local maximum around stoichiometry, but further toward the fuel rich side the H_2CO concentration dips slightly and then increases again, such that the peak H_2CO concentration is well away from stoichiometry.

Also plotted on Figure 6.14 is the HCO mole fraction. As expected, HCO lies in between the OH and H_2CO profiles. The HCO profile does change somewhat with the fuel type. For CH_4/H_2 the HCO is narrower but has a higher peak, whereas C_2H_4/H_2 and C_3H_8/H_2 are more spread out, but only slightly more so.

For the 9% O_2 coflow case, Figure 6.15 shows the same profiles as Figure 6.14. The temperature, OH and HCO all seem to have a similar response to the fuel type as already noted for the 3% O_2 case. The location of the OH peak again does not seem to be highly dependent on the fuel type, and the peak concentration is also relatively constant. At 9% O_2 the differences between the different fuels are somewhat more pronounced, but the general trends and observations are comparable. Again, at 9% O_2 the H_2CO distribution is seen to be wide, extending well into the fuel rich side. Unlike at 3% O_2, at 9% O_2 the H_2CO profiles do not change quite as significantly with fuel type, although the differences are still noticeable. The basic profile for each of the fuels is somewhat consistent, with a peak just to the rich side of stoichiometry and a long tail extending further to the fuel rich side. The stoichiometric mixture fraction, as indicated by the HCO peak, is seen to shift between the different fuels more for 9% O_2 than for 3% O_2. This shift in stoichiometry becomes more noticeable as the stoichiometric mixture fraction becomes larger, but is still relatively small.

To compare the similarity of the reaction zone structure for the different fuels

under the hot and diluted O_2 conditions, strained laminar flame calculation results are shown for standard air (21% O_2, 300K) in Figure 6.16. Apparent is that unlike for the MILD combustion conditions, the fuel type does lead to clear differences in the species profiles. While the OH profiles remain similar, in comparison to the 3% and 9% O_2, 1100K temperature oxidant stream case, the OH profiles are no longer coincident. This suggests that the MILD combustion conditions are fundamentally responsible for bringing about the similarity of the temperature and OH profiles for the different fuels.

Apart from the differences in the H_2CO levels for the C_2H_4/H_2 flame, the effect of the fuel type does not seem to have a marked effect on the overall structure of the reaction zone. It was noted that the natural gas / H_2 flame has a greater likelihood of localised extinction at the 125mm downstream location. This is not attributed to a chemistry effect, rather, the natural gas / H_2 flame has a higher jet velocity, and so tends to induce a greater stirring motion, entraining more surrounding air, which leads to more frequent localised rupture of the flame front. The lower velocity of the C_2H_4/H_2 and LPG/H_2 flames tends to reduce the interaction of the flame front with the surrounding air and so extinction events occur less often, but when they do, the features are identical.

The comparison between the three different gaseous hydrocarbon fuels in this chapter reveal that the fuel type does not have a significant effect on the reaction zone structure under MILD combustion conditions. It is important to highlight that each of the primary fuels are diluted with hydrogen (H_2) in equal volumetric parts. The addition of H_2 is necessary to increase the flame stability to prevent blowoff. Hydrogen also shifts the stoichiometric mixture fraction to the lean side, towards the edge of the shear layer. The H_2 added to the fuel stream seems to influence the kinetics such that the different hydrocarbon fuels show similar characteristics. The effect of hydrogen on the kinetics is elaborated further in §7.4.1.

Chapter 7

Summary & Discussion

7.1 Introduction

The results presented in Chapters 4, 5 & 6 have revealed many interesting phenomenon relating to jet in hot and diluted coflow flames which emulate MILD combustion conditions. In this chapter the significance of these results will be put in the overall context of MILD combustion.

By way of a brief summary, there are some fundamental features which have been identified as being common to all of the cases considered. With a reduction in the coflow O_2 level, the OH concentration is seen to drop. To a lesser extent, the structure and distribution of the OH layer also changes with the jet Reynolds number and fuel type. The H_2CO levels vary significantly with changes in flame parameters. There are some typical features which are seen in all cases however. H_2CO is formed early in the combustion process, and appears on the fuel-rich side of the reaction zone.

The relationship between OH and H_2CO extends beyond simply indicating the fuel lean and rich sides of the reaction zone. This is particularly evident in situations where the flame front becomes convoluted or weakened. Convolution is the term used when the reaction zone is subject to interaction with large-scale vortices. Weakening is defined as a localised reduction in concentration and/or a spatial thinning of the OH layer. Observations relating to a weakening, or even

localised extinction, of the flame front are noted at various flame locations and conditions.

The influence of the fuel type, and subsequent changes in the kinetics, do not seem to play a major role in combustion under MILD conditions. Each hydrocarbon fuel considered shows similar features in the reaction zone. In particular, the OH concentration is seen to be very similar for the different gaseous fuels when mixed with hydrogen. Conversely, dilution of the fuel can have a major effect on the reaction zone. Depending on the diluent, some flames visually appear lifted. However, the results suggest that such flames may not, in fact, be lifted.

The importance of these aspects to MILD combustion are dealt with throughout the remainder of this chapter.

7.2 Effect of O_2 level

One of the key parameters in the establishment of MILD combustion conditions is the low oxygen environment. Strong recirculation of combustion products distributes and dilutes O_2 in a MILD furnace. While the O_2 concentration is low, on a global level MILD combustion furnaces are operated lean.

The low oxygen levels encountered in MILD combustion leads to a reduction in peak temperatures. For the jet in hot and diluted coflow flames, the temperature peak is only slightly above the coflow temperature. The recorded temperature images indicate that for a 9% O_2 coflow a distinct temperature peak is noted around the reaction zone. For the lower (3%) O_2 case the temperature peak is barely discernable. Nevertheless, the species measurements reveal the definite occurrence of combustion reactions.

Directly related to the temperature reduction at the low O_2 levels is a suppression of the OH concentration. For the fuel types and compositions considered, OH is typically reduced by a factor of $\sim$2–3 at 3% O_2 as compared to the 9% O_2 coflow. A further consequence of reducing the coflow O_2 concentration is a slight broadening of the width of the OH layer. The reduced oxygen concentration requires a greater volume of oxidant stream to consume the fuel. As such, the 3% O_2 coflow flames have a thicker OH width as compared to the 9% O_2 case.

The significant effect of the coflow O_2 level on the peak flame temperature highlights the importance of maintaining a low O_2 concentration surrounding the jet in order to maintain MILD combustion conditions. It is essential to keep the local O_2 level low to avoid high peak temperatures, and thus maintain the low NO_x production that typifies MILD combustion.

7.3   Turbulence Chemistry Interaction

Although imaging of temperature and flame intermediates does not provide measurement of flow field properties, the physical appearance of the measured scalars does enable the flow structure to be identified. In some situations the effect of turbulent fluidic structure can have a significant impact on the reaction zone structure. The two measurement locations were specifically chosen to represent two different oxidant stream compositions, and the flow structure at each location is very different.

Near the jet exit (35mm downstream location) the oxidant stream consists entirely of the well defined coflow. At this location, fluidic structure is brought about from the turbulence generated by the jet. At the downstream location furthest from the jet exit, surrounding air also mixes with the jet and the coflow, giving rise to a three stream mixing scenario. The turbulence at the most downstream location introduces cold, comparatively high oxygen laden air from the surrounds. The cooler temperatures and higher O_2 levels enable the effects of surrounding air entrainment on the reaction zone structure to be identified.

7.3.1   Convolution

Typically, near the jet exit the images do not show evidence of large-scale vortices. The jet shear layer appears unconvoluted, despite the jet flow being turbulent (based on jet Reynolds number). The lack of apparent large-scale turbulence suggests flow laminarisation may occur, likely as a result of the viscosity effects of the hot coflow. Nonetheless, a proportion of images do show signs of large-scale vortices, as indicated by convolution of the temperature and/or flame species.

The effects of convolution of the shear layer is often seen to have only minor effects on the reaction zone structure. In the area surrounding the vortex, the measured species concentration and temperature do not change. The distribution of the measured scalars only seems to follow the curvature of the shear layer. This observation is related to the strain effects discussed in §4.7.3. It has been seen that the peak OH concentration is quite insensitive to the strain rate. Furthermore, in §4.7.1 it was mentioned that the extinction strain rate for the hot and diluted coflow conditions is much higher than for conventional oxidant stream conditions.

Increasing the jet Reynolds number increases the frequency of images showing evidence of convolution from large-scale vortices, but the features seen in the images remain essentially the same as in the "typical" unconvoluted case. At the most downstream location, the turbulent flow structures become larger and the effects are far more apparent. Aside from instances where surrounding air is involved, at the most downstream location the convolution still has quite minor effects on the reaction zone structure.

7.3.2 Reaction Zone Weakening

7.3.2.1 Effect on OH

The convolution process discussed in the preceding subsection (§7.3.1) outlined that the effects of vortex interaction with the shear layer can simply alter the shape of the measured scalars and not affect the reaction zone structure itself. Nevertheless, as the flow becomes more convoluted and stretched by vortices, the OH images can show a localised decrease in concentration and a spatial thinning. The phenomenon relating to reductions in the OH layer is described as a "weakening" of the flame front.

The interaction of the vortices with the reaction zone intuitively suggests that flame stretch leads to the observed reduction in OH concentration. However, both the experimental results (Figure 4.5 & Table 4.6) and the laminar flame calculations (Figure 4.10) clearly indicate that the strain rate does not appear to significantly alter the OH. The reaction zone weakening seen in the instantaneous images is attributed not only to the strain imposed by the vortices, but also the
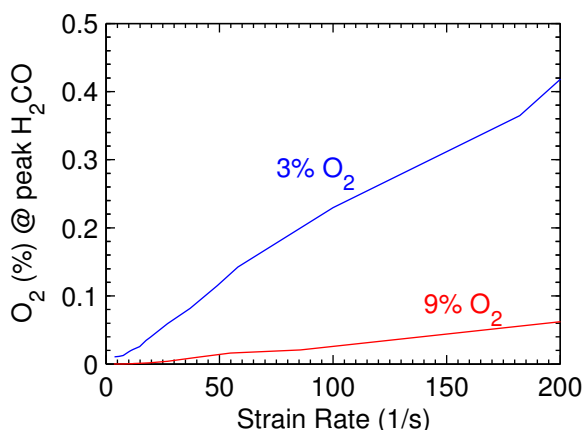
Figure 7.1: Laminar flame calculation of O_2 mole fraction (%) at location of peak H_2CO concentration as a function of strain for methane/hydrogen flames at two oxidant stream O_2 levels.
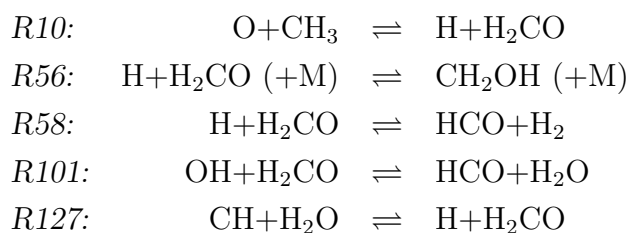
associated large-scale turbulent mixing. Strain rate alone does not lead to major changes in OH concentration, but in combination with large-scale turbulent mixing, vortex interaction with the reaction zone can lead to the weakening processes observed.

7.3.2.2   Effect on H_2CO

Unlike the OH, the H_2CO has been seen to increase with strain from both the experimental measurements (Figure 4.5) and from laminar flame calculations (Figure 4.11). H_2CO has also been shown to increase with the extent of partial premixing (Figure 4.3). To investigate the possibility of a connection between these two observations, the O_2 concentration at the location of peak H_2CO is plotted against strain rate in Figure 7.1. The details of these calculations are included in Appendix A.8.

Figure 7.1 suggests there may indeed be a relationship between strain and partial premixing. Since H_2CO is formed on the fuel-rich side, the O_2 concentration at the location of peak H_2CO is indicative of the amount of O_2 which has diffused across the flame front. It is apparent that as strain is increased, the amount of O_2 on the fuel-rich side increases also. This process perhaps suggests a form of strain-induced partial premixing (via diffusion), and is worthy of further investigation.

The H_2CO production rates have been analysed from laminar flame calculations. Details of these calculations are outlined in Appendix A.10. For CH_4/H_2 flames, two strain rate conditions have been chosen to differentiate between low and high strain. For both the 3% & 9% O_2 coflow cases, five main reactions have been found to be responsible for the majority of H_2CO formation and consumption. The key reactions identified are;

$$
\begin{aligned}
R10: & & O+CH_3 & \rightleftharpoons H+H_2CO \\
R56: & & H+H_2CO\ (+M) & \rightleftharpoons CH_2OH\ (+M) \\
R58: & & H+H_2CO & \rightleftharpoons HCO+H_2 \\
R101: & & OH+H_2CO & \rightleftharpoons HCO+H_2O \\
R127: & & CH+H_2O & \rightleftharpoons H+H_2CO
\end{aligned}
$$

For the 3% O_2 oxidant stream case, Figures 7.2 & 7.3 show the production rate of H_2CO plotted against mixture fraction for the five selected reactions at two different strain rates. As described in Appendix A.3 the standard definition of mixture fraction is not well defined for diluted oxidant stream conditions. Instead, a normalised mixture fraction, ξ^* (equation A.4) is used in Figures 7.2 & 7.3 to ensure that ξ^* ranges from zero in the oxidant stream to one in the fuel stream.

Reactions R10 and R127 are the main contributors to H_2CO production. H_2CO production via R10 increases by a factor of ten between the two strain rates considered. In comparison, R127 increases by a factor of three. The increase of H_2CO production as the strain rate is increased is consistent with Figure 4.11. Accompanying the increase in H_2CO production is also an increase in the consumption rate. Reactions rates for R58 and R101 increase by a factor of five and three, respectively, between the two strain rate cases. Nevertheless, the large increase in the reaction rate of R10 with strain over-compensates for the differences in consumption, leading to the higher H_2CO concentration.

The rate of H_2CO production via reaction R10 for the two strain cases under consideration are shown in Figures 7.4 & 7.5. Also shown in these figures are the species relevant to H_2CO production via reaction R10 (viz. O and CH_3). A vertical line is included as a reference point at the location of the peak nett H_2CO production rate. At this mixture fraction, it is noted that the O concentration is very low for the low strain case, but is significantly (five fold) higher at the
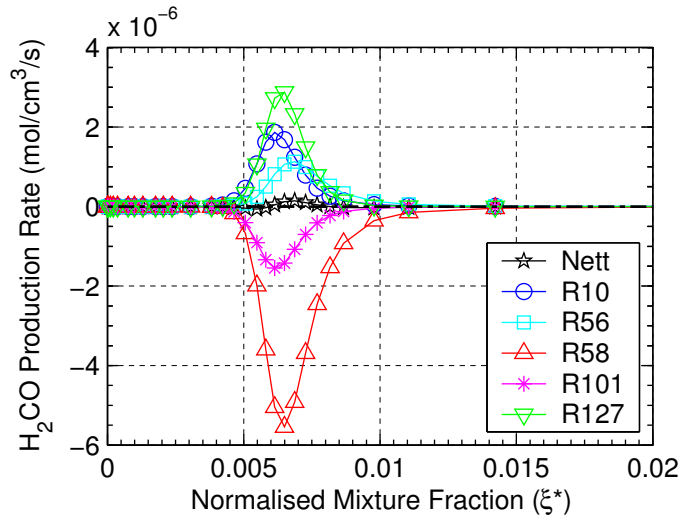
Figure 7.2: H$_2$CO production rate via major reactions, found from laminar flame calculations. CH$_4$/H$_2$ fuel with 3% O$_2$, 1100K oxidant stream. Strain rate, $a{\approx}30\mathrm{s}^{-1}$.
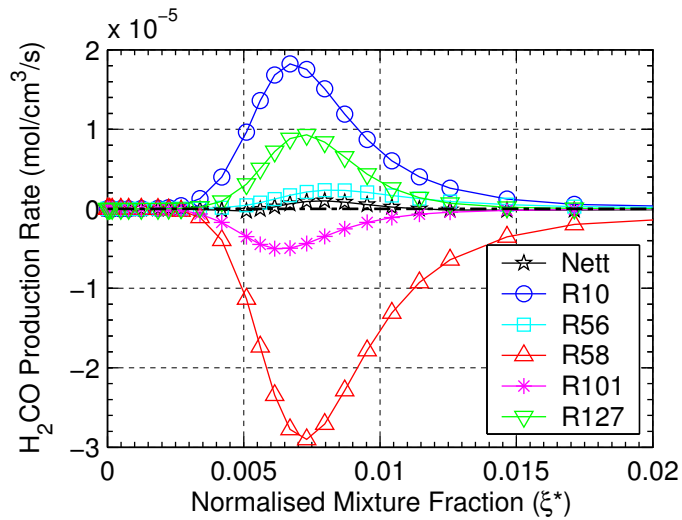

Figure 7.3: H$_2$CO production rate via major reactions, found from laminar flame calculations. CH$_4$/H$_2$ fuel with 3% O$_2$, 1100K oxidant stream. Strain rate, $a{\approx}200\mathrm{s}^{-1}$.

high strain case. This difference in O concentration between the two strain cases, coupled with a two fold increase in CH_3, seems to explain the relative reaction rate of R10.

An increase in the concentration of O at the location of peak H_2CO production seems to be one of the main contributors to the increase of H_2CO with strain. Investigation of reaction rates reveals that the major production of O is from O_2, via reaction *R38*: $H + O_2 \rightleftharpoons O + OH$. The production rate of O via reaction R38, and H & O_2 mole fractions, are also shown in Figures 7.4 & 7.5. It is apparent that the production rate of O at the location of peak nett H_2CO is ten fold greater at the higher strain rate. This is attributed to a five fold increase in O_2 concentration at the location of peak nett H_2CO between the two strain cases.

It is acknowledged that there are many concurrent processes that occur as the strain rate is increased. Nevertheless, the most significant increase in H_2CO with strain seems to occur via the following path;

$$O_2 \xrightarrow[+H]{R38} O \xrightarrow[+CH_3]{R10} H_2CO$$
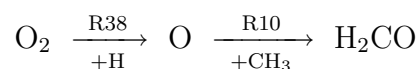
The identified pathway relates the increase in H_2CO with strain to an increase in O_2 concentration at the location of peak nett H_2CO production. For these laminar calculations, any O_2 at the location of peak H_2CO must have diffused from the oxidant stream. This diffusive transport of O_2 across the reaction zone is likened to partial premixing. The possibility of O_2 existing on the fuel rich side of the reaction zone is not unheard of. Even in conventional nonpremixed flames, O_2 has been measured along the centreline towards the base of an attached flame [78].

The reaction rates are seen to increase with strain. As the O_2 consumption rate increases with strain, more O_2 is consumed in the higher strain case. The consumption of O_2 competes with its diffusion across the reaction zone. From the observation of higher O_2 concentration on the fuel rich side, it is apparent that the diffusion of O_2 increases more than the reaction rate does at the higher strain condition. In other words, the flame front becomes more permeable as the strain rate is increased.
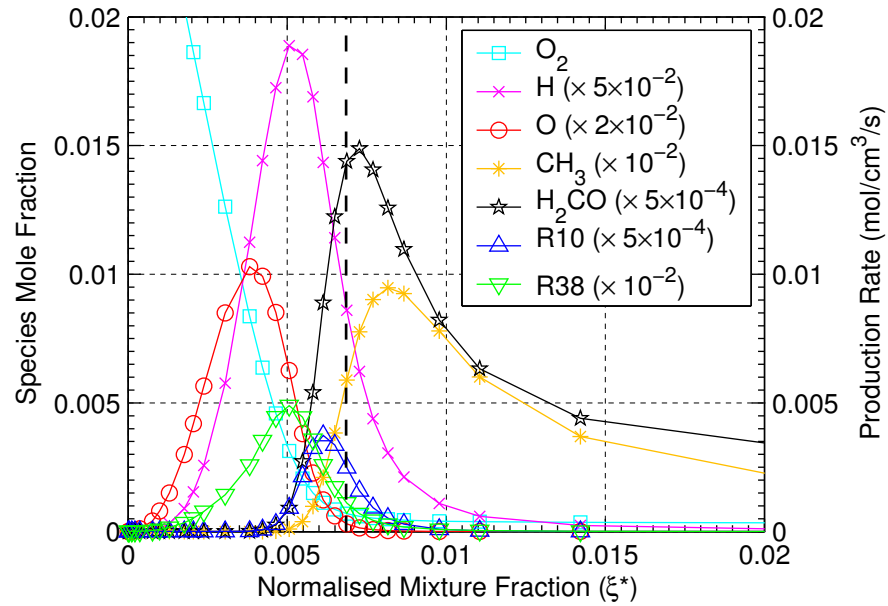
Figure 7.4: Selected species and production rates found from laminar flame calculations. Production rate of H_2CO is shown for reaction R10. Production rate of O is shown for reaction R38. CH_4/H_2 fuel with 3% O_2, 1100K oxidant stream. Vertical dashed line indicates location of peak H_2CO production rate. Strain rate, $a \approx 30s^{-1}$.
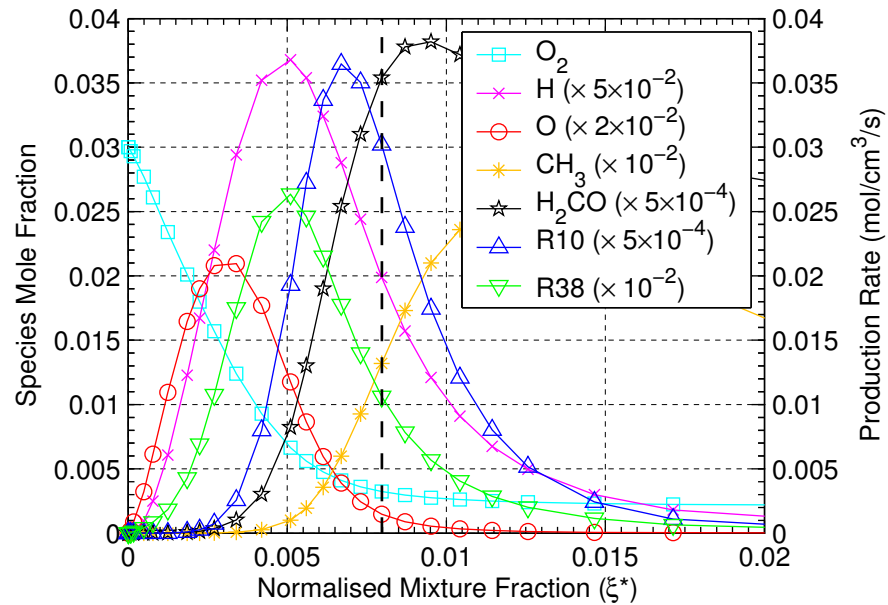

Figure 7.5: Selected species and production rates found from laminar flame calculations. Production rate of H_2CO is shown for reaction R10. Production rate of O is shown for reaction R38. CH_4/H_2 fuel with 3% O_2, 1100K oxidant stream. Vertical dashed line indicates location of peak H_2CO production rate. Strain rate, $a \approx 200s^{-1}$.

Referring back to Figure 7.1 it is seen that the amount of O_2 permeation (partial premixing) via diffusion seems higher at the 3% case than for the 9% O_2 oxidant stream. Comparing the 3% and 9% O_2 cases suggests that the higher reaction rates at the 9% O_2 level consume more O_2, greatly reducing the amount of O_2 permeation.

The relationship between the reaction rate and level of permeation suggests that a lower reaction rate (i.e. weaker reaction zone) permits a greater degree of partial premixing. This observation is consistent with the instantaneous images showing increases in H_2CO near the location of local weakening of the flame front.

7.3.2.3   Reaction Zone Weakening Summary

It is apparent that reaction zone weakening (i.e. a reduction in reaction rate) can manifest itself in one of two ways; either an increase in H_2CO or a reduction in OH concentration. Under MILD combustion conditions, the high temperature environment increases the amount of diffusion. The low O_2 conditions leads to a reduction in reaction rate, that is, a weaker reaction zone (as compared to higher O_2 oxidant stream conditions). The effects of weakening and diffusion contribute to a greater degree of transport across the reaction zone. Therefore, in MILD combustion a form of partial premixing occurs. This observation of O_2 permeation is seen to influence the H_2CO, but not the OH. In the case of OH, strain rate alone does not seem to significantly influence the OH concentration. However, large-scale turbulent mixing due to large-scale vortices can lead to a weakening of the flame front.

7.3.3   Localised Extinction/Reignition

It has been discussed (§7.3.2) that vortices can lead to a reduction in OH levels due to turbulent mixing. The reduction in OH (i.e. flame front weakening) can occur to such an extent that localised extinction can occur. While reaction zone weakening occurs at both of the measurement locations, localised extinction has only been observed at the furthest downstream measurement location. In such situations, the OH layer becomes locally broken. In the case of localised

extinction, the H_2CO levels are seen to significantly increase. Accompanying the break in OH, the H_2CO increase indicates both that (partial) premixing has occurred and that the combustion reactions continue. The extinction of the flame front is attributed to cooling.

In all images with evidence of local extinction it is possible to identify a region of surrounding air which has a lower temperature. Following extinction, the resultant partial premixing leads to significant increases in H_2CO concentration. The H_2CO which is seen in the instances of local extinction suggests that these extinction effects are genuine and not falsely identified due to out-of-plane effects, which are minimised in any case due to the streaming nature of this flow.

The presence of strong H_2CO at the location of extinction events indicates the presence of O_2 levels in excess of the hot coflow and suggests interaction with the surrounding air. If the surrounding air is entrained then it would follow that when the combustion reaction reignites it will do so with a greater reaction intensity due to the higher O_2 concentration. This is, in fact, seen in the form of increases in the OH concentration and higher temperatures after reignition events.

The temperature of the surrounding air does not necessarily have to be cold (room temperature) air to cause localised extinction. Hot coflow that has mixed with surrounding air can have a temperature decrease sufficient to cause cooling of the flame front leading to extinction. An absolute definition of the requirements for extinction has not been identified as part of this study. A combination of local temperature, O_2 concentration, and time scales would all be expected to have an influence in conditions resulting in localised extinction.

The localised extinction of the flame front even at considerable temperatures (of the order of $\sim$500K) could have practical implications. For example, cooling from furnace walls or excessive heat removal could potentially lead to reductions in local temperature leading to localised extinction. In the case of the JHC burner, cooling is also associated with an increase in O_2 concentration. The lack of additional oxygen accompanying the lower temperatures in other circumstances may lead to widespread extinction.

While the extinction at the most downstream location is attributed to cooling, the jet Reynolds number also has an effect on the frequency of such extinction

events. As the Reynolds number is increased, the turbulent structures that are formed lead to more interaction with the surrounding air. In turn, this increases the likelihood of the flame front coming into contact with the cold/cool air. Therefore, the effects of Reynolds number are in the form of increased large-scale turbulent mixing. The results do not support an intuitive suspicion that the increased frequency of extinction events with increased Reynolds number is due to strain related effects.

The features which typify localised extinction events appear the same for the various flame conditions, suggesting the same mechanism is the cause in all cases.

The effect of surrounding air entrainment leading to a combination of localised flame front weakening/extinction, and subsequent increases in reaction rates, indicates the importance of ensuring homogeneous mixing under MILD combustion conditions. The inclusion of comparatively small amounts of fresh air, even at elevated temperatures due to mixing with the heated coflow, can lead to localised increases in reaction rates. Subsequently, the higher temperatures in turn lead to higher levels of NO_x formation, thus counteracting the benefits of MILD combustion. It is therefore imperative that fresh air be excluded from MILD combustors without well controlled mixing to ensure high dilution with combustion products prior to the reaction zone.

7.4 Fuel Composition Effects

7.4.1 Primary Fuel Type

In Chapter 6 it was shown that under hot and diluted oxidant stream conditions the reaction zone is not significantly affected by the fuel type. The fuels considered were natural gas, ethylene, and LPG (each diluted with hydrogen 1:1 by volume). Both from measurements and strained laminar flame calculations the OH concentrations results were seen to be quite constant. Only minor changes of the OH spatial distribution were noted, and attributable to differences in fuel velocity required to maintain constant Reynolds number. The only significant changes with the fuel type were noted in the H_2CO levels, most notably with

the C_2H_4/H_2 flame. The trends in the measured H_2CO levels were seen to be consistent with laminar flame calculations.

The similarity of the combustion characteristics for the various gaseous hydrocarbon fuels considered suggests that MILD combustion should be readily adapted for different fuel types. The insensitivity to fuel type is potentially a significant advantage for the implementation and application of MILD combustion to practical systems.

A key parameter which contributes to the structure of the reaction zone is the addition of hydrogen (H_2) to the primary fuel. It was found from experimentation that when H_2 was not added to the jet the flames would typically blow-off. Only the C_2H_4 flame could be sustained, and even then, it appeared lifted. The role of H_2 in flame stabilisation will be considered in §7.4.2.

The importance of H_2 addition to the fuel is also reflected in laminar flame calculations. For the experimental 3% O_2 oxidant stream conditions, the calculations showed no temperature rise across the reaction zone for either CH_4 or C_3H_8 as the fuel, without any H_2 in the fuel stream. A variety of imposed strain rates were attempted, but none showed evidence of a reaction. For C_2H_4 fuel, a reaction was achievable with the calculations, but only at low to moderate strain rates. These trends in the calculation for the undiluted fuel types are in agreement with those noted during the experiments with the JHC burner.

To examine the structural differences when H_2 is added to the fuel, Figure 7.6 shows selected species concentrations found from strained laminar flame calculations (details in Appendix A.9). The conditions for Figure 7.6 are identical as for the previously presented in Figure 6.15, but without H_2 added to the fuel. As outlined in the preceding paragraph, comparisons can only be made at the 9% O_2 case, as at the 3% O_2 conditions a reaction could not be sustained.

Comparison of Figure 7.6 (no H_2 addition) to Figure 6.15 (with H_2 addition) reveals major differences in the selected species concentrations. Unlike with H_2 diluted fuels, Figure 7.6 shows that the OH profiles are dependent on the fuel type. For C_2H_4, the peak OH concentration is 30% higher, and the FWHM (full-width half maximum, in the normalised mixture fraction space) is 40% wider, than for CH_4 fuel. Significant differences for the various fuel types in the H_2CO and HCO
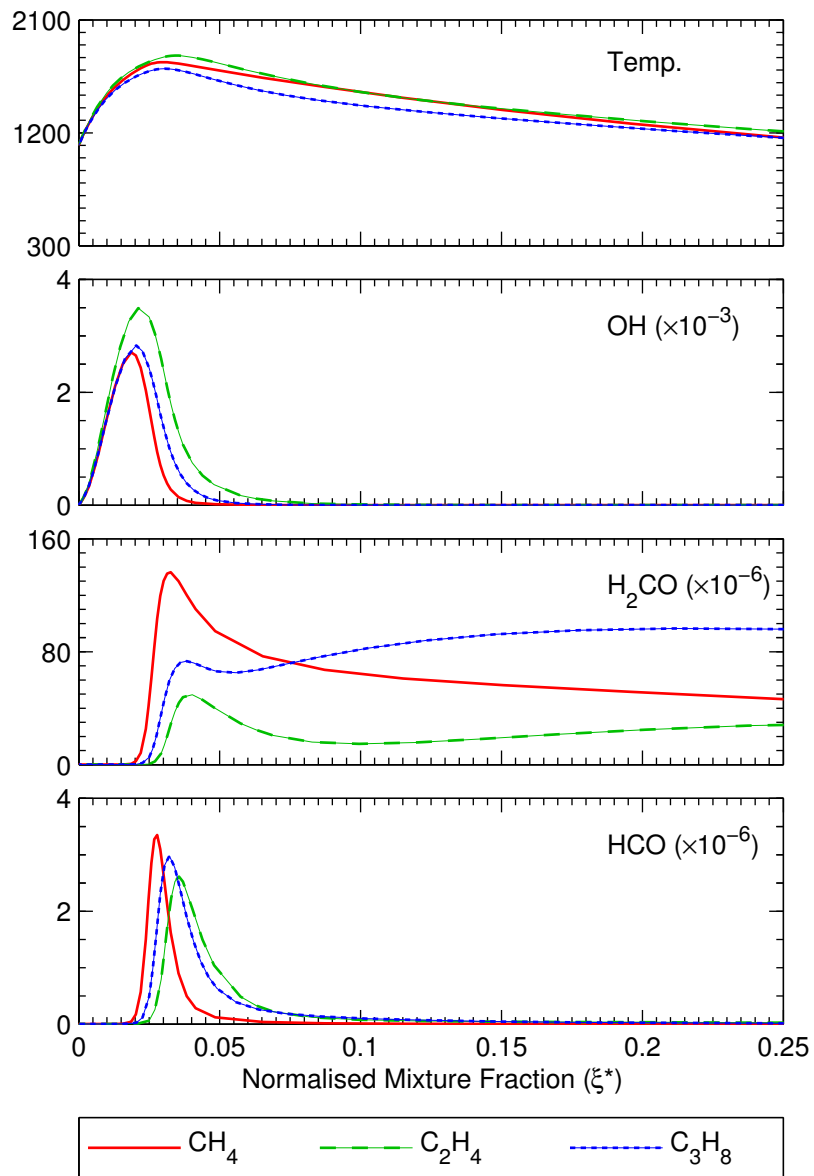
Figure 7.6: Temperature and species mole fractions from strained laminar flame calculations in (normalised) mixture fraction space for 9% O_2 coflow composition ($a \approx 100s^{-1}$).

profiles are also far more pronounced than seen with H_2 dilution. Comparison of the peak concentration in the reaction zone of H_2CO and HCO reveals that both increase by ~ 3.5 without H_2 addition.

It is apparent that without H_2 addition to the fuel, the reaction zone structure is dependent on the primary fuel type. When H_2 is added to the primary fuel, under MILD combustion conditions, the reaction zone for each of the hydrocarbon fuels considered becomes very similar. This independence of the reaction zone structure suggests that a wide variety of fuels may be useable for achieving MILD combustion. Furthermore, H_2 addition to the fuel stream greatly enhances flame stabilisation.

7.4.2 Reaction Zone Transition

Some of the flames presented in Chapter 5 showed visible characteristics typical of lifted flames. Closer inspection of the species images in the "lifted" region of these flames suggests pre-ignition reactions take place. Within the "lifted" region, H_2CO formation is clearly apparent and a definite OH layer is identified. Downstream of the "lift-off" height, the OH concentration significantly increases. Since OH is measured both upstream and downstream of the "lift-off" height (albeit at very different concentrations), it is more appropriate to identify this as a transition point. The general observations relating to this transition point are analogous to the lift-off height in conventional lifted flames.

The OH concentration on either side of the transition point essentially exhibits a bimodal behaviour, where it is low upstream of the transition (pre-ignition reactions), and high downstream (in the fully reacting conditions). While this is not strictly an extinction/reignition process, it is proposed that it may be somewhat related. When the temperature is above auto-ignition, specific ignition/extinction does not occur, rather a monotonic function exists between the two (§5.7.2). It is possible however that instead of definite ignition or extinction, the reaction may take place as either strong or weak. This does not preclude the monotonic relationship between ignition/extinction, but does explain the "bimodal" behaviour of OH concentration across the transition point in these flames.

An important difference between the transition point in these flames and conven-

tional lifted flames is their trend with jet velocity. Typically the lift-off height increases with the jet velocity, whereas for the flames in a hot diluted coflow the transition height decreases. This major difference further highlights a fundamental change in the stabilisation mechanism of these flame. An increase in jet velocity is believed to promote intense mixing with the coflow which acts to improve stabilisation, and hence reduce the transition height.

The flames which appear "lifted" are at the higher (9%) O_2 coflow. For the same fuel properties and Reynolds number, at the lower (3%) O_2 coflow conditions the flames appeared attached. In general, the flames in the higher O_2 coflow are associated with a more intense reaction zone. Therefore, the reaction rate due to the coflow O_2 level does not appear responsible for the 9% O_2 flames exhibiting the transitional behaviour.

The scalar imaging of this study does not provide categorical evidence of why the 9% O_2 flames exhibit the transitional behaviour and yet the 3% O_2 flames do not. A possible reason is the shift in stoichiometric mixture fraction for the 9% O_2 case towards the fuel rich side. The three-fold difference in stoichiometry may cause the reaction zone to be under more significant influence from the jet shear layer. Another possibility is that the lower reaction rates associated with the 3% O_2 coflow lessen the impact of flame induced strain rates. These suggestions are only speculative. From the scalar measurements available, identification of the role of either of these possibilities, or any other factors, cannot be quantified.

While the fuel diluted ethylene flames in the 9% O_2 coflow typically show a lifted flame appearance, with H_2 dilution the flames become unequivocally attached. Addition of H_2 is expected to increase the laminar flame speed – an important parameter in flame stabilisation. To investigate this aspect, the laminar flame speed has been calculated for the various experimental conditions using the PRE-MIX code of the Chemkin package and the GRI-Mech 3.0 mechanism. Details of these calculations are provided in Appendix A.11. At stoichiometric conditions, Table 7.1 shows the calculated laminar flame speed for the various fuel combinations at the 3% & 9% O_2 levels. Somewhat surprisingly, the addition of H_2 has not increased the laminar flame speed for these cases.

Table 7.1 also shows the calculated laminar flame speed results for 1100K, but at 15% and 21% O_2 (with the balance N_2). These calculations bridge the gap

Fuel	Ratio	3% O_2	9% O_2	15% O_2	21% O_2
C_2H_4	—	270 cm/s	881 cm/s	956 cm/s	1180 cm/s
C_2H_4/H_2	1:1	264 cm/s	779 cm/s	1410 cm/s	1391 cm/s
C_2H_4/air	1:3	430 cm/s	949 cm/s	969 cm/s	1180 cm/s
C_2H_4/N_2	1:3	251 cm/s	847 cm/s	904 cm/s	1458 cm/s

Table 7.1: Calculation of laminar flame speed for diluted ethylene flames at 1100K. Dilution ratio expressed on molar basis. The 3% and 9% O_2 oxidant cases represent the experimental coflow composition. For 15% and 21% O_2 levels the balance is N_2. $\Phi = 1$ in all cases.

between 21% O_2, 300K conditions to those at 1100K and 3% or 9% O_2. The results of Table 7.1 indicate that at the higher O_2 levels, the H_2 dilution does indeed increase the laminar flame speed. This was not seen at the lower O_2 levels. This suggests that the reduction in laminar flame speed with H_2 addition at the lower O_2 levels is an effect of the kinetic differences between these cases, rather than the temperature. It is noted that the laminar flame speed for C_2H_4 at 21% O_2 for a 1100K unburned temperature agrees well with correlations given in Turns [111], which yield a calculated flame speed of 1154 cm/s for these conditions. An incidental note is made that the laminar flame speed increases with N_2 dilution for the 21% O_2 flame.

The laminar flame speed does not necessarily shed light on why the H_2 diluted flames attach whereas the other fuel diluents lead to the transitional behaviour of the flames. Instead, the difference is attributed to the role of H_2 as being an ignition promoter [46] which improves the flame stability. The important role of H_2 was seen in §7.4.1. Furthermore, given that the trend of lift-off does not particularly correlate with the laminar flame speed indicates the cause of this transition is not related to lift-off in the usual sense. This is consistent with the other observations already noted, primarily the pre-ignition reactions.

The detection of flame species upstream of the transition height does not necessarily imply that the flames are or are not lifted. The reactions which occur in the "lifted" region are believed to be associated with pre-ignition reactions rather than a fully developed flame front. There may be some dispute over the terminology of this phenomenon. Given that conventionally lifted flames do not exhibit pre-ignition reactions in the same way, it does not seem justifiable to also

refer to these flames as lifted. Describing these flames as having a transition in reaction zone structure seems a more accurate depiction.

At low O_2 levels, the flames do not exhibit the transitional behaviour. Even in the flames which visually appear lifted, it is apparent that pre-ignition reactions occur within the "lifted" region. The presence of OH and H_2CO suggests that the flames that appear lifted are not necessarily lifted in the conventional sense. The hot and diluted coflow conditions of MILD combustion seems to provide a fundamentally different environment for the stabilisation of these flames.

The transitional behaviour of the 9% O_2 flames is very different to the stable flames in the 3% O_2 coflow which typify MILD combustion. This suggests that ensuring low O_2 concentration, by maintaining effective dilution through recirculation within a furnace, eliminates the need for high jet momentum as a prerequisite for MILD combustion. This in effect allows higher modulation ratios in a MILD combustion furnace. The images also reveal that fuel starts reacting immediately after leaving the jet. In a MILD combustion furnace, the same oxidant conditions persist for the entirety of the reaction, and hence it is highly likely to continue reacting in a similar manner. Again, this highlights the importance of well controlled mixing in the establishment and sustainability of MILD combustion.

7.5 Relationship between OH and H_2CO

The combination of OH and H_2CO has been suggested as an indicator of formyl (HCO), and in turn the heat release rate (§2.3.2.4). The work of Paul & Najm [91] has shown that the product (i.e. the spatial overlap) of OH and H_2CO images from premixed flames does indeed correlate with heat release.

Rather than focussing on the absolute intensity of $[OH] \cdot [H_2CO]$, in this section consideration is primarily given to the relative overlap of the two species. Due to the low oxygen conditions, the heat release rate is inherently low. Coupled with a less than ideal signal-to-noise ratio, presenting the overlap of OH and H_2CO yields more meaningful results. Instead of introducing new findings, investigation of the overlap is intended to complement the results already presented. As such,
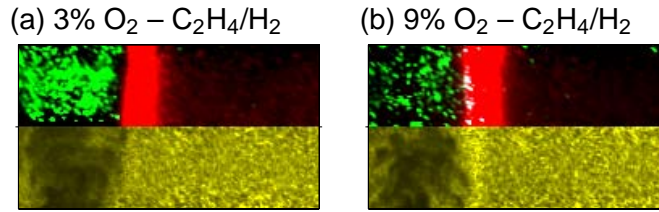
(a) 3% O_2 – C_2H_4/H_2 (b) 9% O_2 – C_2H_4/H_2

Figure 7.7: Selected instantaneous OH, H_2CO and temperature measurements showing effect of coflow O_2 level. Top image contains OH, H_2CO and spatial overlap of OH & H_2CO. Bottom image is the temperature. OH: Black–Red. H_2CO: Black–Green. [OH]·[H_2CO]: Black–White. Temperature: Black–Yellow. Each image 8×30mm. Axial location 35mm above jet exit.

looking at the overlap is more appropriate than the attempting to infer the actual heat release rate.

For the various cases to be considered, there are significant differences in the product of OH and H_2CO. An upper-threshold has been applied to the images to highlight the relative characteristics. The result is that [OH]·[H_2CO] appears saturated, whilst in other instances the product is barely discernable. In reality, it is only the maximum values that are clipped. Even though the images may appear to exhibit a binary relationship, the low intensity [OH]·[H_2CO] is in fact retained.

To demonstrate spatial overlap in this section, the images are split into the species and the temperature. In the top portion of these images, black–green represents the H_2CO signal, and black–red the OH intensity. The scaling of the species is arbitrary, but constant throughout the entire section. The overlap of OH and H_2CO is shown in white. The bottom portion of the images (in black–yellow) is the temperature.

7.5.1 Effect of O_2 Level

Figure 7.7 shows images of the OH/H_2CO overlap for the C_2H_4/H_2 flame at the 35mm location for two coflow O_2 levels. The H_2CO in these images appears rather blotchy. This appearance of H_2CO in the H_2 diluted flames has been seen elsewhere, but is far more apparent with this colour-scaling. Such blotchy

appearance is not seen to this extent with the other fuel compositions, suggesting that this may well be a genuine effect.

The patches of white colouration at the 9% O_2 case (Figure 7.7b) indicates overlap, and thus heat release. The scattered H_2CO distribution leads to the overlap also appearing blotchy. Nevertheless, the region of overlap spatially agrees with the temperature increase in the reaction zone.

At 3% O_2 (Figure 7.7a) there does not appear to be any spatial overlap between OH and H_2CO. It should be noted that the lack of apparent overlap in the 3% O_2 image does not imply that there is no heat release. The adopted scaling of the image simply does not highlight the overlap. The species images may be artificially over-corrected to yield an overlap image, but this has the effect of distorting the features in the images. Nevertheless, the differences between the two images in Figure 7.7 highlight the effect of the O_2 increasing the heat release rate.

The difference in the spatial overlap (i.e. heat release) follows the expected trend with O_2 coflow level. At the lower O_2 level the heat release is less than for the 9% O_2 case. This is supported by the laminar flame calculations presented in Figures 6.14 & 6.15, where the overlap (as determined by HCO) increases approximately five fold in mixture fraction space. Comparison of the laminar flame calculations presented in Figure 6.16 reveals that under conventional air conditions there is twice the overlap for the 9% O_2 case. This further highlights the low overlap under the hot and diluted conditions.

7.5.2   Reaction Zone Transition

In the transitional flames (those that visually appeared lifted) an apparent bimodality has been noted. Upstream of the transition height, pre-ignition reactions have been identified. Downstream of the transition the OH concentration increases markedly.

Figure 7.8a presents an image showing the transition point of a C_2H_4/air flame (9% O_2) at the 35mm location. This image is the same as presented in Figure 5.8c. The image shows high OH levels toward the top of the image, and toward the
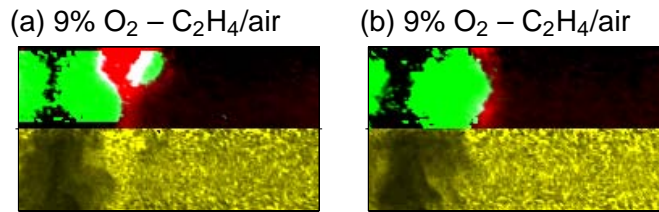
(a) 9% O_2 – C_2H_4/air   (b) 9% O_2 – C_2H_4/air

Figure 7.8: Selected instantaneous OH, H_2CO and temperature measurements showing reaction zone transition. Top image contains OH, H_2CO and spatial overlap of OH & H_2CO. Bottom image is the temperature. OH: Black–Red. H_2CO: Black–Green. [OH]·[H_2CO]: Black–White. Temperature: Black–Yellow. Each image 8×30mm. Axial location 35mm above jet exit.

bottom of the image OH levels are much lower. It is apparent that spatial overlap (i.e. heat release) only occurs at the top of the image, where the OH concentration is highest. Figure 7.8b shows an instance of the same flame conditions, beneath the instantaneous transition height. In this situation, there are minimal signs of heat release. As noted in §7.5.1 the images could in fact be manipulated to reveal heat release, but this does not change the relative differences relating to the transition point.

The images in Figure 7.8 support the proposition of different reaction rate on either side of the transition height. Accompanying the pre-ignition reactions (Figure 7.8b) the heat release is very low. Downstream of the transition, the heat release rate increases significantly. These observations confirm that there is indeed two reaction regimes within the transitional flames.

7.5.3 Spatial Mismatch

In §6.5.5 (Figure 6.13) it was revealed that at the most downstream (125mm) location there can be a spatial mismatch between the OH and H_2CO. Figures 7.9a and 7.9b provide some examples to highlight this spatial mismatch. Apparent in both of these images is a separation between the OH and H_2CO. In between the OH and H_2CO the temperature increases. The temperature increase is suggestive of heat release in this region. Despite the temperature increase, it is very clear that there is no spatial overlap of OH and H_2CO in this region. This suggests that taking the product of OH and H_2CO may not be suitable for inferring the
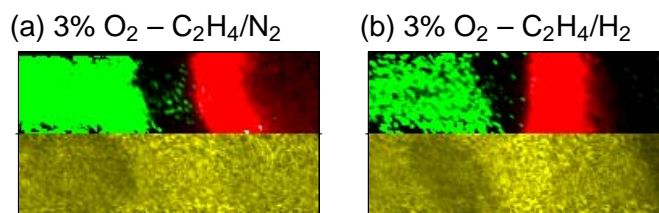
(a) 3% $O_2 - C_2H_4/N_2$ (b) 3% $O_2 - C_2H_4/H_2$

Figure 7.9: Selected instantaneous OH, H_2CO and temperature measurements showing spatial mismatch. Top image contains OH, H_2CO and spatial overlap of OH & H_2CO. Bottom image is the temperature. OH: Black–Red. H_2CO: Black–Green. [OH]·[H_2CO]: Black–White. Temperature: Black–Yellow. Each image 8×30mm. Axial location 125mm above jet exit.

heat release under these hot and diluted oxidant stream conditions.

In §2.3.2.3 it was outlined that at high temperature regions, H_2CO destruction occurs. As such, inferring heat release from [OH]·[H_2CO] has some limitations.

7.6 Future Work

Significant development toward the understanding of fundamental aspects relevant to MILD combustion have been revealed by this study. As with any finite piece of work, there remain some issues which could be the subject of future investigation. Two interesting issues that have been raised are the possibility of flow laminarisation, and the transition in the reaction zone which gives a lifted flame appearance.

Laminarisation effects

Based on the jet Reynolds number, all of the measurements presented are considered to be in the turbulent regime ($5000 \leq Re_{jet} \leq 15,000$). In general however, the majority of images suggest that the shear layer is unconvoluted, giving the impression of a laminar flow. A laminarisation of the flow is feasible because the high temperature environment could lead to a reduction in local turbulent Reynolds number due to the change in viscosity.

Aside from the appearance of the instantaneous images, some other effects (or more specifically, the lack of effect) of the Reynolds number also tend to support a laminarisation of the jet flow. As the jet Reynolds number is increased, neither the OH mean nor RMS radial profiles show any significant change in shape or peak value. Similarly, the RMS of temperature in the shear layer is very low. These observations are especially true for the lower (3%) O_2 coflow case. Given that the laminarisation effects seem even more pronounced at the 3% O_2 coflow possibly suggests that the lower reaction rates may lead to further laminarisation than seen at 9% O_2 case. This may be due to the more homogenous temperature profile.

It is worth noting that despite the potential laminarisation which seems to occur, turbulent structure can still have significant influence on the reaction zone. Nevertheless, the results certainly seem to suggest that some form of reduction in turbulence levels takes place under the hot and diluted O_2 conditions.

The most evidential support for laminarisation is in the unconvoluted appearance

of the instantaneous images. To further investigate a laminarisation of the reaction zone would require in-depth flow-field measurements. Future work on laminarisation would highly benefit from simultaneous temperature measurements to complement the flow-field data.

Reaction Zone Transition

At some conditions, the flames visually appear lifted. Species imaging reveals that pre-ignition reactions occur within the "lifted" region, suggesting that such flames exhibit transitional behaviour rather than being lifted in the conventional sense. These lifted, or transitional, flames are seen in the 9% O_2 coflow whereas when the O_2 concentration is decreased to 3%, the flames appear attached.

Contrary to the observations, the 9% O_2 coflow would be expected to lead to a more robust reaction zone which is less susceptible to "lifting" than the 3% O_2 case. Some possible reasons for this contrast have been suggested, including; a change in the stoichiometry at the higher O_2 level shifting the flame front closer to the shear layer, and/or, a reduction in flame induced strain rate. Laminar flame speed differences have also been investigated, but found that this would not explain the difference.

To confirm or deny the proposed possibilities for the transitional behaviour, or to investigate other potential causes, detailed flow-field analysis would be required. Such measurements (or modelling) should include comprehensive determination of the strain rate, and be accompanied by identification of the stoichiometric surface.

Chapter 8

Conclusion

Combustion of hydrocarbon fuels is anticipated to continue to play a significant role in the production of the world's energy supply in the foreseeable future. With current concerns of fuel shortages, greenhouse global warming, and other pollutant concerns, there is a demand for new combustion technologies with improved efficiency with lower pollutant emissions. The Moderate or Intense Low oxygen Dilution (MILD) combustion regime offers the potential to meet these requirements.

The fundamental aspects of the unique MILD combustion regime, under controlled experimental conditions, have been examined in this project using laser diagnostic techniques. The two key flame intermediates OH and H_2CO, as well as temperature, have been imaged simultaneously to reveal details relating to the reaction zone. Simultaneous imaging enables the spatial distribution of each scalar to be examined, and also the combined effect of the interactions of the measured scalars.

Multiple flame parameters are varied independently to examine the effect of each in isolation. The key parameters investigated are the effect of the oxidant stream oxygen concentration, the fuel stream Reynolds number, and the fuel composition (both the fuel type and also the effect of fuel dilution by various diluents).

The oxidant stream O_2 concentration is a key parameter in achieving MILD combustion conditions. The effect of lowering the O_2 level is to lead to reductions

in the OH and temperature in the reaction zone, in effect leading to a less intense reaction. Associated with the reduced reaction rate is the spatial broadening of the reaction zone at low O_2 concentrations.

In all cases, from a visual perspective, lowering the O_2 concentration of the coflow oxidant stream significantly reduces flame luminosity, and almost completely eliminates soot from the flames. Even further downstream, where the coflow effects have diminished, the oxidant composition is still seen to have an influence on the flame appearance.

Beyond the confines of the controlled coflow of the JHC burner, surrounding air entrainment can also alter the oxygen concentration, having further influences on the reaction zone. The additional oxygen introduced by the surrounding air may be expected to increase the reaction rates, but the lower temperature of the surrounding air can have the opposite effect and can lead to a localised extinction of the flame front. Following extinction, partial premixing occurs leading to increased reaction rates, and subsequently higher temperatures and consequently higher NO_x production. Cooling of the flame front therefore has the effect of counteracting the intentions of MILD combustion.

In general, the effect of increasing the jet Reynolds number is quite minimal on the fundamental structure of the reaction zone. Naturally, as the Reynolds number is increased the flow exhibits more turbulent structure, and so the flame front becomes more convoluted. This vortex interaction can lead to changes in the reaction zone structure, which is described as a weakening process. The weakening is characterised by a reduction in OH concentration and thickness. Weakening also leads to increases in H_2CO due to O_2 transport across the flame front. This oxygen permeation is likened to partial premixing, and is more pronounced at the lower O_2 levels which typify MILD combustion.

The effect of fuel composition has been examined, both by changing the primary fuel type, and by changing the fuel diluent. Changing the primary fuel type does not seem to affect the reaction zone in any tangible manner, when hydrogen is mixed with the fuel. The observed independence of the reaction zone structure suggests that a wide variety of fuels may be useable for achieving MILD combustion. The similarity of the reaction zone structure is attributed to the addition of hydrogen. Without hydrogen addition, at the higher O_2 level the reaction zone

structure becomes dependent on the primary fuel, and at the lower O_2 level the flames do not stabilise.

The effect of fuel dilution has been seen to have substantial effects on the visual appearance of the flames. At the lower oxygen coflow, irrespective of the fuel diluent, the flames all appear attached to the jet exit. In contrast, at the higher (but still well below atmospheric air) oxygen concentration, most of the flames appear to be lifted. The flame intermediate measurements do not support the visually lifted observation. Instead, it is apparent that a reaction does occur in the "lifted" region, but the reaction rate is significantly less than downstream of the transition point. The MILD combustion conditions provide a different mechanism for flame stabilisation.

In summary, an experimental burner has been used to study the fundamental aspects of MILD combustion under controlled conditions. Advanced laser diagnostic techniques have revealed interesting phenomenon which occur within these flames that would not be otherwise possible. The findings of this work are relevant to the implementation of MILD combustion to practical combustion systems to fulfil the world's energy demands.